



저작자표시-비영리-변경금지 2.0 대한민국

이용자는 아래의 조건을 따르는 경우에 한하여 자유롭게

- 이 저작물을 복제, 배포, 전송, 전시, 공연 및 방송할 수 있습니다.

다음과 같은 조건을 따라야 합니다:



저작자표시. 귀하는 원저작자를 표시하여야 합니다.



비영리. 귀하는 이 저작물을 영리 목적으로 이용할 수 없습니다.



변경금지. 귀하는 이 저작물을 개작, 변형 또는 가공할 수 없습니다.

- 귀하는, 이 저작물의 재이용이나 배포의 경우, 이 저작물에 적용된 이용허락조건을 명확하게 나타내어야 합니다.
- 저작권자로부터 별도의 허가를 받으면 이러한 조건들은 적용되지 않습니다.

저작권법에 따른 이용자의 권리는 위의 내용에 의하여 영향을 받지 않습니다.

이것은 [이용허락규약\(Legal Code\)](#)을 이해하기 쉽게 요약한 것입니다.

[Disclaimer](#)

Thesis for a Ph. D degree

**Study on interferometric coherence model and
its application to natural disaster detection
using single and full polarimetric SAR data**

**간접 긴밀도 모델 연구와 단일 및 다중 편파
SAR 영상을 활용한 자연 재해 탐지**

August, 2017

**Graduate School of
Earth and Environmental Sciences
Seoul National University**

Jungkyo Jung

Abstract

For rapid response and efficient recovery, the accurate assessment of damaged area caused by the natural disaster is essential. SAR system has been known as a powerful and effective tool for estimating damaged area due to its imaging capability at night and cloudy days. One of the damage assessment methods is based on interferometric coherence generated from two or more SAR images, namely coherent change detection. The interferometric coherence is a very sensitive detector to subtle changes induced by dielectric properties and positional disturbance of scatterers. However, the conventional approaches using the interferometric coherence have several limitations in understanding the damage mechanism caused by natural disasters and providing the accurate spatial information. These limitations come from the complicated mechanism determining the coherence. A number of sources including the sensor geometry, radar parameters, and surface conditions can induce the decorrelation. In particular, the interpretation complexity of the interferometric coherence is severe over the vegetated area, due to the volumetric decorrelation and temporal decorrelation. It is a remaining problem that the decorrelation caused by the natural phenomena such as the wind, rain, and snow can come along the decorrelation caused by natural disaster. Therefore, a new accurate approach needs to be designed in order to interpret the decorrelation sources and discriminate the effect of natural disaster from that of natural phenomena. This research starts from the development of the temporal decorrelation model to interpret the interferometric coherence observed in multi-temporal SAR data. Then, the coherence model is extended to be applied to the damage mapping algorithm for single- and fully-polarimetric SAR data for detecting the damaged area caused by volcanic ash and wildfire.

The coherence model is designed so that it explains the coherence behavior

observed in the multi-temporal SAR data. The noticeable characteristic is that the interferometric coherence tends to decrease as the time-interval increases. Also, the coherence for multi-layer is determined by the different contributions of each layer. For example, the volume and ground layer can affect the total coherence observed in the forest area. In order to reflect the realistic condition and physically interpret the coherence, the coherence model proposed in this research includes several decorrelation sources such as temporally correlated dielectric changes, temporally uncorrelated dielectric changes and the motions in the two layers; i.e. ground and volume layer. According to the proposed model, the coherent behavior of each layer is explained by exponentially decreasing coherence (temporally-correlated coherence), and the difference between the observed coherence and the temporally-correlated coherence is interpreted as the temporally-uncorrelated coherence. The ground-to-volume ratio plays an important role to determine the contributions of temporal decorrelations in ground and volume layer.

Suggested model is applied into the coherent change detection for multi-temporal and single-polarized SAR data. The method is evaluated for detection of volcanic ash emitted from Kirishima volcano in 2011 using ALOS PALSAR data. The criterion of the spatial baseline is calculated based on the Random Volume over Ground model to minimize the volumetric decorrelation. The model parameters are extracted under the several assumptions, and then the historical coherence behavior is analyzed using kernel density estimation method. By comparing the changes of model parameters between the reference pairs and event pairs, the probability of surface changes caused by volcanic ash is defined. The in-situ data, which measure the depth and area density of volcanic ash, is compared with the calculated probability maps for determining the threshold and evaluating the performance. The correlation is found over the area where the depth of the volcanic ash is more than 5 cm and the area density is more than 10 kg/m².

The temporal decorrelation model is also used for change detection using multi-temporal and fully-polarimetric interferometric SAR data. By introducing polarimetric and interferometric SAR data, the assumptions used in the method for single-polarized SAR data are reduced and the changes of two layer can be estimated separately. The approach is applied to detect the burnt area caused by the Lake fire, in June 2015 using UAVSAR data. Even though, coherence analysis shows the loss of coherence due to the fire event, the temporal decorrelation caused by the natural changes is mixed with the signal of the event. In order to apply the coherence model and extract the model parameter, here, the three steps are proposed; coherence optimization, temporally-correlated coherence estimation, and temporally-uncorrelated coherence estimation. Then, the extracted model parameters are used for the damage assessment using the probability determination based on the history of natural phenomena. The final generated damage map shows higher performance than the damage mapping method using coherence only. Also, the comparison result with the RMoG model shows high agreement, which implies the extraction of the model parameters is reliable.

One of the advantages of the proposed algorithm is that the more accurate delineation of damage area can be expected by isolating the decorrelation caused by the natural disaster from the effect of natural phenomena. Moreover, a distinguishable benefit can be obtained that the changes over ground and volume layers can be assessed separately by utilizing the multi-temporal full-polarimetric SAR data.

Keyword: Interferometric coherence, coherence model, Change detection, SAR interferometry, Polarimetric SAR interferometry, damaged area detection
Student Number: 2013–30107

Contents Table

Chapter 1. Introduction	1
1.1. Brief overview of SAR and its applications	1
1.2. Motivations	5
1.3. Purpose of Research	8
1.4. Outline	10
Chapter 2. Estimation of complex correlation and decorrelation sources	11
2.1. Estimation of complex correlation	11
2.2. Decorrelation sources	14
2.3. Derivation of coherence model assuming two layers for repeat-pass interferometry	35
Chapter 3. Damage mapping using temporal decorrelation model for single-polarized SAR data : A case study for volcanic ash	51
3.1. Description of study area	51
3.2. Data description	55
3.3. Extraction of temporal decorrelation parameters	61
3.4. Probability map generation	68
3.5. Mapping volcanic ash	73
3.6. Discussion	76
Chapter 4. Damage mapping using temporal decorrelation model for multi-temporal and fully-polarized SAR data	78
4.1. Description of Lake Fire and UAVSAR data	79
4.2. Brief analysis of SAR amplitude and interferometric coherence ...	82
4.3. Damage mapping algorithm using coherence model	89
4.4. Applicable conditions of damage mapping algorithm using coherence model	114
4.5. Comparison of model inversion results and damage mapping algorithm results	120
4.6. Discussion and conclusion	129
Chapter 5. Conclusions and Future Perspectives	132

Abstract in Korean	140
Bibliography	147

Figure list

Fig. 2. 1. Probability density function of interferometric phase for coherence and the number of looks. Coherence levels range from 0.9, 0.7, 0.5, 0.3, and 0.1. The narrowest distribution corresponds to 0.9 coherence.....	12
Fig. 2. 2. Phase standard deviation for coherence and number of looks.....	13
Fig. 2. 3. Biased coherence versus true coherence for a various number of looks.....	14
Fig. 2. 4. Thermal decorrelation as a function of SNR.....	16
Fig. 2. 5. Geometry of SAR sensor (left) and geometric decorrelation for a function of baseline and slope angle in the case of ALOS PALSAR, FBS mode.....	17
Fig. 2. 6. Geometric decorrelation for a function of slope angle with perpendicular baseline, in the case of ALOS PALSAR, FBS mode.	18
Fig. 2. 7. Volume coherence for functions of extinction coefficient and canopy height. The volume coherence at 0 dB/m is coincident to the case that structure function is assumed as constant.	21
Fig. 2. 8. Schematic representation of random volume over ground model. (a) Actual geometry of sensors and forest, and (b) simplified two layers model.....	22
Fig. 2. 9. Volumetric decorrelation changes for a function of ground-to-volume ratio, extinction coefficient, baseline and volumetric height.....	23
Fig. 2. 10. Volume coherence versus Ground-to-volume ratio with (a) extinction coefficients assuming the canopy height is 15 m and (b) canopy height assuming the extinction coefficient is 0.15 dB/m.	25
Fig. 2. 11. Coherence change using Random-Volume-over-Ground (RVoG) model for a variety of forest parameters: (a) As a function of wavenumber and extinction coefficient ke assuming canopy height $hV = 20$ m. (b) As a function of wavenumber and canopy height assuming vertical extinction 0.1 dB/m.....	28
Fig. 2. 12. Schematic representation of scatterer motion for temporal decorrelation..	30
Fig. 2. 13. Theoretical temporal decorrelation induced by motions of scatters for three frequencies. L-band (1.27 GHz, 23.4cm), C-band (5.405 GHz, 5.56 cm), and X-band (10.25 GHz, 2.94cm). (a) When only horizontal motions exist and (b) when horizontal and vertical motions are present.....	33
Fig. 2. 14. Schematic representation of random motion over ground model. (a) Actual geometry of sensors and forest with motion, and (b) simplified two layers model with motion.	37

Fig. 2. 15. (a) Temporally correlated coherence behavior versus temporal baseline when the characteristic time constants are 8000, 4000, 2000, 1000, and 500 days. (b) Coherence modeled in two layers when characteristic time constants of the ground and volume are 5000 and 300 days and the ground-to-volume ratios are 10, 0, and 10 dB. The lines represent the hypothetical envelopes defined by the temporally correlated coherence. The points are the coherences of two-layer model for three different ground-to-volume ratios assuming Gaussian distributions with 0.85 and 0.4 means and 0.1 and 0.2 standard deviations for ground and volume layers, respectively.	42
Fig. 2. 16. Coherence behavior calculated from the RVoG model, RMoG model and the coherence model used in this study by varying the ground-to-volume ratios. The coherence involving the volumetric coherence might be non-monotonic, while the coherence changes monotonically when the volumetric coherence is zero in RMoG model. The coherence in the proposed model is monotonic only in the certain condition (i.e. $\gamma_g^t > \gamma_v^t / \cos\phi \gamma_g^t$). In the case of no volume layer, then the coherences of two-layer model is governed by only temporal decorrelation of ground regardless of the volumetric decorrelation (red triangles and green circles.)	46
Fig. 2. 17. Coherence loci in a complex plane. The RVoG model and the RMoG model that incorporates the volumetric decorrelation are illustrated. Meanwhile, the RMoG for a zero spatial baseline is observed in the line intersecting the origin. For the long-temporal and zero-spatial baseline case, the line between $\mu = 0$ and $\mu = \infty$ does not need to pass through the origin.	48
Fig. 3. 1. Topographic map of Kyushu, Japan (Top), and shade relief map of Kirishima volcano cluster (Bottom).	53
Fig. 3. 2. Landsat images acquired March 5, 2008, and April 13, 2013. Land-use maps provided by JAXA for Kirishima volcano and Kirishima city.	54
Fig. 3. 3. Sigma 0 and SNR distributions for diverse land uses.	55
Fig. 3. 4. Averaged coherence maps of reference pairs with time intervals from 46 days to 368 days. The interferometric pairs are listed in Table 3. 1.	58
Fig. 3. 5. Averaged coherence maps of reference pairs with time interval from 411 days to 828 days. The interferometric pairs are listed in Table 3. 1.	59
Fig. 3. 6. Coherence maps of event pairs. Jan.18.2011 - Mar.05.2011 (left), Dec.03 - Mar. 05.2011(Middle), and Aug. 27.2008 - Mar.05.2011. (Right)	60

Fig. 3. 7. Estimation of the temporally correlated changes in temporal decorrelation using exponential curve fitting. Coherence distribution along the time axis for (a) man-made structure (denoted B in Fig. 3. 8) and (b) forest area (denoted D in Fig.3. 8). Squares and circles are the measured coherence. Red lines indicate the decorrelation related to the temporally correlated dielectric changes.....	62
Fig. 3. 8. Estimated ground-to-volume ratio, μ , for (a) Kirishima volcano and (b) Kirishima city.	64
Fig. 3. 9. Characteristic time constant of the ground layer for (a) Kirishima volcano, and (b) Kirishima city.	65
Fig. 3. 10. Characteristic time constant of volume layer for (a) Kirishima volcano, and (b) Kirishima City	66
Fig. 3. 11. (a) Histograms (blue bar) of $\gamma_{t_rand}^g$ in ground-dominant pixels and (b) γ_{t_randg} and γ_{t_randv} in ground-and-volume-coupled pixels. Brown histograms indicate corresponding value in event pair. Black lines are the estimated cumulative density functions using KDE, and red boxes are probability of event. This analysis was performed in the area denoted as A and D in Fig. 3. 8	71
Fig. 3. 12. Calculated probability change map for (a) Kirishima volcano and (b) Kirishima city.	72
Fig. 3. 13. (a) Estimated probability map over 75% and (b) the predicted distributed map of the volcanic ash and location of in-situ depth data. Comparison between estimated probability and (c) the depth of volcanic deposits and also between (d) area densities.	75
Fig. 3. 14. (a and c) Two examples of coherence covariance matrix and (b and d) γ_{t_randg} matrices. (a) and (b) show the temporal behavior of bare soil, denoted A in Fig. 3. 6, and (c) and (d) are denoted B in Fig. 3. 6.....	77
Fig. 4. 1. A burnt area map of Lake fire. The image is provided from the Incident Information System (http://inciweb.nwcg.gov/).....	80
Fig. 4. 2. Land cover maps of Study area provided from National Gap Analysis Program.	83
Fig. 4. 3. UAVSAR image acquired on April 23, 2009. The color composite image was reconstructed using Pauli basis. R: HH-VV, G: 2HV, B: HH+VV.....	83
Fig. 4. 4. Amplitude ratio between images acquired on May 11, 2015, and June 29,	

2015, for (a) HH, (b) HV, and (c) VV polarizations.	84
Fig. 4. 5. ROC curve for amplitude ratio in Fig. 4. 4.	85
Fig. 4. 6. Averaged coherence maps using HH, VV, and HV images (a) acquired before the fire and (b) acquired crossing the fire.	86
Fig. 4. 7. Color composite image using coherence maps generated from interferometric pairs acquired before the fire. R: VV coherence G: HV coherence B: HH coherence.	88
Fig. 4. 8. Coherence maps generated from the interferometric pairs acquired on May 11, 2015, and June 29, 2015, for HH, VV, and HV polarization. The Lake fire started on June 17, 2015.	87
Fig. 4. 9. Coherence difference maps. The reference coherences are generated from the interferometric pair acquired on January 08, 2015 and May 11, 2015. The event coherence maps are calculated from the interferometric pair between May 11, 2015, and June 29, 2015. The black area means lowered coherence with respect to the reference coherence.	89
Fig. 4. 10. Flow chart for damage mapping.	90
Fig. 4. 11. Interferometric coherence optimization scheme using single-baseline multi- scattering mechanism.	94
Fig. 4. 12. Interferometric coherence optimization scheme using multi-baseline multi- scattering mechanism.	95
Fig. 4. 13. Interferometric coherence optimization scheme using single-baseline equal- scattering mechanism.	96
Fig. 4. 14. Interferometric coherence optimization scheme using multi-baseline equal- scattering mechanism.	97
Fig. 4. 15. Optimized coherence using multi-baseline (a-b) multi-scattering- mechanism and (c-d) equal-scattering mechanism. After optimization, the coherence was obtained for interferometric pairs (a, c) January. 08.2015- May.11.2015 and (b, d) May.11.2015-June.29.2015.	100
Fig. 4. 16. Coherence covariance matrices using multi-baseline multi-scattering- mechanism. (a) outcrop area, (b) unburnt forested area, (c) burnt forested area, and (d) burnt forested area which are denoted as A, B, C, and D in Fig. 4.12.	101
Fig. 4. 17. Coherence covariance matrices using multi-baseline equal-scattering- mechanism. (a) outcrop area, (b) unburnt forested area, (c) burnt forested area, and (d) burnt forested area which are denoted as A, B, C, and D in Fig. 4.12.	101
Fig. 4. 18. Characteristic time constants of (a) ground and (b) volume layers. High	

values of characteristic time constant mean the high coherence can be expected even in long temporal baseline.	105
Fig. 4. 19. Model parameter extraction for the ground layer. (a) Optimized coherence before the fire. (b) Optimized coherence during the fire. The temporally correlated coherence of ground layer for (c) 710 days and (d) 759 days. The temporally uncorrelated coherence of ground layer (e) before the fire and (f) during the fire. For the pair before the fire, the scenes acquired on May 31, 2013, and May 11, 2015, are used.	106
Fig. 4. 20. Model parameter extraction for volume layer. (a) Optimized coherence before the fire. (b) Optimized coherence during the fire. The temporally correlated coherence of volume layer for (c) 710 days and (d) 759 days. The temporally uncorrelated coherence of volume layer (e) before the fire and (f) during the fire. For the pair before the fire, the scenes acquired on May 31, 2013, and May 11, 2015, are used.	107
Fig. 4. 21. Histograms of total coherence (gray), the coherence of damaged area (pink), the coherence of undamaged area (green), the temporally uncorrelated coherence of damaged area (red curve), and temporally uncorrelated coherence of undamaged area (black curve) for (a) the ground and (b) the volume layer.	109
Fig. 4. 22. Damage probability calculation. The histograms can be built using history of the temporally uncorrelated coherence of ground (upper) and volume (lower) layer, respectively.	110
Fig. 4. 23. The calculated damage probability for (a) ground layer and (b) volume layer. The multiple probability maps of ground and volume layer can be averaged to reduce the effect of natural phenomena.	112
Fig. 4. 24. Performance evaluation of damage mapping algorithm. (a) reference damage map and (b) ROC curve. (c and d) The binary image of the ground layer when the false alarms are 0.01 and 0.05, respectively. (e and f) The binary image of volume layer when false alarms are 0.01 and 0.05.	113
Fig. 4. 25. (a and b) The interferometric phase of optimized coherence before the fire. (c) The phase difference between two optimized coherence (i.e. (a) and (b)). (d and e) The interferometric phase of optimized coherence during the fire. (f) The phase difference between two optimized coherence (i.e. (d) and (e)).	115
Fig. 4. 26. The absolute value of phase difference in Fig. 4. 25. (a) Before fire. (b) During fire.	116
Fig. 4. 27. Histograms of phase differences in (a) unburnt area and (b) burnt area.	116

Fig. 4. 28. Complex correlation plotted in the complex plane. (a) outcrop area, (b) unburnt forested area, (c) burnt forested area, and (d) burnt forested areas which are denoted as A, B, C, and D in Fig. 4.12.	117
Fig. 4. 29. Performance evaluation for different number of available scenes and interferometric pairs. Red line and squares indicate the true positive changes at 0.15 false positive. Blue line and squares represent the true positive change at 0.1 false positive.....	119
Fig. 4. 30. Temporal coherence comparisons between RMoG model and the coherence model used in this study. Temporal coherence of (a) ground and (b) volume layers for a pair 2015/05/11-2015/06/29 (49 days). Temporal coherence of (c) ground and (d) volume layers for a pair 2013/5/31-2015/06/29 (759 days). 122	
Fig. 4. 31. Characteristic time constant of (a) ground layer and (b) volume layer calculated from HH polarization data.	124
Fig. 4. 32. Characteristic time constant of (a) ground layer and (b) volume layer calculated from HV polarization data	125
Fig. 4. 33. Characteristic time constant of (a) ground layer and (b) volume layer calculated from HH polarization data.	125
Fig. 4. 34. Comparisons of characteristic time constant of ground layer extracted from full-polarization data with (a) HH, (b) HV and (c) VV polarizations. Comparisons of characteristic time constant of volume layer extracted from full-polarization data with (d) HH, (e) HV and (f) VV polarizations.	126
Fig. 4. 35. Damage probability maps derived from the damage mapping algorithm using multi-temporal single polarization data (Chapter 3).	128
Fig. 4. 36. ROC curves for coherence and damage mapping algorithm using single-polarizations and full-polarization.....	129

Table list

Table. 2. 1. Model comparison.....	45
Table 3. 1. Interferometric pairs used in this study.....	57
Table 3. 2. Extracted model parameter labeled in Fig. 3. 8.....	63
Table 4. 1. Sensor parameters of UAVSAR system.	81
Table 4. 2. UAVSAR data used in this study.	82
Table 4. 3. The probability of detection on various damage mapping methods.	129

Chapter 1.

Introduction

1.1. Brief overview of SAR and its applications

During the last few decades, the advanced techniques for remote sensing have been dramatically developed and have been used in numerous earth science fields. Synthetic aperture radar (SAR) is one of the promising and powerful systems for remote sensing and its applications involve hydrology, oceanography, glaciology, geology, and volcanology, etc.

Since SAR utilizes an active sensor which transmits the microwave signal and receives the backscattered signal from the targets, it can image in daylight or at night. Also, because the microwave is not less affected by the meteorological conditions, the SAR system has advantages that it can acquire the data anytime. Moreover, the images acquired from SAR sensors have unique information related to the dielectric and morphological properties of target media which are different illumination from the optical sensing measurement. Thus, the SAR measurement has been applied to a number of earth science fields and plays an important role as a complementary measurement with the other remotely sensed data. For this reasons, the needs of SAR sensors have been dramatically increasing, and consequently, a number of SAR satellites have been launched and successfully operated. Accordingly, a huge amount of robust and innovative techniques have been developed.

One of the main techniques of SAR system is interferometry, namely “InSAR”, which utilizes the phase differences between received signals by two or more SAR sensors. The phase components of complex values of SAR image is related to the distance to the target and scattering phase of the target. However, because the phase of one image of SAR sensor is effectively summation of each scatterer in a

resolutions cell, the sole phase is shown as a uniform probability density function and does not give any information of distance. The interference of two SAR images acquired at slightly different geometry cancels the scattering phase of the target recorded in each SAR images and measures the angular differences between the sensors and target at a certain height by applying simple trigonometry. The interferometer can estimate the topographic height by using the relationship between the topographic height and estimated angle difference angle and geometry of SAR sensors such as perpendicular baseline, the altitude of sensors and look angle. The concept of interferometry is first introduced to estimate the topographic height of Earth by Graham (Graham, 1974). The representative missions for generation of global digital-elevation-model (DEM) are Shuttle Radar Topography Mission (SRTM) and TanDEM-X mission (Jordan, 1997; Krieger et al., 2007; Moreira et al., 2004; J. J. Van Zyl, 2001). Both utilize InSAR techniques and provide DEMs with 30m x 30m and 15m x 15m spatial resolutions, respectively.

The major advance of InSAR system is designed to estimate surface displacement which is referred as differential SAR interferometry, DInSAR. The surface movement could be estimated by using conventional scheme by estimating the offsets between images when the target moves more than a resolution cell and its accuracy is the order of meters. However, DInSAR technique uses phase differences of SAR images. If the position of the target at revisit time is shifted compared to the initial position at first acquisition, it induces the phase shift in a resolution cell. Typical wavelength of the microwave which recent SAR satellites use range from 2cm (X-band) to 24 cm (L-band). The phase difference measurement can be orders of millimeter or centimeter, so its accuracy is much higher than the conventional scheme. DInSAR technique has been widely applied to measure the displacement caused by diverse natural phenomena such as earthquakes, volcanic activities, and land subsidences (Amelung et al., 1999; Galloway et al., 1998; Massonnet et al.,

1995; Massonnet et al., 1993). The recently developed time-series interferometric techniques using multi-temporal data acquired at multiple times have improved the accuracy of displacement estimation by extracting the error sources such as tropospheric phase delay, orbital ramps, DEM error. The representative methods are persistent scatterer interferometry (PSInSAR), small baseline subset algorithm (SBAS), and Stanford method for persistent scatterer (StaMPS) (Berardino et al., 2002; Ferretti et al., 2001; Hooper, 2008; Jung et al., 2014).

Despite the robustness of InSAR and DInSAR techniques, the measurement accuracy can be degraded where the contribution of the phase noise in pixels is severe. As mentioned above, the phase of complex value is related to the distance and scattering characteristics of the resolution cell. If the scattering phase is identical at different acquisition time and the acquisition position is exactly identical, the scattering phase in target media can be perfectly canceled in interferometry and the phase is reliable. This state is called “coherent”. However, this case is unusual because the states of the scatterers are perturbed due to the meteorological changes such as the wind, rain, and snow, etc. and artificial changes such as agricultural activities, construction, and the collapse of man-made structures. If the state of the target is totally changed, the measurement of displacement fails. The similarity degree of complex values of two observations can quantitatively be estimated, which is referred as “coherence”. Thus, high coherence ensures high reliability, meanwhile the low coherence implies the inaccurate measurement. In this perspective, the low coherence could be a weakness of InSAR system for the purpose of measuring the displacement. Meanwhile, the applications using this characteristic of the coherence have been proposed, hence, the coherence involves the information related how the scatterers in resolution cells respond to the natural phenome such as the wind, and soil moisture change. Consequently, the land cover classification methods based on the coherence have been suggested. (J. Askne et al., 1993; Bruzzone et al., 2004).

Also, the coherence can be used to assess the change detection and damage detection. The phase is disturbed even by the subtle morphological and positional changes. Hence, this change can be captured in phase disturbance estimator, coherence. Some researchers reported that the track made by the vehicle can be detected using interferometric coherence, and it demonstrated the sensitivity of coherence as change detector (Corr et al., 1998; Preiss & Stacy, 2006). Similarly, the damage maps have been derived after disasters such as flood, and earthquake (Fielding et al., 2005; Geudtner et al., 1996; Hoffmann, 2007; Yonezawa et al., 2001).

As the development of SAR system is accelerating, currently developed airborne and spaceborne SAR systems have been designed to acquire the full-polarimetric SAR (PolSAR) images which play the key roles to reveal the propagation and scattering mechanism. The polarimetric SAR is invaluable to decompose the observed scattering mechanism to the elementary components such as surface, double, and volume scattering. The applications based on PolSAR include the image classification, change detection, image segmentation (Shane R Cloude et al., 1997; J.-S. Lee et al., 1994; Park et al., 2013; Sato et al., 2012; J. Van Zyl et al., 1992).

The two main SAR applications can be combined to solve the uncertainty of physical and morphological properties of natural media. The techniques utilizing both interferometry and polarimetry are referred as “Polarimetric SAR interferometry (PolInSAR)”. The interferometer which uses more than two SAR data can measure the topographic height using phase of complex values. However, the conventional interferometric system operating with a single-polarization and a single-frequency is difficult to extract the scattering mechanism which the microwave interacts the scatterers of the scenes because the number of the measurement is not enough to extract the parameters associated with the scattering process. Also, the interferometric observations using single-polarization do not explain the exact location of scattering phase center of the target which depends on

polarization and wavelength of a system parameter and physical structure and geometrical parameters. To overcome the limitations of the conventional interferometry, the PolInSAR data is one of the promising ways because it increases the number of observations which relevant to scattering process of the target. A number of innovative approaches utilizing PolInSAR techniques have been suggested to extract the model parameters of forest and glacier having multi-layers (S. R. Cloude et al., 1998; Lavallo et al., 2012; Maxim Neumann et al., 2010; Konstantinos P Papathanassiou et al., 2001).

After the first launch of spaceborne SAR sensor (SEASAT), a number of spaceborne and airborne SAR systems have been developed and operated. Depending on the goal of the mission, they use different frequencies and operating strategies. The innovative experiments have been conducted to measure the natural phenomena and understand the physical mechanisms. Therefore, the continuously the techniques to utilize the SAR system need to be designed and improved.

1.2. Motivations

Natural disasters can cause serious massive damage to the property, social infrastructure, natural resources, and heavy casualties. For the rapid response to the disaster event and efficient recovery, the accurate and timely delivered information of damage is essential. Consequently, the technique to accurately detect the damaged area using remote sensing data has been one of the main issues in Earth and Environmental science field.

Disaster detection using remote sensing data is key techniques for the generation of global-scale damage maps after natural hazards (Yonezawa & Takeuchi, 2001, Gamba, et al., 2007, Matsuoka & Yamazaki, 2004(Yun et al., 2015)). In the past decades, several approaches of change detection using visible and near-infrared data

have been proposed (Collins et al., 1996; Singh, 1989). These approaches, however, have not always been successful in detecting changes in the presence of canopy cover because optical sensors measure primarily the surface reflectivity. Also, the cloud cover can limit the availability of proper data. Conversely, synthetic aperture radars (SARs) microwaves can penetrate forest canopies and obtain structural information about the underlying surface, especially at longer wavelengths. In addition, remote sensing with radars has several advantages, such as independence of acquisition from cloud cover and sun illumination. These advantages are critical in many practical situations because they extend the temporal and spatial applicability of SAR-based change detection techniques and play an invaluable role as a complementary tool to the other remote sensing data.

Change detection approaches using SAR data are categorized into incoherent and coherent (Preiss, Douglas, et al., 2006). Incoherent change detection involves comparison of backscattering amplitude between SAR data, generally by interpreting the difference or ratio of the SAR intensity acquired before and after the event to be detected (Dekker, 1998; Gong et al., 2012; Giovanni Nico et al., 2000; Rignot et al., 1993). In order to enhance the changed area, log ratio and amplitude normalized differences were also introduced (Bovolo et al., 2005; G. Nico et al., 2000). Also, incoherent change detection was performed with a filtering method in order to reduce false alarms (Dekker, 1998; White et al., 1990). These efforts were further developed into unsupervised change detection techniques that automatically determine the threshold value (Moser et al., 2006b).

On the other hand, coherent change detection (CCD) techniques utilize the interferometric correlation estimated between interferometric pairs of SAR images (Azzedine Bouaraba et al., 2012; Grey et al., 2003; Novak, 2005; Oishi et al., 2009; Yonezawa & Takeuchi, 2001). Analysis of cross-correlation is able to provide information about changes in scattering properties, including dielectric and structural.

Many CCD techniques have produced excellent results in detecting subtle changes induced by natural hazards and human activities (A Bouaraba et al., 2012; Geudtner et al., 1996; G. Nico et al., 2000; Preiss, Douglas, et al., 2006). These techniques were based on the statistics of the coherence and difference in the coherence magnitude (A Bouaraba et al., 2012; Grey et al., 2003). Some researchers have proposed change estimation based on hypothesis testing with likelihood-ratio-based statistics (Newey et al., 2012). This method has been further extended into polarimetric coherence cases (Barber, 2015). Furthermore, the coherences generated from three-pass data have been used to reduce the false alarm rate induced by vegetation (Barber et al., 2012). Other researchers have adopted multispectral land-cover classification in CCD using a Bayesian approach (Yu et al., 2014). In (Wahl et al., 2016), a new estimator was proposed to account for false alarms associated with a low cluster-to-noise ratio.

So far, however, the physical process that affects the statistics of the interferometric phase has not been fully considered in CCD techniques. Coherence is affected by a variety of components such as radar geometry, radar parameters, and surface conditions. Temporal decorrelation, in particular, is a mixture of natural changes and changes possibly associated with disaster events. Thus, ambiguities in conventional CCD techniques still remain where temporal decorrelation caused by natural phenomena is dominant such as over vegetated areas, which are likely affected by the wind or seasonal changes. When decorrelation caused by a certain event is coupled with temporal decorrelation from wind or rain, isolating the two different decorrelation sources is difficult and leads to poor change detection performance. Therefore, it is necessary to understand the effect of temporal decorrelation on the interferometric coherence of both natural processes and major events for isolating the natural changes from changes caused by the major event.

Also, the damage delineation method mainly utilized the single threshold to

detect the damaged area because they implement the spatial information only using one or two interferometric pairs. However, the uncertainty can arise when the scatterers with different physical properties react differently to the natural disasters. The high false alarm and low true detection can be severe if input images contain a variety of surface types. The problem cannot be overlooked even in the forested area, because the canopy height, spatial density of tree, and attenuation of microwave also affect the interferometric coherence. Therefore, the strategy to set different criteria in pixel by pixel is required.

Recently advanced SAR system can obtain the full-polarimetric SAR images which are also used in interferometry. The change detection techniques using multi-polarization SAR data successfully estimated to change by focusing on the on the image magnitude (Moser et al., 2006a; Rignot & Zyl, 1993). Meanwhile, analysis using the complex correlation of multi-temporal SAR data for quad-polarimetric SAR data is not fully exploited even though it has potential to detect changes successfully. In addition, the full-polarimetric interferometric SAR data measure the different phase centers with different polarization. Therefore, a new technique using multi-temporal and full-polarimetric data for change detection needs to be evaluated.

1.3. Purpose of Research

In the previous subsection, the possible reasons were outlined to degrade the performance of damage mapping using only coherence. To overcome the problems and obtain the desired result might be relied on what information can be derived and how to apply them. The main concept of this study starts from that the additional information to discriminate the contribution of damage and natural phenomena can be found in the multitemporal dataset. The historical behavior of coherences involved in multi-temporal data before the disaster can provide the statistical distribution of value which is associated with the natural phenomena. However, the

exploitation of decorrelation sources in multi-temporal data is fundamentally preceded before the damage assessment. The coherence is determined by diverse decorrelation sources. In particular, the temporal decorrelation severely affects the coherence in the multitemporal dataset which has a long temporal baseline (i.e. a few days to a few years). Therefore, the temporal decorrelation model for multi-temporal data should be formulated to explain the coherence behavior. Then, the proposed model will be extended to the application of change detection. At the same time, the potential of the coherence model to extend to the polarization issue is also taken into consideration.

This research aims to estimate the damaged area caused by the disaster based on the coherence calculated from single-polarimetric and full-polarimetric SAR data using temporal decorrelation model. Firstly, the coherent behavior will be interpreted based on the model, then, the inversion process for the extraction of the parameters will be designed for single-polarized data. For a case study, changed area by the volcanic ash deposit which was emitted due to the eruption of Kirishima volcano in January 2011 will be estimated. Secondly, the coherent changes will be analyzed for multi-temporal and full-polarimetric SAR data. Then, the inversion of the temporal decorrelation model and change detection method will be designed. The study will focus on the Lake fire which occurred in July 2015 in California, USA.

The main objectives can be summarized as followings

- Formulation of the temporal decorrelation model for the multitemporal dataset which has a long temporal baseline
- Development of coherence change detection technique for multi-temporal and single-polarized SAR data
- Development and evaluation of coherence change detection for multi-temporal and quad-polarized SAR data.

1.4. Outline

This research addresses the three main topics: coherence model, damage detection using single-polarization and multi-temporal data and damage detection using fully-polarized multi-temporal data. Each topic is organized as follows.

In Chapter 2, the interferometric decorrelation sources are reviewed and a temporal decorrelation model to interpret coherence observations from multi-temporal and single-polarization SAR data is proposed.

In Chapter 3, how to estimate the model parameters of the temporal decorrelation model for coherence change detection is described. The strategy is evaluated using Japan Aerospace Exploration Agency's (JAXA's) ALOS-PALSAR data acquired before and after the eruption of the Kirishima volcano in Japan in 2011. Using in-situ data, validation of result and discussion about the limitations of the approach is explained.

In Chapter 4, the damage mapping algorithm using coherence model for the multi-temporal and full-polarized data. Accordingly, the inversion method and damage assessment are discussed. The approach was applied to the UAVSAR data for detection of burnt area by Lake Fire, 2015 which occurred in California, US.

In Chapter 5, the study is summarized and the future study is discussed.

Chapter 2.

Estimation of complex correlation and decorrelation sources

2.1. Estimation of complex correlation

The complex correlation is defined as

$$\gamma = \frac{\langle s_1 s_2^* \rangle}{\sqrt{\langle s_1 s_1^* \rangle \langle s_2 s_2^* \rangle}} = |\gamma| \exp(j\phi_0) \quad (2.1)$$

where s_1 and s_2 are the complex pixel values of two SAR images, and the angular brackets denote ensemble averaging (Zebker et al., 1992). The magnitude of the complex correlation coefficient, with $0 \leq |\gamma| \leq 1$, is often called simply “coherence”. The coherence is used as the estimator of phase noise. The argument of γ is the effective phase difference which contains the flat-earth, topographic, displacement and atmospheric phase delay contributions.

The properties of complex correlation can be understood using the statistical approach because the complex values of SAR images, including the real and imaginary part of complex values, usually have circular Gaussian distribution. The joint probability density function of the interferometric phase ϕ and amplitude a can be written as (Touzi et al., 1999)

$$\begin{aligned} pdf(a, \phi) \\ = \frac{2L(La)^L}{\pi \varsigma^{L+1} (1 - |\gamma|^2) \Gamma(L)} \exp\left(\frac{2|\gamma|La \cos(\phi - \phi_0)}{\varsigma(1 - |\gamma|^2)}\right) K_{L-1}\left(\frac{2La}{\varsigma(1 - |\gamma|^2)}\right) \end{aligned} \quad (2.2)$$

where $\varsigma = \sqrt{E(s_1)E(s_2)}$ and $K_{L-1}()$ is the modified Bessel function. Γ is the gamma function for the looks, L . By integrating over amplitude, a , the marginal probability density function of the phase, $pdf(a, \phi)$, can be obtained as

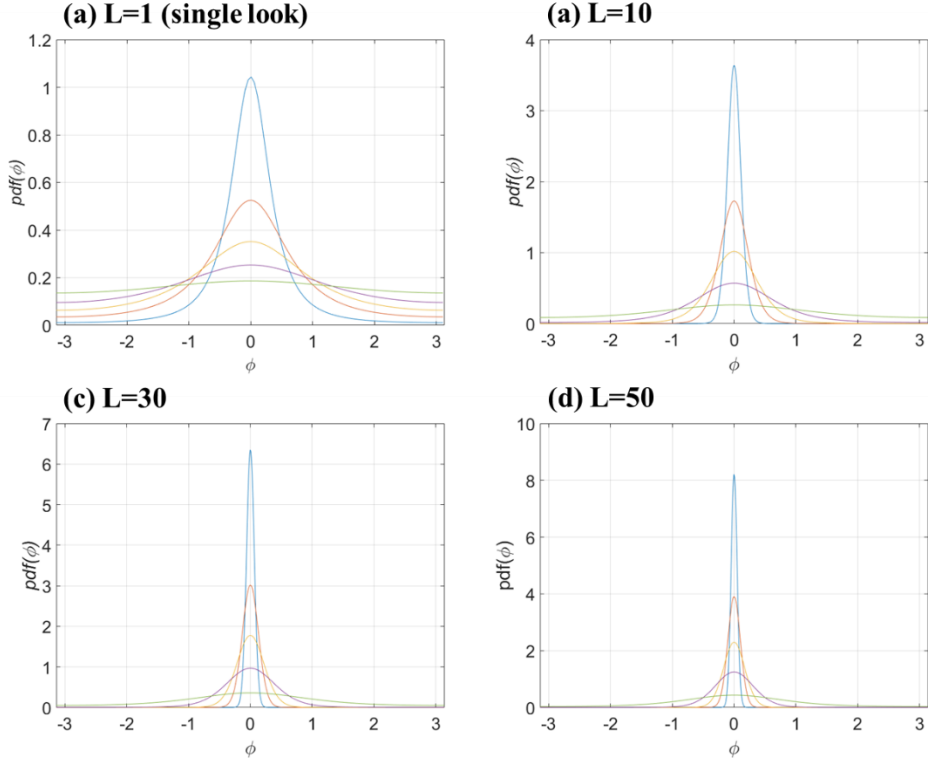


Fig. 2. 1. Probability density function of interferometric phase for coherence and the number of looks. Coherence levels range from 0.9, 0.7, 0.5, 0.3, and 0.1. The narrowest distribution corresponds to 0.9 coherence.

$pdf(\phi)$

$$\begin{aligned}
 &= \frac{(1 - |\gamma|^2)^L}{2\pi} \left[\frac{\Gamma(2L - 1)}{|\Gamma(L)|^2 2^{2(L-1)}} \left\{ \frac{(2L - 1)\beta}{(1 - \beta^2)^{L+\frac{1}{2}}} \left(\frac{\pi}{2} + \arcsin\beta \right) + \frac{1}{(1 - \beta^2)^L} \right\} \right. \\
 &\quad \left. + \frac{1}{2(L - 1)} \sum_{r=0}^{L-2} \frac{\Gamma\left(L - \frac{1}{2}\right)}{\Gamma\left(L - \frac{1}{2} - r\right)} \frac{\Gamma(L - 1 - r)}{\Gamma(L - 1)} \frac{1 + (2r + 1)\beta^2}{(1 - \beta^2)^{r+2}} \right] \quad (2.3)
 \end{aligned}$$

$$\beta = |\gamma| \cos(\phi - \phi_0) \quad (2.4)$$

Then, the probability density function of interferometric phase, ϕ , for variables γ , L , ϕ_0 can be plotted as shown in Fig. 2.1. The variance of interferometric phase can be calculated based on the probability density function as

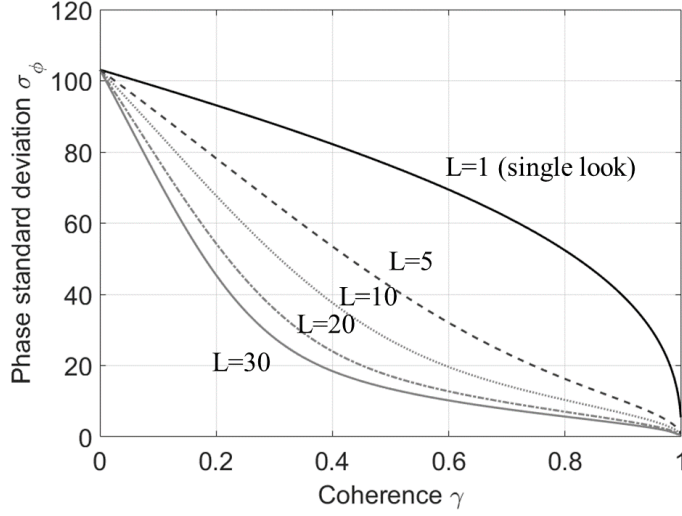


Fig. 2. 2. Phase standard deviation for coherence and number of looks.

$$\int_{-\pi}^{\pi} [\phi - E(\phi)]^2 p d f(\phi) d \phi \quad (2.5)$$

Based on the probability density functions of interferometric phase, the increase of the number of looks makes the shape of distribution narrow. Hence, by applying the sufficient looks, the measured phase is expected to be close to true phase. Also, the high coherence value tends to yield narrow distribution, and it implies that the phase is sufficiently reliable. Similarly, the phase standard deviation increase as the coherence decrease as shown in Fig.2.2. For the distributed target of single look images, the phase standard deviation is relatively high, even though the coherence is high. Therefore, the coherence is an indicator or a measure for the accuracy of interferometric phase having a nonlinear relationship between the phase standard deviation and coherence.

The estimator of coherence could have a bias if the sufficient number of looks is not used. The bias in the coherence magnitude d can be described:

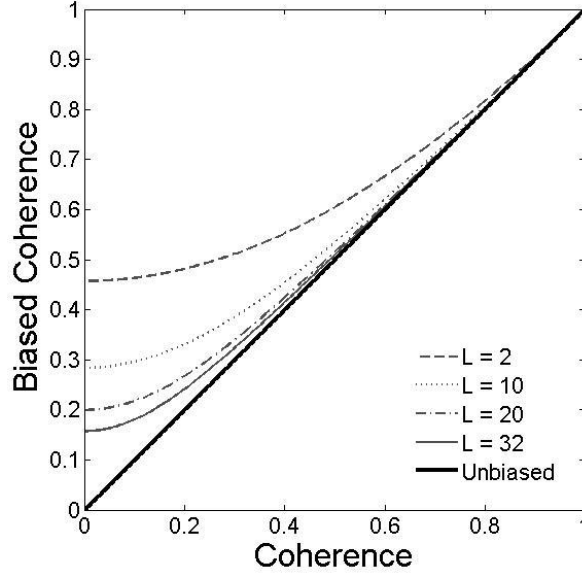


Fig. 2. 3. Biased coherence versus true coherence for a various number of looks.

$$E(d) = \frac{\Gamma(L)\Gamma\left(1 + \frac{1}{2}\right)}{\Gamma\left(L + \frac{1}{2}\right)} \cdot {}_3F_2\left(\frac{3}{2}, L, L; L + \frac{1}{2}; 1; D^2\right) (1 - D^2)^L \quad (2.6)$$

where D is the unbiased coherence (true coherence), and L is the number of looks (Touzi et al., 1999). Fig 2.3. shows the relation between the unbiased coherence and the biased coherence with regarding the number of looks. It is clearly observed that the estimation of coherence is more biased at the lower coherence or the smaller estimation window. Thus, the efficient way to estimate the coherence correctly is the use of the sufficient number of looks.

2.2. Decorrelation sources

In general, the coherence ranges between 0 and 1. For completely coherent scatterers, $\gamma = 1$; however, this condition is extremely uncommon in repeat-pass interferometry owing to a variety of decorrelation effects. Decorrelation can be divided into four components: geometric, volumetric, temporal, and thermal

decorrelation (Bamler et al., 1995; Wei et al., 2010; Zebker & Villasenor, 1992).

$$\gamma = \gamma_{geometric} \gamma_{thermal} \gamma_{temporal \& volume} \quad (2.7)$$

2.2.1. Thermal decorrelation

Thermal decorrelation is determined by thermal noise in the interferometric instrument. Thermal noise is typically assumed to have Circular-Gaussian statistics. The scattered signal consists of signal parts and noise parts, such as

$$s_1 = c + n_1 \quad s_2 = c + n_2 \quad (2.8)$$

The coherence determined by only thermal decorrelation can be described as (Bamler & Just, 1995; Zebker & Villasenor, 1992),

$$\gamma_{thermal} = \frac{\langle cc^* + cn_2^* + c^*n_1 + n_1n_2^* \rangle}{\sqrt{\langle cc^* + 2cn_1^* + n_1n_1^* \rangle \langle cc^* + 2cn_2^* + n_2n_2^* \rangle}} \quad (2.9)$$

Then the noise parts are assumed to be uncorrelated and the signal is uncorrelated with the noise parts,

$$E(n) = E(n_1) = E(n_2) \quad (2.10)$$

$$\gamma_{thermal} = \frac{\langle cc^* \rangle}{\sqrt{\langle (cc^* + nn^*)^2 \rangle}} = \frac{|c|^2}{|c|^2 + |n|^2} \quad (2.11)$$

The signal to noise ratio is $|c|^2/|n|^2$ and thermal decorrelation can be written as

$$\gamma_{thermal} = \frac{1}{1 + SNR^{-1}} \quad (2.12)$$

Consequently, the thermal decorrelation is related to the signal-to-noise ratio (SNR) of the scatterers illuminated by radar signal (Wei & Sandwell, 2010; Zebker & Villasenor, 1992). The variance of the interferometric phase depends on the SNR. Thus, pixels with high SNR generally exhibit high coherence. Because the magnitude of the returned SAR signal varies depending on the response of the scatterers, the thermal decorrelation also varies pixel by pixel. The SNR can be

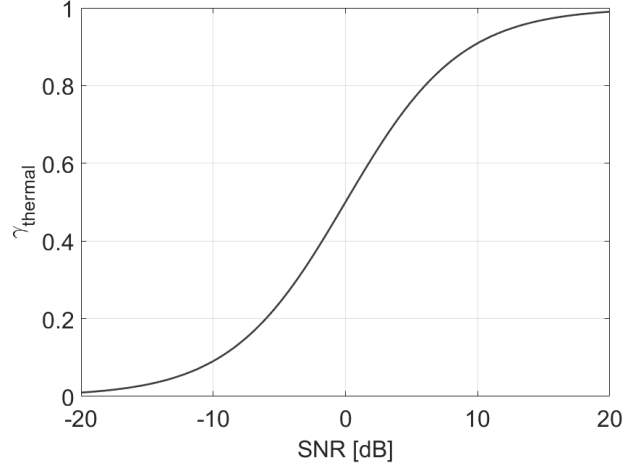


Fig. 2. 4. Thermal decorrelation as a function of SNR.

estimated by dividing the radar backscattering coefficient (σ^0) by the noise equivalent sigma zero (NESZ) (Sun et al., 2010).

2.2.2. Geometric decorrelation

Geometrical decorrelation is caused by the shift of wavenumber spectra when data acquired at different incidence angle from different acquisition positions of two sensors (Gatelli et al., 1994). The relative shift of the ground wavenumber is related to the baseline, and the local slope angle. If let α be local slope angle, the ground range wavenumber k_y can be described as,

$$k_y = \frac{4\pi}{\lambda} \sin(\theta - \alpha) = \frac{4\pi f}{c} \sin(\theta - \alpha) \quad (2.13)$$

Then, its deviation can explain the variation of k_y as a change of the look angle, $\Delta\theta$.

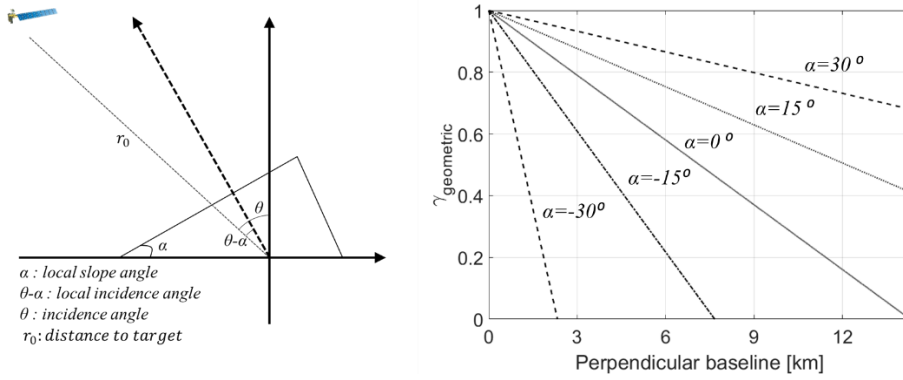


Fig. 2. 5. Geometry of SAR sensor (left) and geometric decorrelation for a function of baseline and slope angle in the case of ALOS PALSAR, FBS mode.

$$\Delta k_y = \frac{4\pi f \Delta \theta}{c} \cos(\theta - \alpha) \quad (2.14)$$

The ground wavenumber shift can be expressed as the expression of equivalent frequency shift, Δf . This can be obtained by differentiation of above equation.

$$\Delta f = -\frac{f \Delta \theta}{\tan(\theta - \alpha)} = -\frac{c B_n}{r_0 \lambda \tan(\theta - \alpha)} \quad (2.15)$$

The expression means that the backscattered signal contained the shifted spectral components. The scattered signal of two images acquired at different positions is totally uncorrelated, as the frequency shift Δf equal to bandwidth, W . Based on this, the critical baseline is determined as (Gatelli et al., 1994),

$$|B_{crit.}| = \left| \frac{W r_0 \lambda \tan(\theta - \alpha)}{c} \right| \quad (2.16)$$

Additionally, the spatial resolution of range direction is determined the bandwidth of the chirp signal of SAR sensor. Thus, the critical baseline can be expressed as a function of resolution, ρ_r .

$$|B_{crit.}| = \left| \frac{r_0 \lambda \tan(\theta - \alpha)}{2 \rho_r} \right| \quad (2.17)$$

Now, the geometrical decorrelation can be defined using the calculated critical baseline (Gatelli et al., 1994; Zebker & Villasenor, 1992).

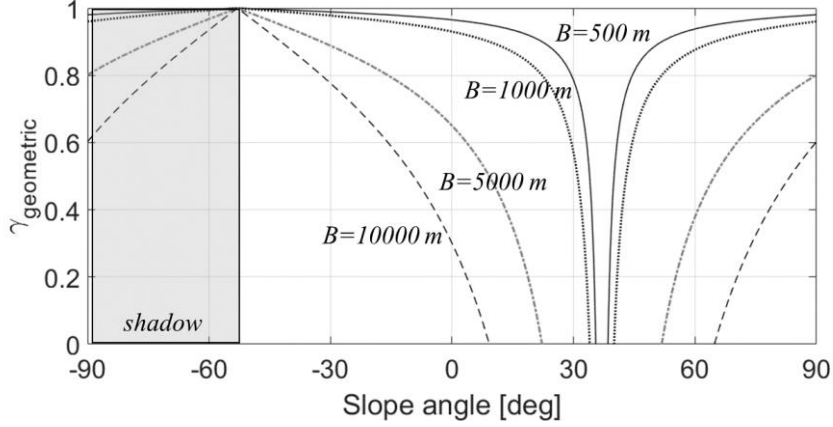


Fig. 2. 6. Geometric decorrelation for a function of slope angle with perpendicular baseline, in the case of ALOS PALSAR, FBS mode.

$$\gamma_{geometric} = 1 - \frac{B_{\perp}}{B_{crit}} \quad (2.18)$$

The formulated geometrical decorrelation is determined by the geometric parameter such as distance to the target, incidence angle, and local slope angle, and the system parameters such as wavelength, and bandwidth. Thus, the geometrical decorrelation is different depending on the SAR sensors and location of scatterers. In the case of ALOS PALSAR, the fine beam single (FBS) and fine beam double (FBD) mode are usually used for SAR interferometry. The bandwidths of FBS and FBD are 28 MHz and FBD 14 MHz, respectively. Thus, the critical baselines are $\sim 14\text{km}$ and 7 km for FBS and FBD modes. The geometric decorrelation of FBS mode was plotted in Fig. 2.5. As expected, the longer baseline results in the lower coherence. Since the geometric decorrelation is sensitive to the slope angle as well, the effect of the geometric decorrelation varies on the locations. Also, the geometric decorrelation can be plotted as a function of slope angle as shown in Fig. 2.6. When the vector of the line of sight is normal to the plane of the slope, $\theta = \alpha$, the geometric decorrelation dramatically affect the coherence so that coherence become zero. In contrast when the line of sight vector is parallel to the slope plane, the geometric

coherence is almost 1. However, if the slope angle is less than $\theta - 90^\circ$, the transmitted signal of SAR sensor cannot reach the surface. This is known as “shadow effect”, which is present in SAR images. It should be taken into account for analysis of geometric decorrelation. Therefore, coherence can be estimated in the range of slope angle, $\theta - 90^\circ < \alpha < \theta$. The common band filtering, which filter out the uncorrelated frequency parts of the two scenes, and utilize the only common parts (Wei & Sandwell, 2010).

2.2.3. Volumetric decorrelation

Volumetric decorrelation originates from the scattering of radar microwaves within a volume such as forest canopies (J. I. Askne et al., 1997; Treuhaft et al., 2000; Zebker & Villasenor, 1992). For simplicity of the model, here the volume layer is assumed as uniformly distributed and randomly oriented scattering elements with an underlying surface. If the vertical coordinate is denoted as z , it can be assumed that the surface layer is located at $z = z_0$ and the height of the volume layer can be $z = z_0 + h_v$, where h_v is the canopy height. When the sensor illuminates the target media with slightly different distance (or angular angle), the interferometric complex coherence in the volume layer can be formulated by using the structure function, $p(z)$ as:

$$\begin{aligned} \gamma^v &= \frac{\langle s_1 s_2^* \rangle}{\sqrt{\langle s_1 s_1^* \rangle \langle s_2 s_2^* \rangle}} = \frac{\int \langle \rho_1(z) \rho_2^*(z) \rangle dz}{\sqrt{\int \langle \rho_1(z) \rho_1^*(z) \rangle dz \int \langle \rho_2(z) \rho_2^*(z) \rangle dz}} \\ &= \frac{\int_0^{h_v} p(z) e^{ik_z z} dz}{\int_0^{h_v} p(z') dz} \end{aligned} \quad (2.19)$$

$$\rho_2(z) = \rho_1(z) e^{ik_z z} \quad (2.20)$$

where $\rho_1(z)$ and $\rho_2(z)$ are the complex reflectivity per unit length. Here, k_z is the vertical wavenumber:

$$k_z = \frac{4\pi\Delta\theta}{\lambda \sin \theta} = \frac{4\pi B_{perp}}{\lambda R_0 \sin \theta} \quad (2.21)$$

In Eq. (2.21), λ is the wavelength of radar signal, θ is the mean look angle, and $\Delta\theta$ is the difference between two look vectors of the interferometric pair, which is a function of the slant range distance from the sensor to the target, R_0 , and the perpendicular baseline, B_{perp} . The structure function, $p(z)$, which physically means the attenuated backscatter per vertical unit length, is determined by the mean backscatter density of the volume layer, m_v , the attenuation of wave propagation in the volume layer and thickness of volume layer.

In order to understand the effects of the volume layer only, here, the ground scattering contribution is ignored first, and later the model will contain the ground effect also. In order to depict the vertical structure function, one frequently assumes the uniform profiles and exponential profiles. If the uniform profile is introduced, the Eq.(2.19) is rewritten as:

$$\gamma^v = \frac{e^{ih_vk_z} - 1}{ih_vk_z} = e^{\frac{ih_vk_z}{2}} \frac{\sin(\frac{h_vk_z}{2})}{\frac{h_vk_z}{2}} = e^{\frac{ih_vk_z}{2}} \text{sinc}\left(\frac{h_vk_z}{2}\right) \quad (2.22)$$

The model is simplified as the simple Sinc function which has two variables of volume canopy height and vertical wavenumber. This model is beneficial in the estimation of canopy height when the quantity of independent parameter is limited as in single-pol space-borne SAR system (Balzter, 2001; Olesk et al., 2015; Praks et al., 2012).

If the exponential profile is assumed for the attenuation, the structural function can be expressed as a one-way extinction coefficient, σ_e :

$$p_v(z) = m_v \exp(2\sigma_e(z' - h_v)\sec\theta), \quad (2.23)$$

The numerator in Eq (2.19) is rearranged as:

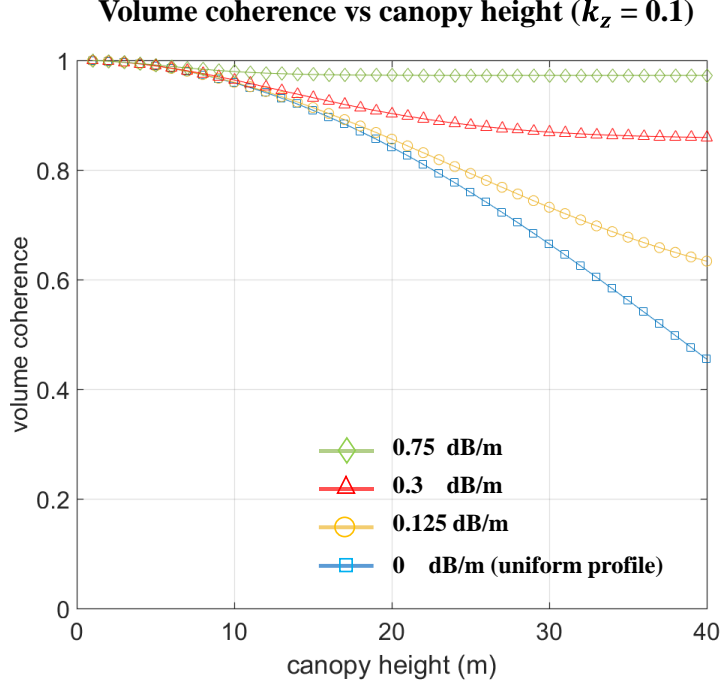


Fig. 2. 7. Volume coherence for functions of extinction coefficient and canopy height. The volume coherence at 0 dB/m is coincident to the case that structure function is assumed as constant.

$$\begin{aligned}
 \int_0^{h_v} p(z') e^{ik_z z'} dz' &= \int_0^{h_v} m_v e^{\frac{2\sigma_e(z'-h_v)}{\cos\theta}} e^{ik_z z'} dz' \\
 &= \frac{m_v}{\frac{2\sigma_e}{\cos\theta} + ik_z} \left[e^{ik_z h_v} - e^{\frac{-2\sigma_e h_v}{\cos\theta}} \right]
 \end{aligned} \tag{2.24}$$

Also, the denominator is rewritten as:

$$\begin{aligned}
 \int_0^{h_v} p(z') dz' &= \int_0^{h_v} m_v \exp(2\sigma_e(z' - h_v)\sec\theta) dz' \\
 &= m_v \frac{\cos\theta}{2\sigma_e} \left[1 - e^{\frac{-2\sigma_e h_v}{\cos\theta}} \right]
 \end{aligned} \tag{2.25}$$

Thus, the interferometric complex coherence of volume can now be:

$$\gamma^v = \frac{2\sigma_e \sec\theta}{2\sigma_e \sec\theta + ik_z} \left[\frac{e^{ik_z h_v} - e^{\frac{-2\sigma_e h_v}{\cos\theta}}}{1 - e^{\frac{-2\sigma_e h_v}{\cos\theta}}} \right] \tag{2.26}$$

Now, the volumetric coherence in volume layer is determined by the wavenumber,

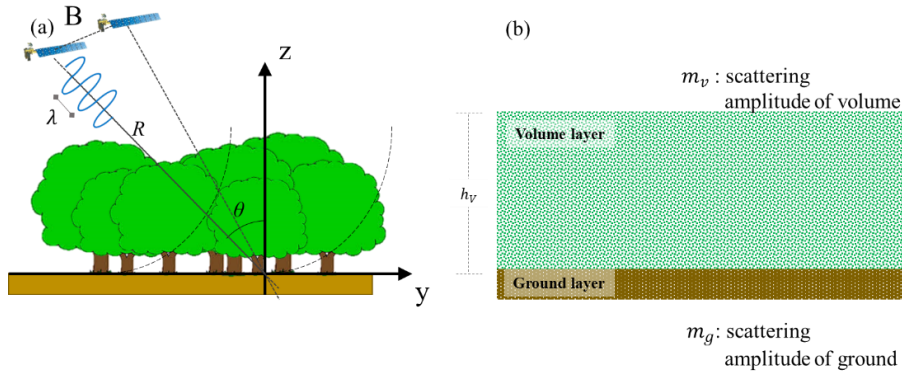


Fig. 2. 8. Schematic representation of random volume over ground model. (a) Actual geometry of sensors and forest, and (b) simplified two layers model.

canopy height, and extinction coefficient, and incidence angle. As shown in Fig. 2. 7, the volume coherence model shows slowly decreasing trend as the canopy height increase at high extinction coefficient. This is because the transmitted signal from radar less penetrated the target media, and the interferometric phase does not significantly vary along the vertical direction. Meanwhile, at the zero-extinction or uniform profiles, the interferometric phases from bottom to top evenly contribute the volume coherence, thus, the volume coherence decreases fast. This result implies that in real nature, the volume decorrelation is more severe in the forest with sparse branches than the dense branches.

The wave with long wavelength (i.e. L-band and P-band) often penetrates the volume layer and reaches to the rough surface. The Radom Volume over Ground (RVoG) model depicts the coherence model including volume and ground layers (S. R. Cloude & Papathanassiou, 1998; Konstantinos P Papathanassiou & Cloude, 2001). In the case of the ground layer, the complex coherence is described as:

$$\gamma^g = e^{ik_z z_0} \quad (2.27)$$

Hence, the magnitude of the coherence of ground layer does not change, but the phase is determined by the altitude of the ground lever and vertical wavenumber.

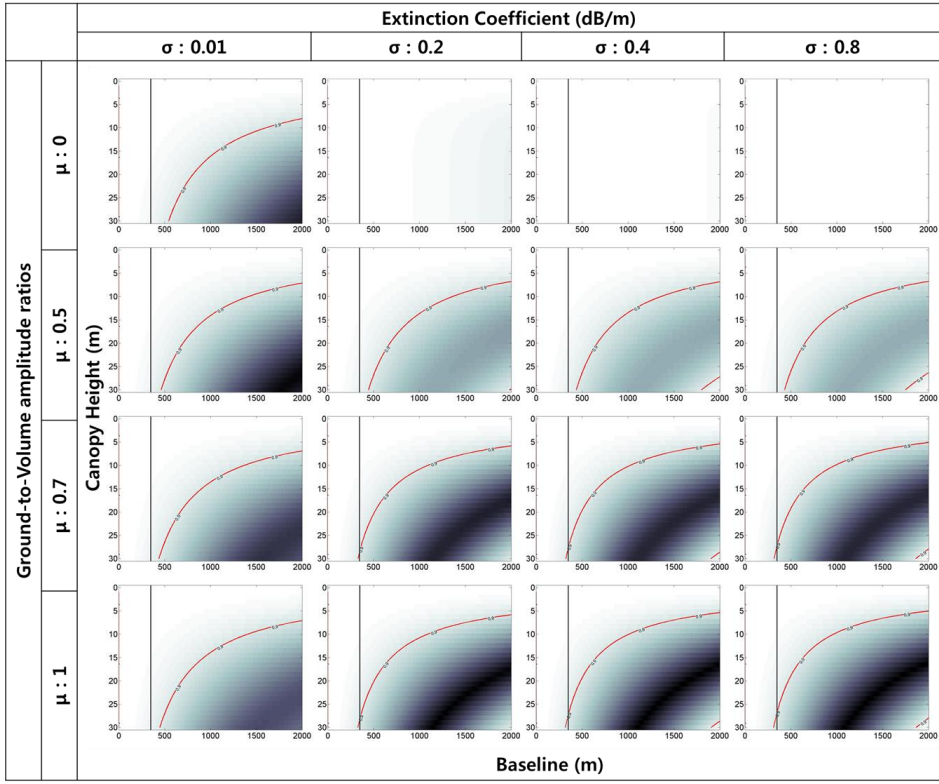


Fig. 2. 9. Volumetric decorrelation changes for a function of ground-to-volume ratio, extinction coefficient, baseline and volumetric height.

The coherence depicted in RVoG model is explained as two contributions of ground and volume layer. Thus, the structure function now has the term related to the ground layer.

$$p_{gv}(z) = m_v e^{(2\sigma_e(z'-h_v)\sec\theta)} + e^{\frac{-2\sigma_e h_v}{\cos\theta}} m_g \delta(z - z_0) \quad (2.28)$$

Thus, the final two-layer coherence model for the volume decorrelations can be expressed as follows:

$$\gamma(w) = e^{ik_z z_0} \frac{m_{0v}(w) \gamma^v e^{-ik_z z_0} + p_g m_g(w)}{m_{0v}(w) + p_g m_g(w)} = e^{ik_z z_0} \frac{\gamma^v e^{-ik_z z_0} + \mu(w)}{1 + \mu(w)} \quad (2.29)$$

$$p_g = e^{-2\sigma_e h_v / \cos\theta} \quad (2.30)$$

where $\delta(z - z_0)$ is delta function. m_g indicates the attenuated scattering from

$$m_{0v}(w) = \left(\frac{\cos\theta_0}{2\sigma_e} \left(1 - e^{-\frac{2\sigma_e h_v}{\cos\theta}} \right) \right) m_v(w). \quad (2.31)$$

$$\mu(w) = \frac{p_g m_g(w)}{m_{0v}(w)} = \frac{2\sigma_e e^{-\frac{2\sigma_e h_v}{\cos \theta}} m_g(w)}{\cos \theta_0 (1 - e^{-2\sigma_e h_v / \cos \theta}) m_v(w)} . \quad (2.32)$$

As a result, the volumetric decorrelation assuming two simplified layers have the structure parameters such as extinction coefficient, and volumetric height, system parameters such as the wavelength of the sensor, and geometric parameters such as baseline, and distance to the target from the sensor. Here, w represents the polarimetric scattering mechanism. Note that m_v and m_g are the polarization-dependent scattering cross-section of volume and ground layer respectively, meanwhile the extinction coefficient of volume layer, σ_e , does not change with polarization. Accordingly, the ground-to-volume ratio μ , which is a function of m_v and m_g , is polarization-dependent parameter. Hence, the coherence observed in forest area is effectively determined by the each contribution of the surface and volume layer. This characteristic is discriminatory property with the model considering only the volume layer.

The difference of incidence angle between two geometries at acquisitions is a function of the distance from sensor to target in slant range plane and the spatial baseline, B . The expected volumetric decorrelation based on the RVoG model can be simulated with the deterministic parameters such as extinction coefficient, canopy height, baseline, and ground-to-volume ratio as shown in Fig 2.9.

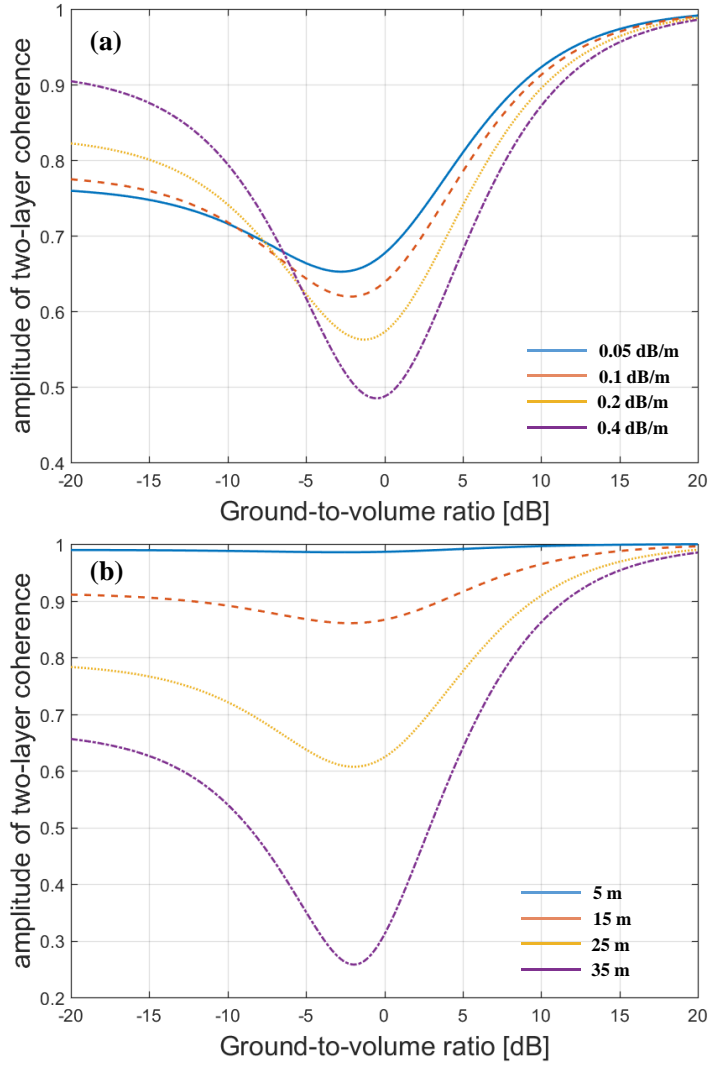


Fig. 2. 10. Volume coherence versus Ground-to-volume ratio with (a) extinction coefficients assuming the canopy height is 15 m and (b) canopy height assuming the extinction coefficient is 0.15 dB/m.

Fig. 2. 10 shows the relationship between the volume coherence and ground-to-volume ratio. High ground-to-volume ratio indicates the ground contribution is dominant, meanwhile, low ground-to-volume ratio represents the volume-dominant. It is worth noting that the amplitude of the coherence does not monotonically increase as the ground-to-volume ratio increase. When the volume contribution is dominant, the coherence decrease as a ground-to-volume ratio increase. Under the

condition that ground contribution is similar to the volume contribution, the coherence become low. Consequently, the minimum value is observed at some value between high and low ground-to-volume ratio. This is because the ground component make the effective phase center moves to the ground, and consequently, the complex coherence of ground and volume layer is mixed. After the order of the ground component is similar to the volume layer, the ground component is stronger as the ground-to-volume ratio increase. Hence, the coherence of two-layer model increases.

Also, it is important that a high extinction coefficient induces high coherences at the low ground-to-volume ratio, however, it leads to the low coherences at the high ground-to-volume ratio. As mentioned above, the high extinction represents that the signal is likely to return at top of the forest. Hence, the interferometric phase is less varied, the coherence is high. In contrast, the interferometric phase is more diverse when the extinction coefficient is low due to the high penetration. Adding the more ground components, the signal from the surface is stronger. It implies that interferometric phase is more varied along the vertical direction. The volume layer with high extinction is still influent on the coherence, thus, the coherence is relatively low. However, since the ground contribution is strong at low extinction, the coherence is mainly determined by the ground component, hence, the coherence could be high.

In Fig. 2. 10. (b), the coherence is depicted as the ground-to-volume ratios increase with the canopy height. The higher canopy height induces the more variation of coherence with the changes of the ground-to-volume ratio.

Recent research efforts using polarimetric SAR interferometry aim at retrieving the structural parameters of forests using a two-layer model in which the properties of coherence and interferometric phase are sensitive to forest vertical structure and height (S. R. Cloude & Papathanassiou, 1998; Konstantinos P Papathanassiou &

Cloude, 2001). The number of the unknowns used in the RVoG model is four ($h_v, \sigma_e, z_0, \mu_1$) and the number of observable is two in the case of acquisition of single-pol and single-pass interferometry. By incorporating the fully polarimetric and single-pass interferometric system, the two additional unknowns (μ_2, μ_3) corresponding to the newly added polarizations are involved the model, while the four additional observables are available. Thus, the RVoG model is able to interpret the volumetric decorrelation in polarimetric SAR interferometry (S. Cloude et al., 2003). However, the applications have been limited for only airborne SAR campaign experiments so far, because of the temporal decorrelation. The temporal decorrelation indicates the amount of decorrelation related to the physical, morphological, and dielectric changes of target scatterers. If the temporal decorrelation present, the coherence is also affected and the model parameters tend to be overestimated. It will be more discussed in the next subsection. If the temporal baseline is sufficiently short, such that temporal decorrelation is negligible as in the case of single-pass interferometry, the model can be used for estimation of the canopy height and other physical parameters. Temporal decorrelation can be controlled in the airborne-SAR campaign, thus, many studies describes the approaches with the airborne SAR data (M. Neumann et al., 2010; Konstantinos P Papathanassiou & Cloude, 2001). The current space-borne system to minimize the temporal decorrelation is TanDEM-X which operates the two coincident X-band SAR sensors with few temporal baseline (Krieger et al., 2007). Since TanDEM-X provides only single- and dual- polarization data, PolinSAR techniques using Dual-polarization have been proposed and demonstrated (Kugler et al., 2014)

In single-polarization SAR interferometry, since the quantity of the parameters exceeds that of observations, the RVoG model parameter cannot be accurately retrieved. The single-pol and single-pass interferometric pair measures the location of a phase center which is effectively determined by the systematic, geometric, and

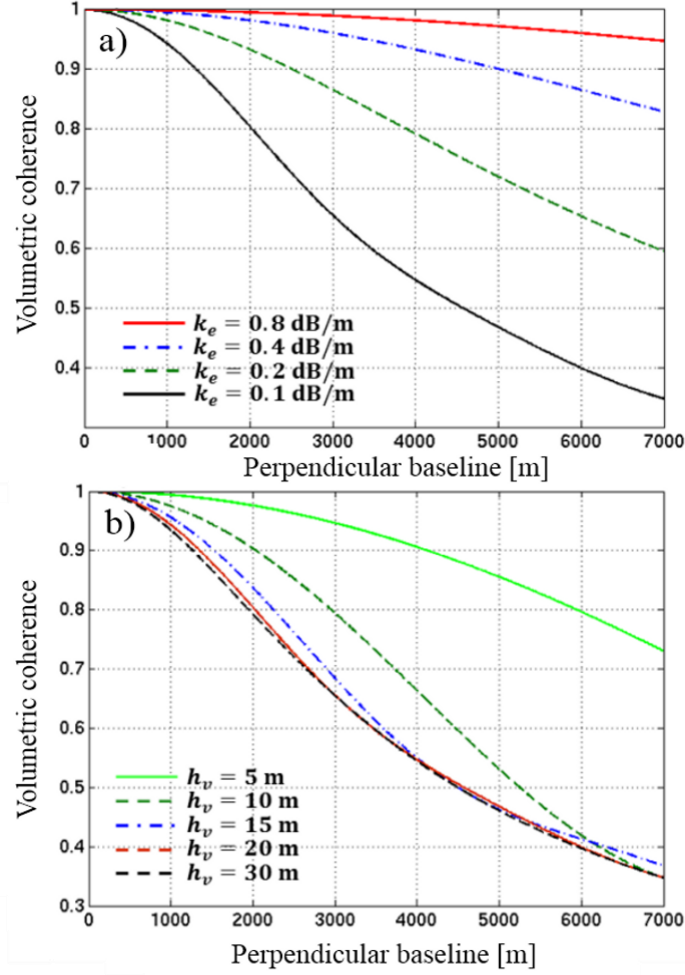


Fig. 2. 11. Coherence change using Random-Volume-over-Ground (RVoG) model for a variety of forest parameters: (a) As a function of wavenumber and extinction coefficient k_e assuming canopy height $h_v = 20$ m. (b) As a function of wavenumber and canopy height assuming vertical extinction 0.1 dB/m.

structural parameters. The conventional interferometric pair with single-polarization provides only one measurement, and it implies the interpretation is restricted and has an ambiguity without the prior information of forest.

If one is interested in the remaining decorrelation except for the volume decorrelation, the volume coherence needs to be estimated and compensated. As mentioned above, the accurate amount of volume decorrelation can be retrieval

under the case of single-pass interferometry with more than dual-polarizations. Alternatively, the conditions to minimize the volume coherence can be priory searched. In order to minimize the volumetric decorrelation, several assumptions can be incorporated into the RVoG model, depending on the properties of the forest and the characteristics of the interferometer. One of the robust ideas is to find the bounding conditions of perpendicular baseline. In practical, the forest parameter is unknown and uncontrollable unless the prior knowledge is given, meanwhile, the baseline is controllable. In this study, the volumetric decorrelation was bounded which is observed by ALOS-PALSAR to minimal value so that the observed total coherence is dominated by temporal decorrelation, which is key to estimating the changes in the imaged scenes. The RVoG coherence versus the perpendicular baseline for different values of canopy extinction coefficient and canopy height was plotted in Fig. 2. 11. The figure shows that the volumetric coherence is higher than 0.94 for perpendicular baselines smaller than 1 km assuming 20 m canopy height and 0.1 dB/m extinction coefficient. Therefore, in order to neglect the contribution of the volumetric decorrelation in the total observed coherence, use of an interferometric baseline shorter than 1 km (i.e., an interferometric wavenumber smaller than 0.10 rad/m) is recommended.

2.2.4. Temporal decorrelation

. Temporal decorrelation is related to the alteration of the position and dielectric changes of the scatterers, typically caused by wind, rain, snow, or other natural events (Rosen et al., 2000; Zebker & Villasenor, 1992). In single-pass interferometry, where two or more images are acquired simultaneously, there are no effects related to changes in scattering characteristics such as the motion of the scatterers and

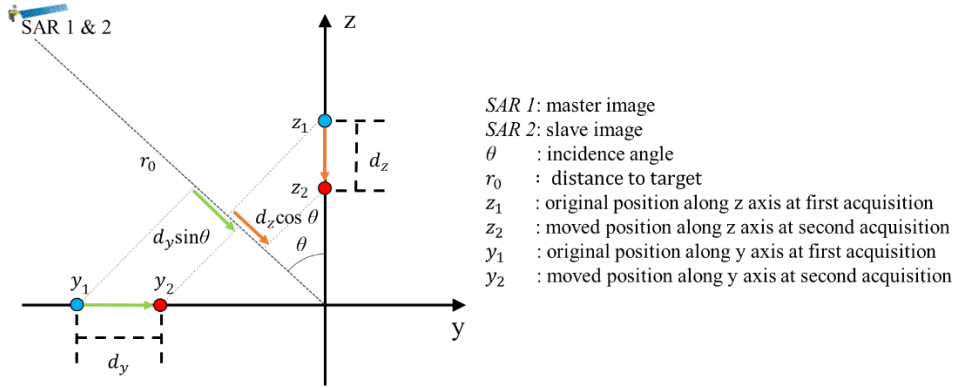


Fig. 2. 12. Schematic representation of scatterer motion for temporal decorrelation.

biological growth; thus, temporal decorrelation is negligible. However, in repeat-pass interferometry, where images are acquired at different times and look angles, the physical changes of scatterers over the time period, the temporal decorrelation could be observed.

The physical sources inducing the temporal decorrelation could be categorized into two groups. One is the decorrelation induced by the positional changes of scatterers, which is also known as motion-induced decorrelation (Lavalle et al., 2012; Zebker & Villasenor, 1992). The other is associated with the dielectric properties changes including soil moisture change, roughness changes, vertical structure profiles changes, and etc. (De Zan et al., 2014; Hajnsek et al., 2008; Morrison et al., 2011; Nesti et al., 1998; Zwieback et al., 2015). The former alters only the interferometric phase but does not induce the backscattering amplitude changes. Therefore, the coherence can be a good indicator to identify the motion-induced decorrelation. Meanwhile, the latter leads to the loss of coherence and may change the amplitude as well.

The explanation of the temporal decorrelation induced by the positional changes

usually adopts the Gaussian-static motions (Zebker & Villasenor, 1992). Let X , Y , and Z represent along-track, cross-track, and vertical axis, respectively and O represents the center of resolution cell. Then, the distance between antenna and resolution cell is assumed to be r . Let assume a target in resolution cell, and its coordinate as (x, y, z) . The phase variation of the pixels at the signal can be described as

$$s_1 = \iiint f_1(x, y, z) \exp \left\{ -i \frac{4\pi}{\lambda} (r + y \sin \theta - z \cos \theta) \right\} \times W(x, y) dx dy dz \quad (2.33)$$

where $f_1(x, y, z)$ is the complex backscatter density, λ is the wavelength, θ is the incidence angle, and $W(x, y)$ is the system impulse response. In revisited time, if the scatterers change their positions to other position, the signal from the second antenna can be written as

$$s_2 = \iiint f_2(x, y, z) \exp \left\{ -i \frac{4\pi}{\lambda} (r + y \sin \theta - z \cos \theta) \right\} \times W(x, y) dx dy dz \quad (2.34)$$

If the backscatter density changes its position without the changes of dielectric properties, the backscatter density at second acquisition can be written as

$$f_2(x, y, z) = f_1(x, y, z) \exp \left[i \frac{4\pi}{\lambda} \{ d_y \sin \theta + d_z \cos \theta \} \right] \quad (2.35)$$

where d_y and d_z are displacement of elements along the y and z axis. The correlation between the signals is

$$\begin{aligned} s_1 s_2^* &= \iiint \iiint f_1(x, y, z) f_1^*(x, y, z) \exp \left\{ -i \frac{4\pi}{\lambda} (d_y \sin \theta + d_z \cos \theta) \right\} \\ &\quad \times W(x, y) W(x, y) dx dy dz dx dy dz \end{aligned} \quad (2.36)$$

If the uniform system response and the independent probability distributions, $p_y(d_y)$ and $p_z(d_z)$, which are the motions displacement along y and z , are assumed, after averaging the equation is simplified as

$$\begin{aligned} \langle s_1 s_2^* \rangle &= \iiint \iiint \rho(x, y, z) \exp \left\{ -i \frac{4\pi}{\lambda} (d_y \sin \theta \right. \\ &\quad \left. + d_z \cos \theta) \right\} p_y(d_y) p_z(d_z) dx dy dz dd_y dd_z \end{aligned} \quad (2.37)$$

The $\rho(x, y, z)$ is the structure function of back scatter density, thus its integration may be written as

$$\iiint \rho(x, y, z) dx dy dz = \sigma^0. \quad (2.38)$$

where σ^0 is averaged backscatter density. If the probability density function is assumed Gaussian distribution, the temporal decorrelation is described as,

$$\gamma_{temporal} = \exp \left\{ -\frac{1}{2} \left(\frac{4\pi}{\lambda} \right)^2 (\sigma_y^2 \sin^2 \theta + \sigma_z^2 \cos^2 \theta) \right\} \quad (2.39)$$

where σ_y and σ_z are standard deviations of displacement at y and z axis. The formulated temporal decorrelation is a function of standard deviation of displacements of elements in y and z directions. If the variation of the motion is same along the all direction, i.e. $\sigma_y^2 = \sigma_z^2 = \sigma_r^2$, the temporal decorrelation is simplified again,

$$\gamma_{temporal} = \exp \left\{ -\frac{1}{2} \left(\frac{4\pi}{\lambda} \right)^2 \sigma_r^2 \right\} \quad (2.40)$$

So, phenomena increasing the standard deviation, which could be interpreted as inhomogeneous movements of elements, could yield loss of coherence. The response of the temporal decorrelation could vary on the sensors, which utilize different wavelength as shown in Fig. 2. 13.

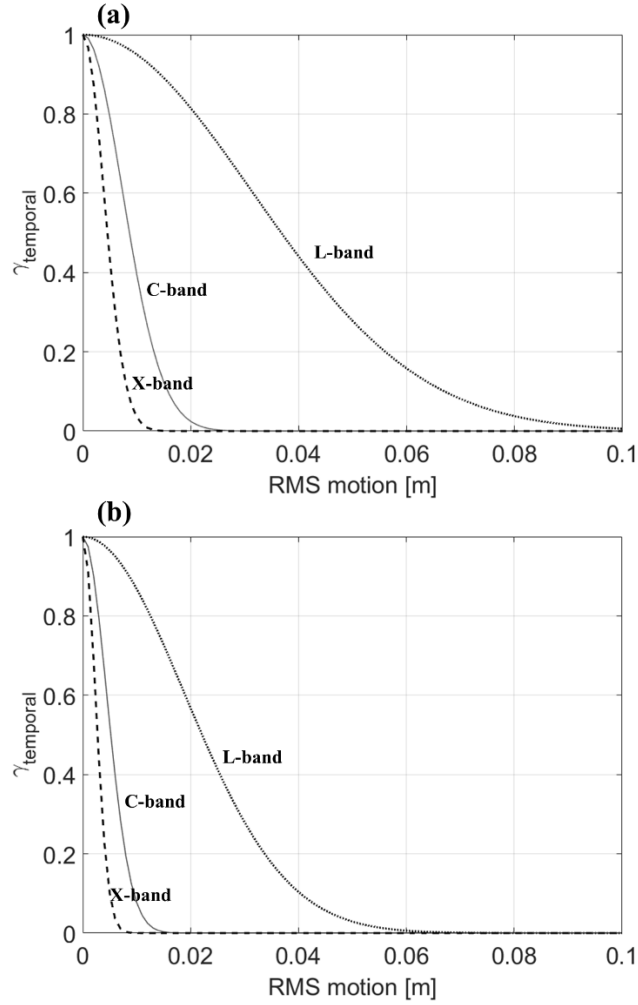


Fig. 2. 13. Theoretical temporal decorrelation induced by motions of scatters for three frequencies. L-band (1.27 GHz, 23.4cm), C-band (5.405 GHz, 5.56 cm), and X-band (10.25 GHz, 2.94cm). (a) When only horizontal motions exist and (b) when horizontal and vertical motions are present.

In the forested area, the temporal decorrelation could be different along the vertical direction. The temporal coherence behavior has been explained in the literature. In this case, the structure function of backscattered signal can be a function of volumetric height.

$$\iiint \rho(x, y, z) dx dy dz = \sigma^0 \int \rho(z) dz \quad (2.41)$$

Here, the distribution of backscatter density is assumed homogeneous along the range and azimuth direction. Also, by setting the $d_z = d_y$ and a new parameter, $d_r = d_y \sin \theta + d_z \cos \theta$, which represents the displacement along the line of sight direction, the correlation between two signals can be expressed as,

$$\langle s_1 s_2^* \rangle = \sigma^0 \iint \rho(z) \exp \left\{ -\frac{4\pi d_r}{\lambda} \right\} p_r(d_r, z) dz dd_r \quad (2.42)$$

After normalizing the temporal decorrelation along the vertical direction is formulated as,

$$\gamma_{temporal} = \frac{\iint \rho(z) \exp \left\{ -\frac{4\pi d_r}{\lambda} \right\} p_r(d_r, z) dz dd_r}{\int \rho(z) dz} \quad (2.43)$$

If the Gaussian distribution is assumed about probability density function $p_r(d_r, z)$, the equation is simplified,

$$\gamma_{temporal} = \frac{\int \rho(z) \exp \left\{ -\left(\frac{4\pi \sigma_r(z)}{\lambda} \right)^2 \right\} dz}{\int \rho(z) dz} \quad (2.44)$$

The temporal decorrelation in a forested area is a function of standard deviations of displacement of elements in the line of sight direction. The formulations of temporal decorrelations assuming forested area differ from the normal case in terms of the vertical structure of the forest. Thus, the temporal decorrelation could vary along the vertical direction of the forest. The expression of temporal decorrelation is described only when acquired SAR data have zero baselines. In the presence of rather long spatial baseline, the volumetric decorrelation also affects the total coherence. The volumetric decorrelation explained in the previous chapter is also the function of

height. Then, the temporal and volumetric decorrelation are combined along the vertical direction and are difficult to be separated. In that case, the more complicated model is required.

In Addition, it is worth noting that the temporal decorrelation describes only phenomena related to the movement of elements. In the real case, the dielectric properties of elements in a resolution cell can be affected and changed by a variety of natural phenomena. For instance, changes in soil moisture can yield the different states of dielectric properties and change the penetration depth, heterogeneously. Also, the loss of coherence versus time interval between image acquisition times has been reported in the literature (Lombardini et al., Jul. 1998; Rocca, 2007). Therefore, the decorrelation induced by motions is appropriate to explain the temporal behavior in the dataset which acquired with short temporal baseline (i.e. a few minutes to hours). However, for the multitemporal dataset which is acquired with rather long temporal baseline (i.e. a few days to months), the temporal decorrelation is not fully understood. Therefore, the formulation of the temporal decorrelation model is required in use of the multi-temporal coherences. For this, the temporal decorrelation model for multitemporal dataset will be explained.

2.3. Derivation of coherence model assuming two layers for repeat-pass interferometry

Temporal decorrelation is associated with changes in the dielectric and structural properties of the scatterers (Lavalle et al., 2015; Zebker & Villasenor, 1992). These changes are more likely to occur over longer interferometric time intervals, which are typical of the space-borne interferometer. Among the various land covers, vegetated areas are more affected by temporal decorrelation owing to the motion of leaves and dielectric changes associated with natural growth and leave falling. All

these effects change the complex reflectivity in the radar resolution cell and cause decorrelation in interferometric radar signals.

Here, a temporal decorrelation model to describe the coherence behavior observed in the repeat pass acquisition strategies with temporal baseline on the order of months or years will be formulated. Temporal decorrelation for the forested area is decomposed into several terms depending on where the temporal decorrelation occurs, i.e., volume or ground, and what induces the temporal decorrelation, i.e., motion or dielectric changes. The multiple targets having different behaviors in a resolution cell effectively determine the coherence. The vegetated area has the distinct and discriminated properties in volume layer and underlying ground layers. Hence, the coherence is rather stable even in the long temporal baseline, meanwhile, the coherence decreases faster in short temporal baseline (Wei & Sandwell, 2010). Motion-induced temporal decorrelation occurs when the scatterers change their positions during the time between the acquisitions of two interferometric images (Zebker & Villasenor, 1992). Leaves and branches are likely to be randomly rearranged by the wind, and their positions are uncorrelated with the initial positions. Thus, the motion in the canopy can occur even within timescales of seconds. The dielectric properties change includes soil-moisture change, and the structure profiles change. They can be observed in rather long timescales of hours or days.

2.3.1. General coherence model involving temporal decorrelation

A widely-used model of the polarimetric-interferometric coherence for vegetation employs a volume layer, which comprises uniformly distributed and randomly oriented scattering elements, and an underlying surface that represents the ground. If the vertical coordinate is denoted by z , the location of the surface is at $z = z_0$ and the location of the top of the volume layer at $z = z_0 + h_v$, where h_v

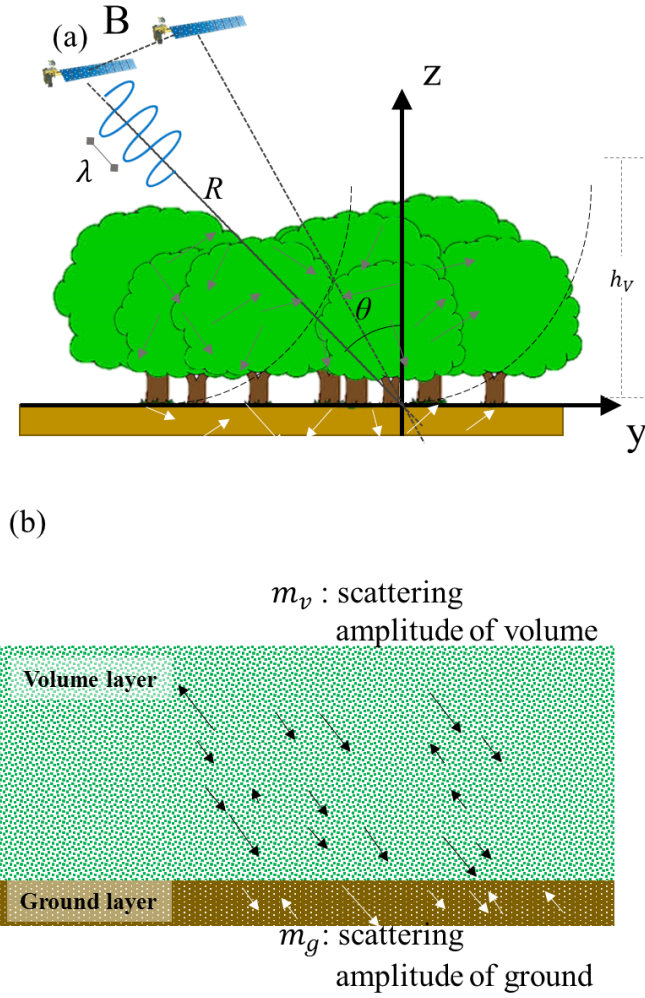


Fig. 2. 14. Schematic representation of random motion over ground model. (a) Actual geometry of sensors and forest with motion, and (b) simplified two layers model with motion.

is the canopy height. In the case of the ground layer, the repeat-pass complex coherence is described by the effective temporal decorrelation of the surface, γ_t^g , and interferometric coherence:

$$\gamma^g = \gamma_t^g e^{ik_z z_0} \quad (2.45)$$

The temporal decorrelation component in the volume layer, $\gamma_t^v(z)$, as:

$$\gamma^v = e^{ik_z z_0} \frac{\int_0^{h_v} \gamma_t^v(z') p(z') e^{ik_z z'} dz'}{\int_0^{h_v} p(z') dz'} \quad (2.46)$$

If the exponential profile is assumed for the attenuation, the structure function can be expressed as a one-way extinction coefficient, σ_e in Eq. (2.47)

$$\begin{aligned} \gamma^v &= e^{ik_z z_0} \frac{m_v \int_0^{h_v} \gamma_t^v(z') e^{\frac{2\sigma_e(z'-h_v)}{\cos\theta}} e^{ik_z z'} dz'}{m_v \int_0^{h_v} e^{\frac{2\sigma_e(z'-h_v)}{\cos\theta}} dz'} \\ &= \frac{e^{ik_z z_0} m_v}{m_{0v}} \int_0^{h_v} \gamma_t^v(z') e^{\frac{2\sigma_e(z'-h_v)}{\cos\theta}} e^{ik_z z'} dz' \quad (2.47) \end{aligned}$$

$$\text{where, } m_{0v}(w) = \left(\frac{\cos\theta_0}{2\sigma_e} \left(1 - e^{-\frac{2\sigma_e h_v}{\cos\theta}} \right) \right) m_v(w)$$

Here, w represents the polarimetric scattering mechanism. Eqs. (1) and (6) can be combined for a typical forest area if the radar signal penetrates the canopy of forest and interaction between ground and canopy is sufficiently strong. Thus, the final two-layer coherence model containing the volumetric and temporal decorrelations can be expressed as follows:

$$\gamma(w) = e^{ik_z z_0} \frac{m_{0v}(w) \gamma^v e^{-ik_z z_0} + p_g m_g(w) \gamma_t^g}{m_{0v}(w) + p_g m_g(w)} = e^{ik_z z_0} \frac{\gamma^v e^{-ik_z z_0} + \mu(w) \gamma_t^g}{1 + \mu(w)} \quad (2.48)$$

$$\text{where, } p_g = e^{-2\sigma_e h_v / \cos\theta}, \quad (2.49)$$

$$\text{and } \mu(w) = \frac{p_g m_g(w)}{m_{0v}(w)} = \frac{2\sigma_e e^{-\frac{2\sigma_e h_v}{\cos\theta}} m_g(w)}{\cos\theta_0 (1 - e^{-2\sigma_e h_v / \cos\theta}) m_v(w)}. \quad (2.50)$$

Based on the two-layer coherence model, many modifications have been applied to extract the physical parameters of forest depending on the strategies of data

acquisitions. If the temporal baseline is sufficiently short, such that temporal decorrelation is negligible as in the case of single-pass interferometry, the model will be coincident with the RVoG used to estimate canopy height and other physical parameters. For the case in which the volume temporal decorrelation is a function of canopy height and motions of scatterers, the form of the model will be reformulated to RMoG (Lavalley & Hensley, 2015; Lavalley et al., 2012). For a scenario with a long temporal baseline (i.e., a few months to years) and a near-zero spatial baseline (the UAVSAR repeat tracks remain within a 5-m tube), different assumptions for the temporal decorrelation can be applied.

2.3.2. Coherence model for zero-spatial baseline and long temporal baseline

For polarimetric interferometric pairs with zero spatial baselines ($k_z = 0$), the volumetric decorrelation component in Eq. (2. 47) vanishes and Eq. (2. 47) becomes (Lavalley & Hensley, 2015; Lavalley et al., 2012).

$$\gamma(w) = \frac{\frac{m_v}{m_{0v}} \int_0^{h_v} \gamma_t^v(z') e^{\frac{2\sigma_e(z'-h_v)}{\cos\theta}} dz' + \mu(w) \gamma_t^g}{1 + \mu(w)} \quad (2.51)$$

In Eq. (2. 51), the temporal decorrelation of the volume layer $\gamma_t^v(z')$ is indicated as a height-dependent parameter to highlight a general relationship between canopy height and motions of scatterer (Lavalley & Hensley, 2015; Lavalley et al., 2012). This relationship can be simplified by using the mean-value theorem (Jung et al., 2016). According to the mean-value theorem, given two continuous functions, $f(x)$ and $g(x)$, within interval (a, b), the definite integral of $\int_a^b f(x)g(x)dx$ can be rewritten as $f(c) \int_a^b g(x)dx$, where mean value “c” is defined on [a, b]. Thus, Eq. (2.51) can be rewritten as (Jung et al., 2016)

$$\gamma(w) = \frac{\frac{m_v}{m_{0v}} \gamma_t^v(h_{v0}) \int_0^{h_v} e^{\frac{2\sigma_e(z'-h_v)}{\cos\theta}} dz' + \mu(w) \gamma_t^g}{1 + \mu(w)} = \frac{\gamma_t^v + \mu(w) \gamma_t^g}{1 + \mu(w)} \quad (2.52)$$

where h_{v0} is an arbitrary intermediate height in the interval $[0, h_v]$. Note that the modification from Eq. (2.48) to Eq. (2.52) reduces the number of variables. This algebraic manipulation implies that the phase of the complex coherence for the long-temporal repeat-pass interferometric pairs is related to the displacement of the surface, and the atmospheric phase delay rather than the topographic phase. Also, the complex value can be induced by the soil moisture change (De Zan et al., 2014; Nolan & Fatland, 2003; Nolan, Fatland, et al., 2003; Zwieback et al., 2015). Meanwhile, the amplitude of the observed coherence can be explained mainly by the temporal decorrelation and ground-to-volume ratio without volumetric decorrelation. Thus, the Eq. (2.52) would be useful for exploiting the temporal decorrelation because the volumetric decorrelation and associated physical parameters do not need to be taken into consideration.

For the long temporal baseline, not only wind-induced motion but also dielectric changes including soil moisture changes can occur. Modeling dielectric changes in the forested area is a challenging task. In order to keep the model with a small number of unknowns while capturing the sensitivity of the coherence over long temporal intervals, the temporal decorrelation parameter γ_t^g is assumed to be dominated by soil moisture induced dielectric changes whereas the temporal decorrelation parameter γ_t^v is assumed to be mainly driven by wind. The rationale behind this choice is that soil tends to remain wet for several hours (or days) after precipitations, in contrast to canopy elements that tend to dry out faster and be more subject to positional changes. Under this assumption, γ_t^g is complex-valued and has dependency on the polarization, meanwhile γ_t^v is real-valued and polarization-independent parameter (Hajnsek et al., 2009). One of the coherence behaviors observed in a repeat-pass interferometry scenario with long temporal

baselines is that the amplitude of coherence decreases as the time-span of interferometric pair increases. This coherence behavior is observed clearly in data sets acquired by repeat-pass space-borne SAR systems. The phenomenon is explained by the Brownian motion, hence, non-consistent scattering conditions after meteorological events such as rain, snow, and wind. This model is a function of the temporal baseline and has been adopted to quantify the coherence behavior (Lombardini et al., 1998; Rocca, 2007). Indeed, the measured coherences cannot be explained by only exponentially decayed model, because the scattering condition often changes regardless of time intervals. Consequently, it is necessary to formulate the temporal decorrelation using two terms: the temporally correlated changes, γ_{t_corr} , and temporally uncorrelated (random) changes, γ_{t_rand} , for volume or ground layers:

$$\gamma_t^g = \gamma_{t_corr}^g \gamma_{t_rand}^g = \exp\left[-\frac{\Delta T}{\tau_g}\right] |\gamma_{t_rand}^g| \exp(i\phi_{\gamma_t^g}) \quad (2.53)$$

$$\gamma_t^v = \gamma_{t_corr}^v \gamma_{t_rand}^v = \exp\left[-\frac{\Delta T}{\tau_v}\right] |\gamma_{t_rand}^v| \quad (2.54)$$

Decomposition of the temporal decorrelation implies that observed coherence of every pixel has its unique time-characteristic constants, τ_v or τ_g , to define the exponentially decayed line, and that the differences between the line and the observed coherence can be interpreted as the temporally uncorrelated changes, γ_{t_rand} . Further, the temporally uncorrelated changes γ_{t_rand} explain the randomly generated decorrelation such as rain, snow, strong wind and the collapse of manmade structures. Decorrelation caused by sudden events have been reported in the literature, and these phenomena were often observed in coherence maps (A Bouaraba et al., 2012; G. Nico et al., 2000). The different coherence values are usually observed even though the temporal baselines of interferometric pairs are same over the same scatterers. According to the proposed model, these coherent differences are interpreted as an effect of the temporally uncorrelated dielectric change.

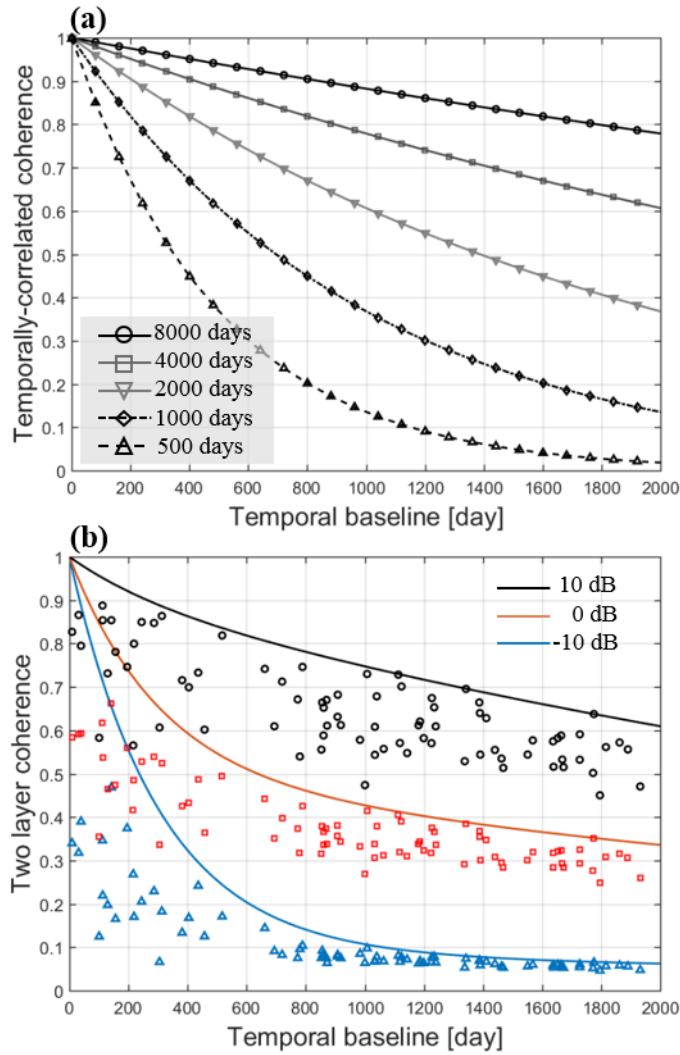


Fig. 2. 15. (a) Temporally correlated coherence behavior versus temporal baseline when the characteristic time constants are 8000, 4000, 2000, 1000, and 500 days. (b) Coherence modeled in two layers when characteristic time constants of the ground and volume are 5000 and 300 days and the ground-to-volume ratios are 10, 0, and 10 dB. The lines represent the hypothetical envelopes defined by the temporally correlated coherence. The points are the coherences of two-layer model for three different ground-to-volume ratios assuming Gaussian distributions with 0.85 and 0.4 means and 0.1 and 0.2 standard deviations for ground and volume layers, respectively.

The temporally uncorrelated term $\gamma_{d,rand}$ can be divided into $\gamma_{d,rand}^g$ and $\gamma_{d,rand}^v$ depending on where decorrelation happens. Consequently, the final form used to model temporal decorrelation for zero-spatial baseline and long temporal baseline case can be formulated as:

$$\gamma(w) = \frac{\exp\left[-\frac{\Delta T}{\tau_v}\right] |\gamma_{t,rand}^v| + \mu(w) \exp\left[-\frac{\Delta T}{\tau_g}\right] |\gamma_{t,rand}^g| \exp(i\phi_{\gamma_t^g})}{1 + \mu(w)} \quad (2.55)$$

The coherence model, which is a function of wave polarization, indicates that the observed coherence is different depending on the scattering position determined by the radar cross section of wave polarization. Thus, the estimated coherence could vary depending on the physical properties of forest and surface types even though pixels have the same amount of temporal decorrelation in ground and volume layers. Also, the formulated model can explain the coherence behavior in a timescale of months to years due to the existence of the temporally correlated coherence. If the interferometric data is acquired within a timescale of seconds to minutes (i.e. $\Delta T \approx 0$), the contribution of temporally correlated change is almost negligible and temporal decorrelation can be interpreted as the result of motion of scatterers. Therefore, the form of the model becomes the RMoG model with zero spatial baseline, potentially enabling retrieval of the motion standard-deviation (Lavalle & Hensley, 2015; Lavalle et al., 2012). However, in Eq. (2. 55), the direct conversion from temporal decorrelation to the standard-deviation of motions is ambiguous because the dielectric changes should be considered in long-temporal repeat-pass scenario.

The temporally correlated change terms, $\gamma_{t,corr}^{g, v}$, are defined as functions of the characteristic time constants, τ_g and τ_v . These variables represent how sensitively the scatterers in a resolution cell respond to the natural changes. In Fig. 2. 51(a), the envelopes of the temporally correlated changes are plotted versus the temporal baseline for characteristic time constants of 8000, 4000, 2000, 1000, and 500 days.

A high value indicates that the dynamic and dielectric properties of scatterers are unlikely to change with time, and consequently, the coherence slowly drops toward zero as shown in Fig. 2. 51(a). Fig. 2. 51(b) shows the simulated coherences versus the temporal baseline for distinct values of ground to volume ratio. In this figure, the characteristic time constants of the ground and volume are 5000 and 300 days for three candidates of ground-to-volume ratios, -10, 0, and 10 dB. The temporally uncorrelated (random) coherences of the ground or volume, $\gamma_{t_rand}^{v, g}$, are given as real value so that they have Gaussian distributions with 0.85 and 0.4 means and 0.1 and 0.2 standard deviations, respectively. According to the formulated coherence model Eq. (2. 55), the different observed magnitudes of coherence can be attributed to the ground-to-volume ratio at arbitrary polarization, even though the physical parameters such as characteristic time constants and temporally-uncorrelated coherence are the same. Because of this sensitivity of coherence to the ground-to-volume ratio corresponding the certain polarization, this study can better constrain the model parameters by introducing additional polarization in the inversion process.

2.3.3. Comparison of coherence model for zero-baseline and long temporal baseline with RVoG and RMoG

The coherence model proposed in the previous section is for the long-temporal baseline and zero-spatial baseline. The recently developed coherence models such as RVoG, RVoG+VTD, and RMoG model were designed for different purposes, under the several assumptions. In this section, the models will be compared regarding the assumptions they used and the circumstances they can be applied, and resulting behaviors in coherence.

As summarized in Table 2.1, the RVoG, RMoG, and RVoG+VTD models were designed for the forest parameter extraction, in particular, the canopy height estimation. Thus, the spatial baseline should be longer than zero. However, the model

Table. 2. 1. Model comparison

	RVoG	RMoG	RVoG+VTD	This study
Purpose	Forest parameter extraction	Forest parameter extraction	Forest parameter extraction	Change or Damage detection
Spatial baseline	Non-zero	Non-zero or zero	Non zero	Zero or Near zero
Temporal baseline	Almost zero (a few seconds or minutes)	a few seconds~ a few days	a few seconds~ a few days	a few seconds~ a few months
Decorrelation in volume	Volume decorrelation	Volume decorrelation + temporal decorrelation	Volume decorrelation + temporal decorrelation	temporal decorrelation
Temporal decorrelation source in ground	-	Motion	-	Dielectric change

proposed in this study is for damage assessment, thus there are no reasons for a spatial baseline to be a non-zero value. In contrast, the zero-spatial baseline is more beneficial by minimizing the irrelevant decorrelation sources.

Since the RVoG model considers the volumetric decorrelation only, the temporal baseline should be small enough to be negligible. The terms compensating the temporal decorrelation have been later added in RVoG+VTD model and RMoG model. The temporal decorrelation source there model mainly consider is the dominant positional changes. Accordingly, the choice of available data should be careful unless it has significant dielectric changes. In general, the interferometric pair with the short temporal baseline is related to the motion-induced decorrelation, thus, the RMoG and RVoG+VTD could be suitable for the repeat pass scenario with short temporal baseline. The proposed model has terms describing the temporally correlated and uncorrelated change which can be found in the long temporal baseline.

In Fig. 2. 16, the coherence changes are plotted as a function of the ground-to-volume ratio for comparison of cases with zero and nonzero spatial baselines. For

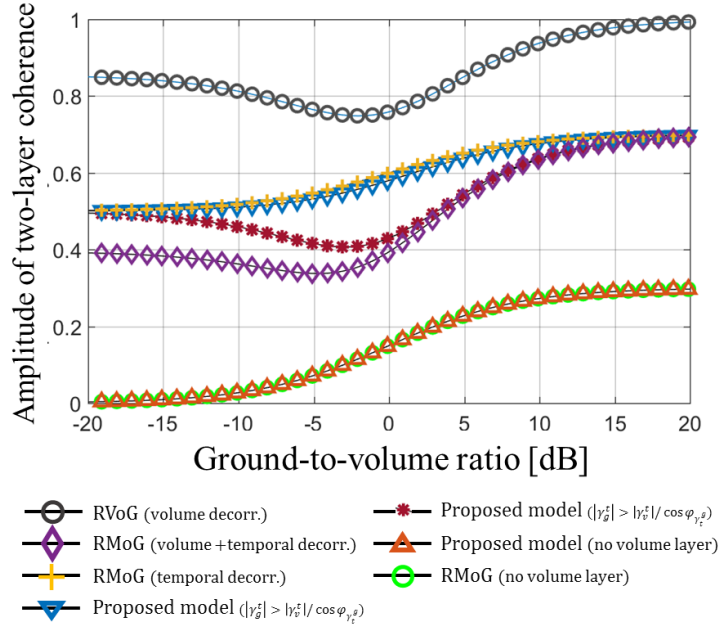


Fig. 2. 16. Coherence behavior calculated from the RVoG model, RMoG model and the coherence model used in this study by varying the ground-to-volume ratios. The coherence involving the volumetric coherence might be non-monotonic, while the coherence changes monotonically when the volumetric coherence is zero in RMoG model. The coherence in the proposed model is monotonic only in the certain condition (i.e. $|\gamma_g^t| > |\gamma_v^t| / \cos \varphi_{\gamma_t^g}$). In the case of no volume layer, then the coherences of two-layer model is governed by only temporal decorrelation of ground regardless of the volumetric decorrelation (red triangles and green circles.).

the coherence with volumetric decorrelation (nonzero spatial baseline), the parameters commonly used are $\theta = 35^\circ$, $k_z = 0.1 \text{ m}^{-1}$, $\sigma_e = 0.12 \text{ dBm}^{-1}$, and $h_v = 25 \text{ m}$. Also, γ_t^g and γ_t^v can be set so that the temporal coherence of the ground layer is higher than the volume layer $|\gamma_t^g| > |\gamma_t^v|$. As the ground-to-volume ratio increases, the coherence with nonzero spatial baseline shows a minimum value for a mixed contribution of the canopy and ground (gray circles and purple diamonds). This indicates the minimum of observed coherences is neither ground layer nor volume layer. The coherence in RMoG model with a zero spatial baseline changes monotonically (yellow plus). Then, without loss of generality, we can

consider the minimum amplitude of coherence as volume dominant layer (low ground-to-volume ratio) and the maximum as the ground-dominant layer (high ground-to-volume ratio). The proposed model in Eq. (2. 55) has a different behavior depending on the amplitude conditions of temporal decorrelation function of ground and volume layers. Hence, if the condition, $|\gamma_g^t| > |\gamma_v^t|/\cos \varphi_{\gamma_t^g}$, is satisfied, the amplitude of complex coherence increase monotonically increase (upside-down triangles). However, the other case, the minimum moves non-monotonically (red asterisks). Thus, the phase induced by dielectric change, $\varphi_{\gamma_t^g}$, can affect the coherence behavior associated with ground-to-volume ratio. In other words, when the phase induced by the dielectric change is not large, the similar interpretation concept can be applied as the RMoG model with a zero-spatial baseline. In order to make the estimation problem tractable, in this study it is assumed that the temporal decorrelation of the ground is moderate. This assumption entails that the amplitude of the complex coherence changes monotonically, which is important in the model parameter inversion because the observed coherences at different polarization can be simply linked to the ground-dominant and volume-dominant layers. Note that when this assumption does not hold for a particular pair, temporal decorrelation is expected anyway to be severe and the overall coherence very low, which suggests that the pair can be disregarded from the set of available pairs and the proposed algorithm can still be applied.

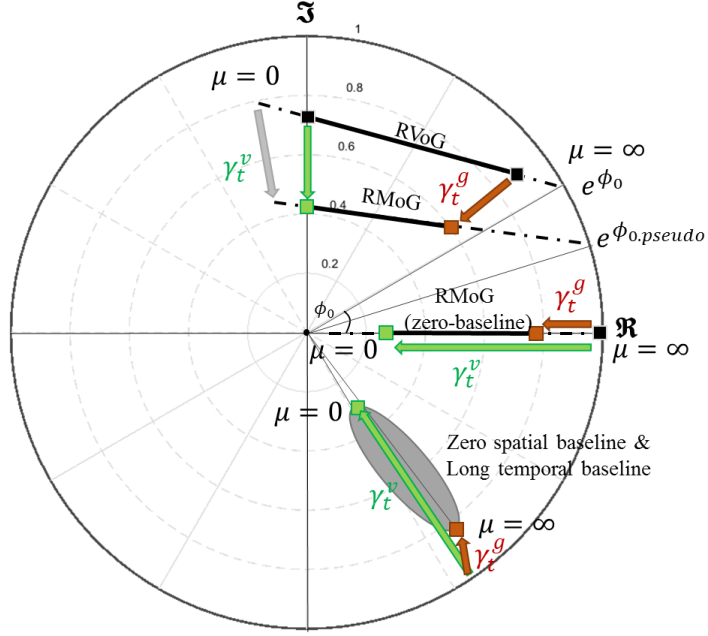


Fig. 2. 17. Coherence loci in a complex plane. The RVoG model and the RMoG model that incorporates the volumetric decorrelation are illustrated. Meanwhile, the RMoG for a zero spatial baseline is observed in the line intersecting the origin. For the long-temporal and zero-spatial baseline case, the line between $\mu = 0$ and $\mu = \infty$ does not need to pass through the origin.

The coherence loci derived from coherence models are illustrated in a complex plane in Fig. 2.17. The ends of the solid line segments represent theoretical points at which the ground-to-volume ratio is infinite or zero. For the RVoG (volumetric coherence only) model, since the ground-to-volume ratio is the only wave-polarization dependent parameter, the coherence is located along the line as the polarization changes. The magnitude and phase of the complex coherence are determined by the physical parameters of forest and the radar parameters. In the RMoG model (volumetric + temporal coherence), the temporal decorrelation shifts the RVoG model line to another line. Not only the physical parameter of vegetated terrain and radar parameters but also the dynamic processes of scatterers relate to the length and angle of the line (Lavalle & Hensley, 2015). Without the consideration of the temporal decorrelation, the topographic height is misinterpreted as $\phi_{0,pseudo}$ not

ϕ_0 . Accordingly, the angle between ϕ_0 and the complex correlation value at $\mu = 0$ is changed and the estimation strategy of volumetric height yields the ambiguous height (S. K. Lee et al., 2013; K. P. Papathanassiou et al., 2003).

Meanwhile, if the case of zero baselines is considered for the RMoG model (no volume decorrelation), the coherence locus is located along the line passing through the origin by varying the ground-to-volume ratio. The phase angle of the line segment is not taken into consideration anymore for the zero spatial baseline and small temporal baseline because temporal decorrelation induced by the motion is mainly observed (Lavalle et al., 2012).

For the scenario of repeat-pass interferometric and zero spatial baseline, the phase is related to the deformation, atmospheric phase delay (APD) and dielectric properties change (i.e. soil moisture change). The phase induced by deformation, and APD is normally polarization-independent. In Eq. (2. 55), if $\varphi_{\gamma_t^g}$ is non-zero, the coherence locus does not pass through the origin. Also, if the $\gamma_{t_rand}^g$ is assumed to be polarization independent, the complex coherence vary along a line depending on the ground-to-volume ratio. However, if the polarization dependency is enough strong, the coherences are located in a certain region as polarization changes (Flynn et al., 2002).

By analyzing the distribution of the complex coherences in the complex plane, the strategy of coherence optimization can be designed. Depending on the amount of the volumetric coherence, the angles of the ends of the line is widened. Since the line defined by the volumetric coherence does not need to intersect the origin, the distance between the ends is important. Accordingly, the coherence optimization method to estimate the maxima of the distance between ends is appropriate. Meanwhile, if the volumetric decorrelation is negligible and the temporal decorrelation is dominant, the maxima and minima of magnitude of complex coherence have a close relationship to the model. Therefore, the coherence

optimization algorithm to find the magnitude maximum in the distribution need to be introduced. The coherence optimization algorithm is discussed more in Chapter 4.

Chapter 3.

Damage mapping using temporal decorrelation model for single-polarized SAR data

: A case study for volcanic ash

Change detection technique is one of the main applications in the remote sensing area. In particular, coherent change detection (CCD) utilizing coherence of interferometric pair is a unique approach achievable only in SAR data. As explained in Chapter 2, since the coherence, the main material of CCD, is determined by diverse sources, the temporal decorrelation model essentially needs to be applied for the interpretation.

Currently operating space-borne SAR system has collected interferometry-capable and multi-temporal SAR images. A number of single-polarized images have been accumulated for past decades over the whole area of Earth. Therefore, the method for multi-temporal interferometric data which are usually acquired at single-polarized data should be primarily designed.

In this Chapter, the CCD technique using the temporal decorrelation model will be applied for detection of volcanic ash of Kirishima volcano in 2011 as a case study. Also, the interpretation of the temporal decorrelation model is performed using Japan Aerospace Exploration Agency's (JAXA's) ALOS-PALSAR which acquired for single-polarized interferometric data.

3.1. Description of study area

Kirishima volcano, located in Kyushu, Japan, is a volcanic cluster consisting of more than 10 basaltic-andesite volcanoes which were active during the 22,000 years.

Shinmoedake is a stratovolcano, one of the volcanoes of Kirishima volcano cluster, and the several small and big eruptions have been reported. The phreatic eruptions were observed in 2008 and 2010 and the magmatic eruptions started in January 2011. After a small phreatomagmatic event on January 19, 2011, a sub-plinian event started on January, 26. During the eruptions, effusion of lava inside the summit crater was observed and a strong shock wave and an explosion earthquake are recorded by tiltmeters and GPS. A thick layer of volcanic ash was deposited on the southeastern part of the volcano (Miyabuchi et al., 2013).

According to the land-use map (ver. 2014.04) provided by JAXA (Takahashi et al., 2013), the peak and the area around the rim of the Shinmoedake volcano mainly consist of bare soil. The Kirishima volcano cluster is surrounded by evergreen and deciduous forest as shown in Fig. 3.2. Thus, the volcanic ash emitted in 2011 mainly fell on bare soil and vegetated areas. As stated in Chapter 2, the decorrelation caused by the volcanic eruption event may appear on top of the temporal decorrelation caused by the natural background change. Such temporal decorrelation caused by the natural change may be misinterpreted as the contribution of the major event. In particular, this misinterpretation might be severe in forests because vegetated areas are prone to temporal decorrelation. Therefore, understanding and predicting the coherence behavior using a temporal decorrelation model are essential for accurate interpretation of coherence.

Kirishima city was chosen for comparison of change detection results in order to evaluate the performance of the change detection method. This area is not severely affected by the volcanic ash in 2011. The city is a type of suburban which consists of man-made structures, cropland, and bare soil.

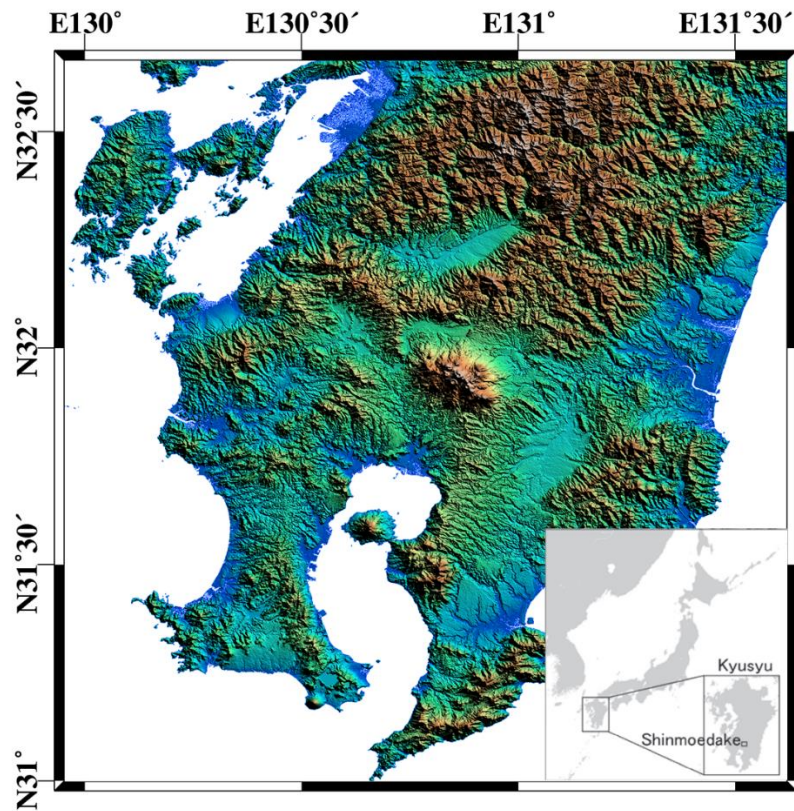


Fig. 3. 1. Topographic map of Kyushu, Japan (Top), and shade relief map of Kirishima volcano cluster (Bottom).

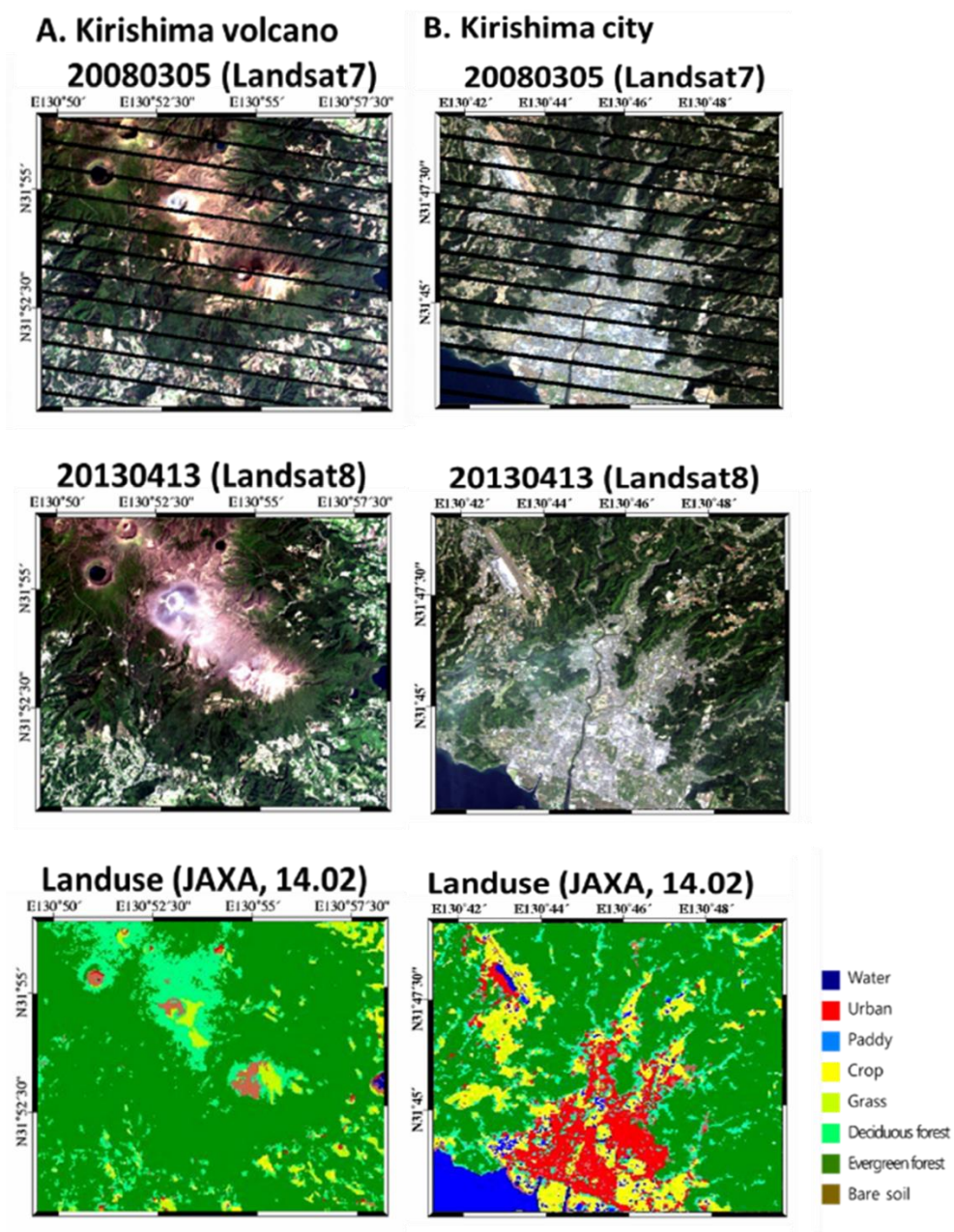


Fig. 3. 2. Landsat images acquired March 5, 2008, and April 13, 2013. Land-use maps provided by JAXA for Kirishima volcano and Kirishima city.

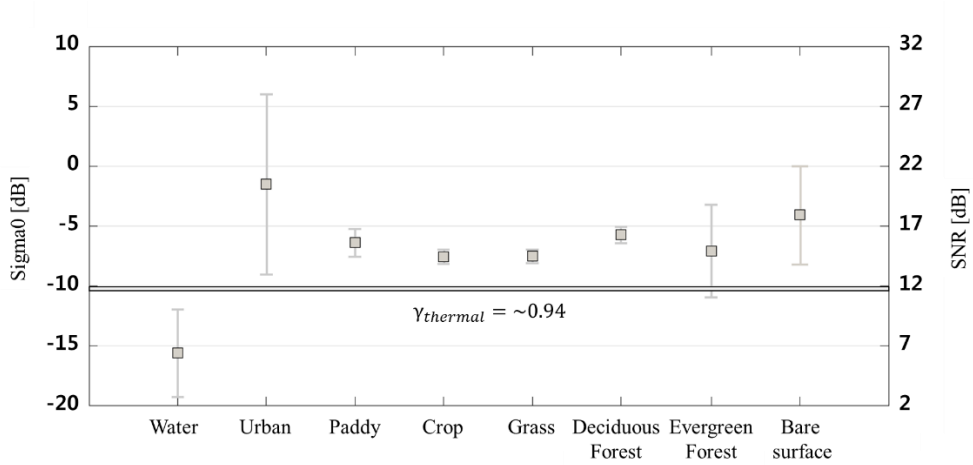


Fig. 3. 3. Sigma 0 and SNR distributions for diverse land uses.

3.2. Data description

In this study, 21 ALOS-PALSAR datasets were used with HH polarization of the study area acquired from January 2007 to April 2011 (about 4.2 years) in descending orbit at a 38° incidence angle. The interferometric pairs were separated into pre-eruption and co-eruption pairs. Only two images were acquired after the volcanic eruption in January 2011 (March 05, 2011 and April 20, 2011). The coherence maps generated using pre-eruption data was assigned as the reference pairs, and these coherence maps were used to interpret the temporal behaviors of natural phenomena via a temporal decorrelation model. The coherence maps generated using co-eruption data were assigned to the event pairs. Interferometric coherence estimation was performed after 32 multi-looking, common band filtering, and removal of flat-earth and the topographic phase. Thus, the bias of coherence and geometrical decorrelation were assumed insignificant. The SNRs were estimated by dividing sigma zero (σ^0) by NESZ(Sun et al., 2010). The minimum NESZ was approximately -23 dB in HH polarization of FBS and FBD modes(Shimada et al., 2009). The acquired data set showed a high SNR for the forest and urban areas, specifically, > 12 , and a low SNR

in the sea area, specifically < 8 as shown in Fig. 3.3. The thermal decorrelation of the forest and urban areas was less than 0.07; thus, thermal noise may not have been the cause of the major decorrelation in those areas. However, the areas with a low SNR, such as the sea and rivers, are prone to thermal decorrelation. Therefore, areas consisting of the sea were masked out and the analysis was mainly performed on bare soil, urban area, and forest, which have high SNR.

For minimization of the volumetric decorrelation, the interferometric pairs within 1000m were chosen as listed in Table 3.1. As described in Chapter 2, the volumetric decorrelation may be over 0.94 for interferometric pairs within 1000m in the case of ALOS PALSAR. Thus, the volumetric decorrelation is assumed not to be major contributions of the decorrelations.

Under criteria described, the coherence maps can be assumed to be affected by only the temporal decorrelation. Generated coherence maps were visualized in Fig 3.4-6. The overall coherences tend to decrease as the temporal baseline is longer. Its behavior will be explained in next sections. The coherence maps shown in Fig. 3.6 have information of volcanic ash because these are generated from event pairs. The signature of volcanic ash is observed, but not clearly. In event pair with 46 temporal baselines, the low coherence value is observed around Shinmoedake volcano. Even though the volcanic ash was mainly deposited over the southeastern slope of the volcano, the low coherence is also observed in northwestern slope. Another misinterpretation could result in the coherence map with 1012 temporal baseline. Since the overall area over the whole scene shows low coherences, the separation between the natural changes and event is difficult. In next section, the algorithm will be discussed for the accurate interpretation, and change detection using temporal decorrelation model.

Table 3. 1. Interferometric pairs used in this study

Master (yyyymmdd)	Slave (yyyymmdd)	Temporal baseline [day]	Spatial baseline [m]	Master (yyyymmdd)	Slave (yyyymmdd)	Temporal baseline [day]	Spatial baseline [m]
Reference Pair							
20070107	20071125	322	18	20080712	20090830	414	-763
20070107	20080110	368	353	20080712	20091015	460	-77
20070107	20080225	414	945	20080712	20091130	506	226
20070107	20100115	1104	-628	20080712	20100115	552	782
20070107	20100302	1150	-154	20081012	20081127	46	191
20071125	20080110	46	334	20081012	20090112	92	532
20071125	20080225	92	927	20081127	20090112	46	341
20071125	20100115	782	-647	20090112	20090414	92	872
20071125	20100302	828	-173	20090112	20090830	230	925
20080110	20080225	46	592	20090414	20090530	46	812
20080110	20100115	736	-981	20090414	20090830	138	53
20080110	20100302	782	-508	20090414	20091015	184	739
20080225	20080411	46	329	20090530	20090830	92	-758
20080225	20080527	92	769	20090530	20091015	138	-73
20080225	20101203	1012	565	20090530	20091130	184	230
20080225	20110118	1058	903	20090530	20100115	230	786
20080411	20080527	46	440	20090830	20091015	46	685
20080411	20101203	966	236	20090830	20091130	92	989
20080411	20110118	1012	573	20091015	20091130	46	303
20080527	20101203	920	-203	20091015	20100115	92	860
20080527	20110118	966	133	20091130	20100115	46	556
20080712	20090414	276	-816	20100115	20100302	46	473
20080712	20090530	322	-4	20101203	20110118	46	337
Event pair							
20080527	20110305	1012	582	20110118	20110305	46	449
20101203	20110305	92	786				

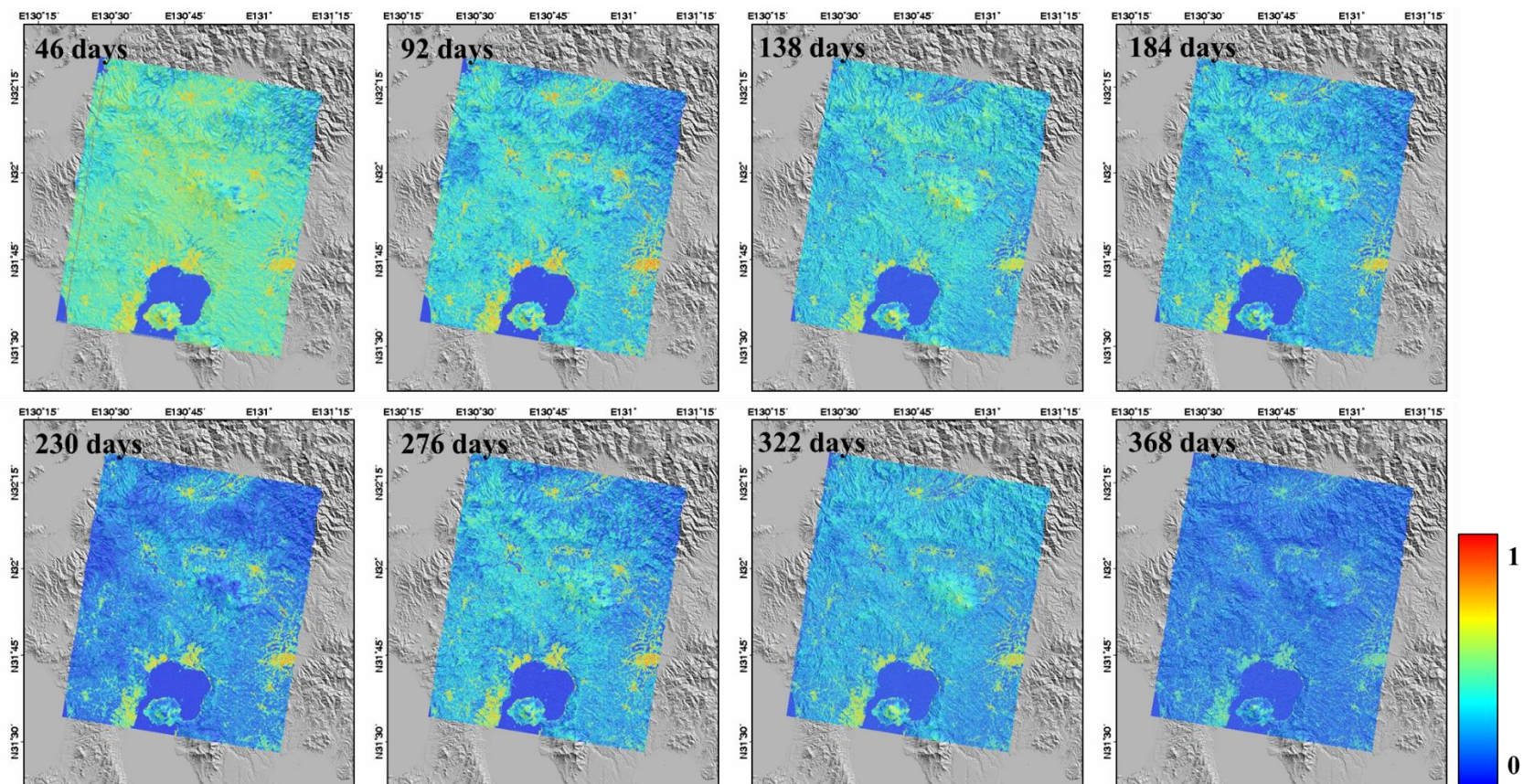


Fig. 3. 4. Averaged coherence maps of reference pairs with time intervals from 46 days to 368 days. The interferometric pairs are listed in Table 3.1.

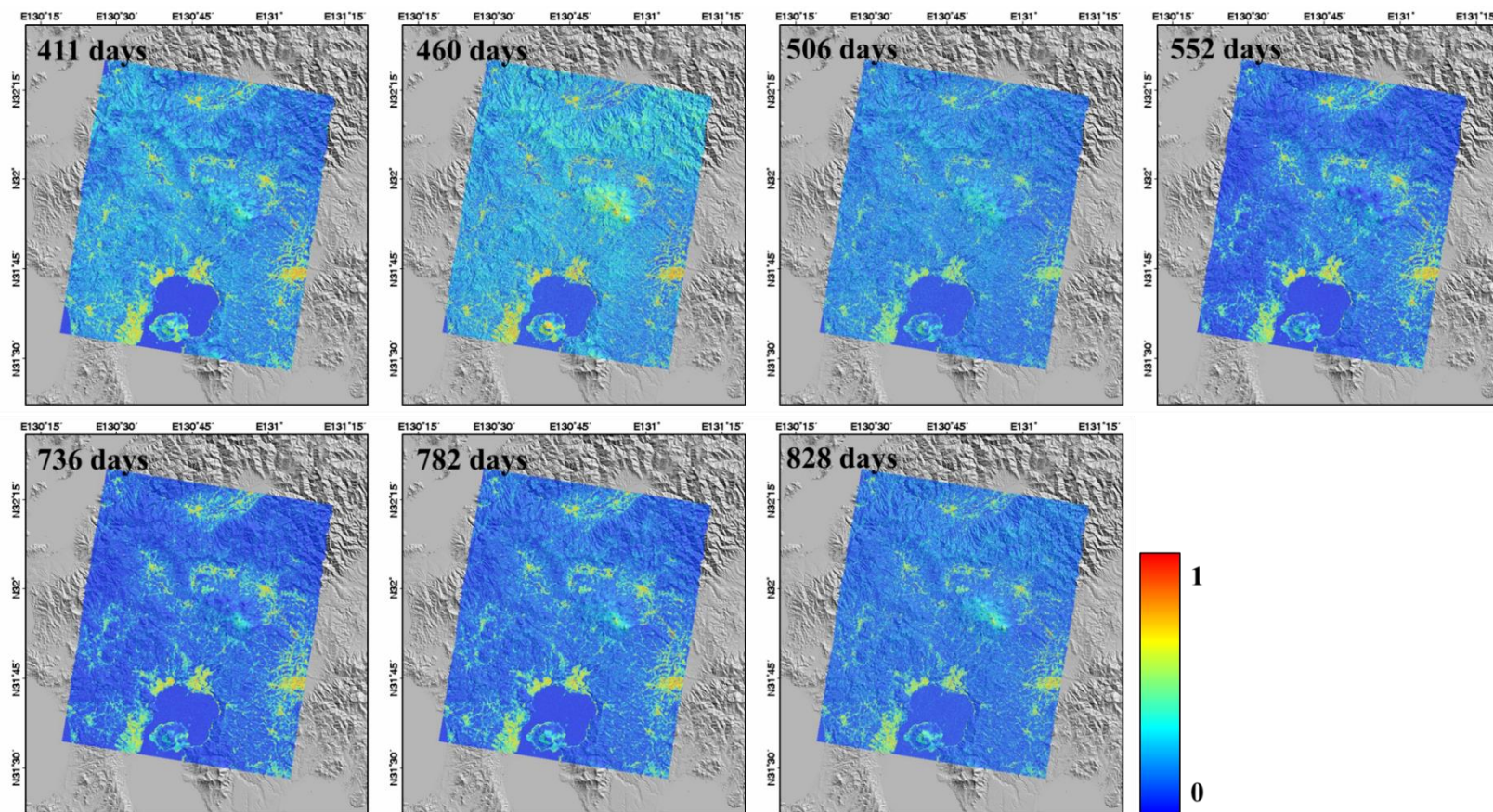


Fig. 3. 5. Averaged coherence maps of reference pairs with time interval from 411 days to 828 days. The interferometric pairs are listed in Table 3.1.

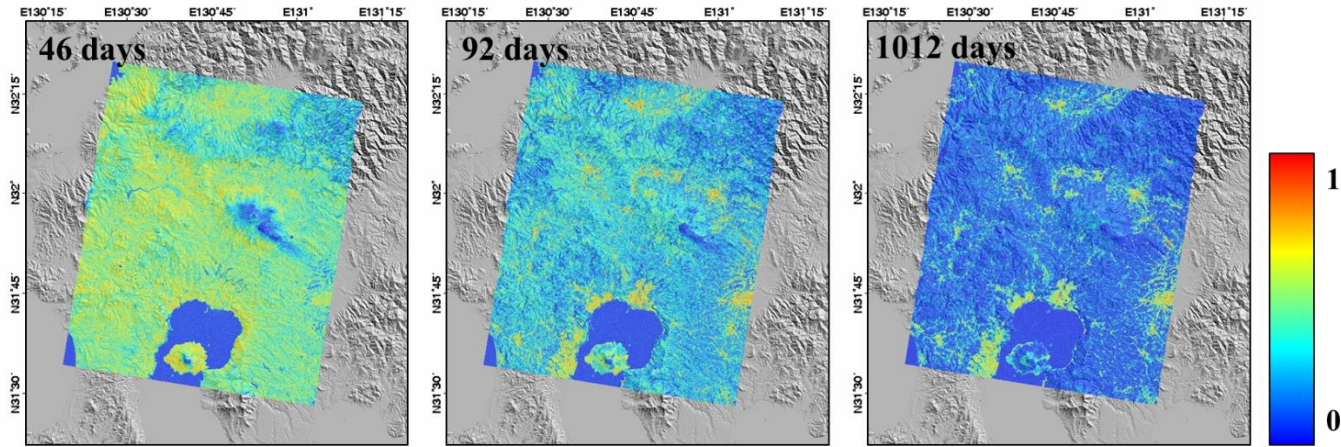


Fig. 3. 6. Coherence maps of event pairs. Jan.18.2011 - Mar.05.2011 (left), Dec.03 – Mar. 05.2011(Middle), and Aug. 27.2008 – Mar.05.2011. (Right)

3.3. Extraction of temporal decorrelation parameters

If N interferometric pairs (sum of the number of reference and event pairs) are available, the number of model parameters become $2N + 3$ in multi-temporal and single-polarization interferometer, because $\gamma_{t_rand}^v$ (N) and $\gamma_{t_rand}^g$ (N) are pair-variant variables and μ , τ_g , and τ_v are pair-invariant variables. Consequently, extracting the model parameters is a challenging task. Despite the analytic limitation, it is possible to estimate the model parameters of the proposed temporal decorrelation model under several realistic assumptions as described hereafter.

In the first step, the highest coherence values were identified in each time interval in the reference pairs. An exponential curve envelope can be fitted for the highest coherence values. The highest coherence values indicate that the coherence is most likely unaffected by temporally uncorrelated temporal decorrelation, which means that $\gamma_{t_rand}^v$ and $\gamma_{t_rand}^g$ are almost equal to one. This assumption is beneficial to simplification of the temporal decorrelation model to,

$$\gamma_t^{high} = \frac{1}{1 + \mu} \exp\left(-\frac{\Delta T}{\tau_v}\right) + \frac{\mu}{1 + \mu} \exp\left(-\frac{\Delta T}{\tau_g}\right) \quad (3.1)$$

The second step is to estimate the ground-to-volume ratio μ and the characteristic time on the ground, τ_g , and in the volume, τ_v . This procedure was performed using curve fitting to the highest points. The curve fitting was applied so that the fitted curve was closest and higher than the selected highest coherences, as shown in Fig. 3.7. In addition, the model parameters, τ_v , τ_g , and μ , all should be greater than zero so that they reflect realistic conditions. The highest points are used for curve fitting because any changes in their structural and dielectric properties would result only in decorrelation. Further, corresponding model parameters, $\gamma_{t_rand}^v$ and $\gamma_{t_rand}^g$, are constrained in the range zero to one. If the coherence points are located over the

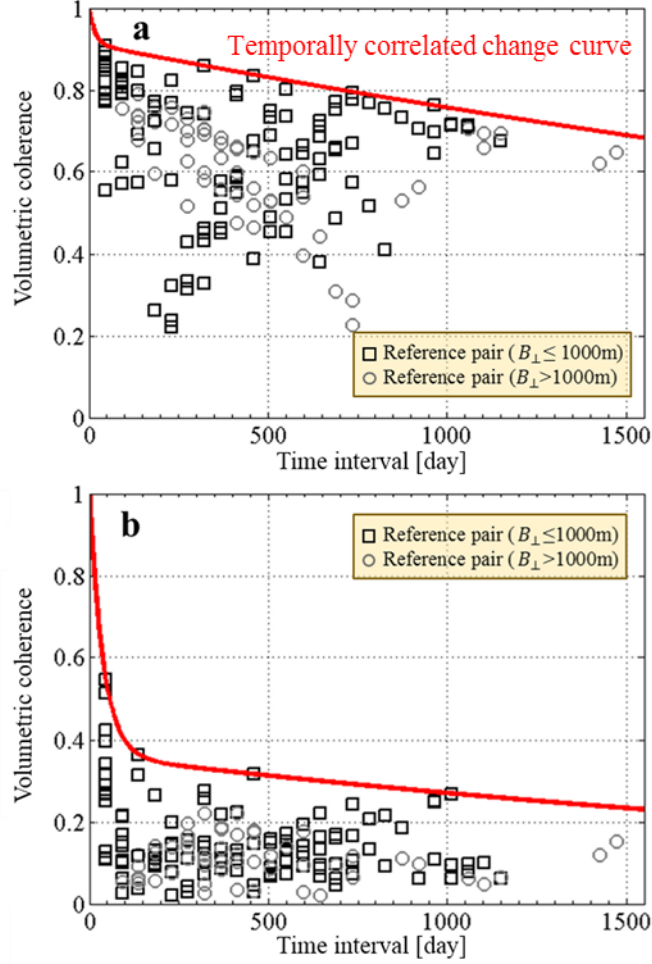


Fig. 3. 7. Estimation of the temporally correlated changes in temporal decorrelation using exponential curve fitting. Coherence distribution along the time axis for (a) man-made structure (denoted B in Fig. 3.8) and (b) forest area (denoted D in Fig.3.8). Squares and circles are the measured coherence. Red lines indicate the decorrelation related to the temporally correlated dielectric changes.

envelope, the model parameters are out of the range and the possible explanation about the physical meaning does not exist.

The accuracy of estimation using maxima is deeply related to the number of available pairs and time intervals. Because (3.1) assumes no $\gamma_{t_rand}^v$ and $\gamma_{t_rand}^g$, this assumption can be successful when there are sufficient numbers of scenes and pairs. Further, the number of maxima is important, because the shape of the envelope

is determined by maxima values. Therefore, long temporal baselines or many time intervals are also keys to more accurate estimation. In this study, although coherence maps with baseline within 5000 m were generated, most cases showed that coherences within 1000 m are closer to the envelope. In addition, the model parameters extracted from coherence showed high correlation with those with 1000 m. Therefore, the basis of the coherences with baseline within 1000 m tends to be representative of all coherence maps.

As shown in Fig. 3.8 and Table 3.2, the extracted parameters have different characteristic time and ground-to-volume ratios depending on the surface type. A high μ means that coherence is determined by one dominant scattering (ground), and τ_v is not important in the analysis. The high μ value is mainly observed in the bare soil and the manmade structures (areas A and B in Fig. 3.8). The τ_g value is higher in the manmade structures than in the bare soil because they are less affected by natural changes. Further, an interesting observation is that the values of μ , τ_g , and τ_v are different even in the same surface type, i.e., evergreen forest denoted as C and D in Fig. 6. Because the ground-to-volume ratio is related to not only surface type but also the properties of the canopy, a vegetated area could have a high μ value if the forest is not dense.

Table 3. 2. Extracted model parameter labeled in Fig. 3.8

Label	Landuse	Ground to volume ratio	Characteristic time [days]		Dominant scattering	Days when coherence is 0.5	Coherence after revisit intervals		
		μ	τ_g (ground)	τ_v (volume)			46 days	92 days	138 days
A	Bare soil	9.43	2888	77	Ground scattering dominant	1711	0.94	0.90	0.88
B	Man-made structure	9.89	6313	53	Ground scattering dominant	3768	0.94	0.91	0.90
C	Evergreen forest	4.05	627	142	Coupled scattering (Ground > Volume)	322	0.89	0.80	0.72
D	Evergreen forest	0.53	1219	49	Coupled scattering (Volume > Ground)	65	0.59	0.42	0.35

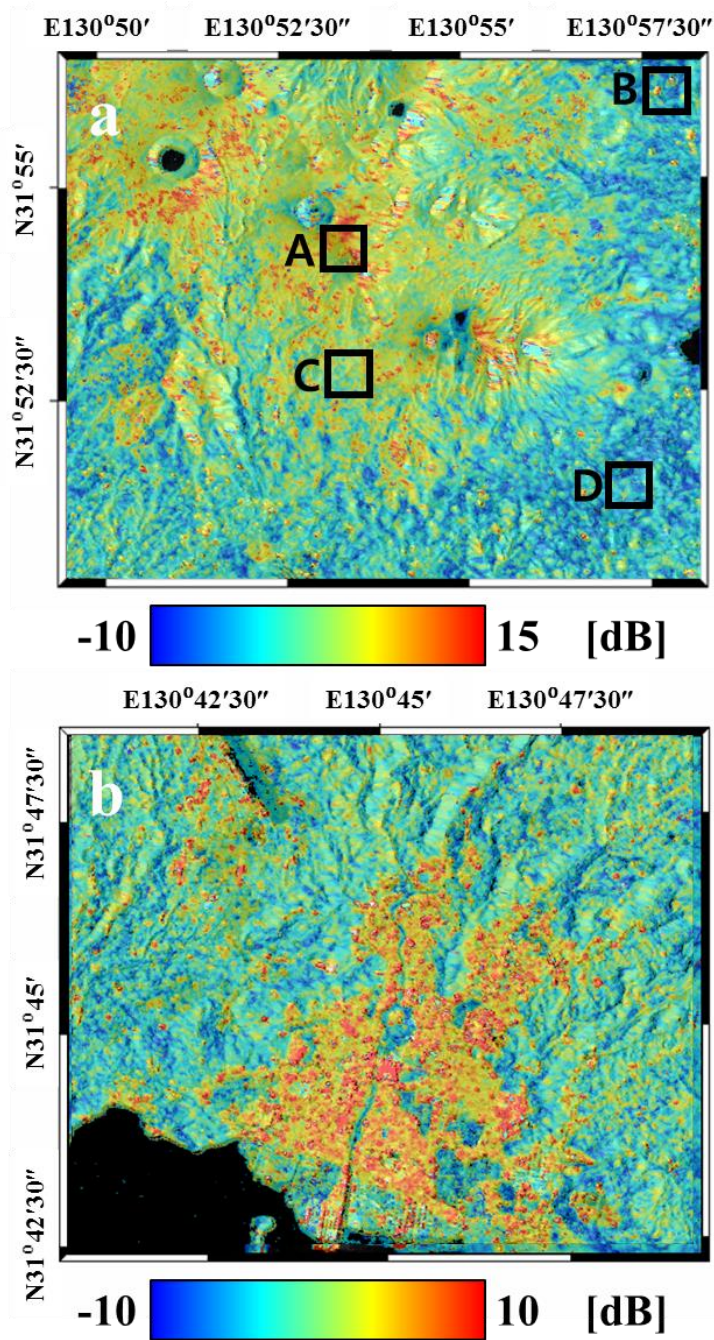


Fig. 3. 8. Estimated ground-to-volume ratio, μ , for (a) Kirishima volcano and (b) Kirishima city.

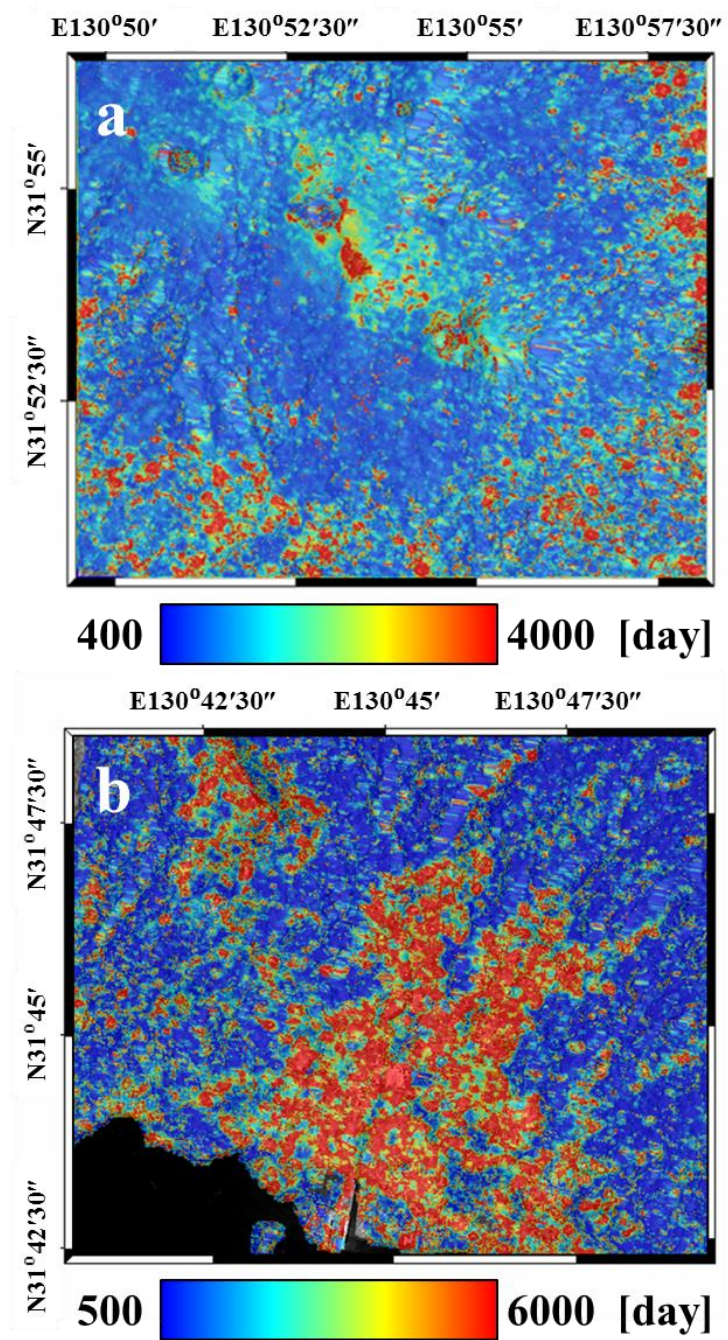


Fig. 3. 9. Characteristic time constant of the ground layer for (a) Kirishima volcano, and (b) Kirishima city.

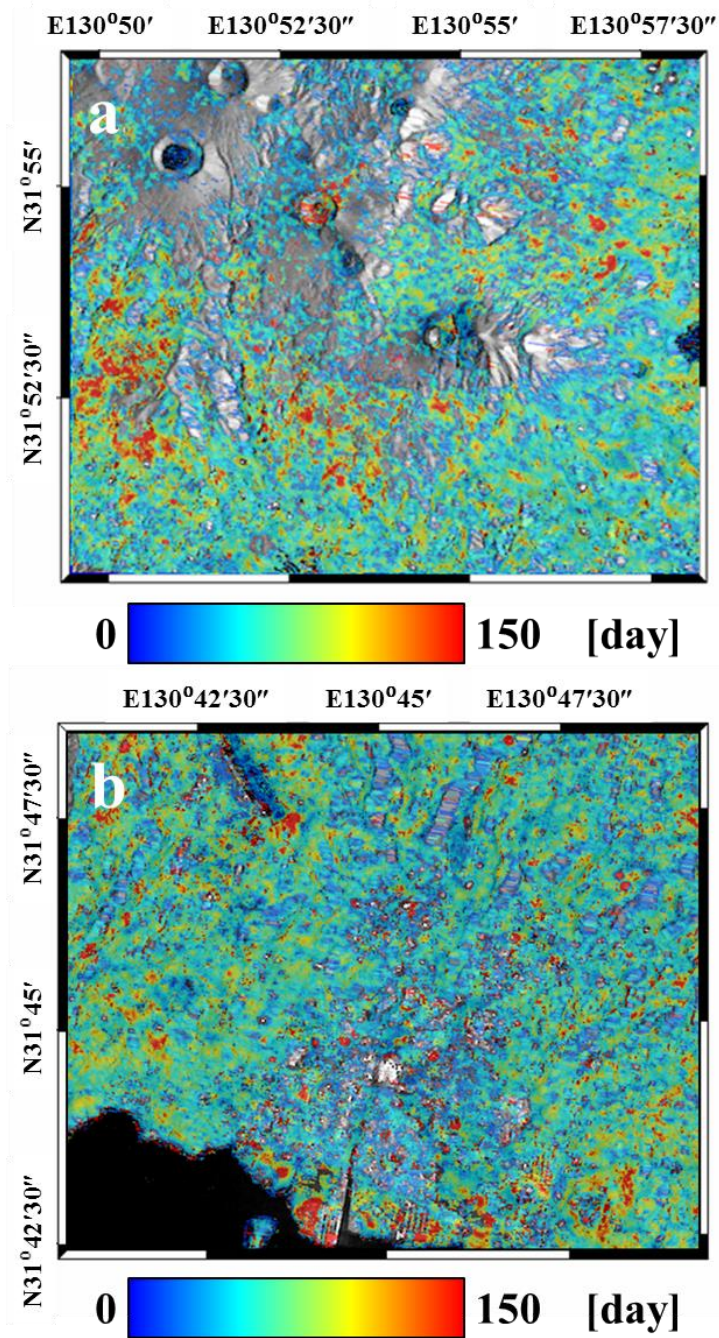


Fig. 3. 10. Characteristic time constant of the volume layer for (a) Kirishima volcano, and (b) Kirishima city

The third step is calculation of the portion (or contribution) of coherence between ground, $\alpha_g = \gamma_{t_corr}^g / (\gamma_{t_corr}^g + \gamma_{t_corr}^v)$, and volume, $\alpha_v = 1 - \alpha_g$, in each time interval, based on the estimated μ , τ_g , and τ_v . Even though the parameters, τ_g , τ_v , and, μ were already extracted in the preceding step two, the number of unknown variables is $2N$, which exceeds the number of coherence maps, N . Therefore, another assumption needs to be applied to reduce the number of variables. In this study, α_g is a key factor in solving the problem. Portion α_g is a timespan variant variable. In the general case, α_g increases in temporally correlated coherence as the timespan increases because τ_g is higher than τ_v . The targets such as manmade structures and bare soil have high μ , thus, the ground contribution is assumed to be dominant in every timespan.

The fourth step is estimation of the random (temporally uncorrelated) coherence changes of ground, $\gamma_{t_rand}^g$. In the pixels with a high proportion of the ground component, the temporal decorrelation is determined by only ground-dominant scattering, that is (3.1) is reformulated as,

$$\text{if } \alpha_g > 0.9, \gamma_t^{high} = \exp\left(-\frac{\Delta T}{\tau_g}\right) \quad (3.2)$$

$$\gamma_{d,rand}^g = \frac{\gamma_{obs}}{\left[\exp\left(-\frac{\Delta T}{\tau_g}\right)\right]} \quad (3.3)$$

Thus, it is necessary to find ground-scattering dominant pixels before performing (3.3). The decorrelation components, $\gamma_{t_rand}^g$, are related to the changes in the dielectric properties induced by rain, snow, and seasonal changes. Therefore, the extracted parameters, $\gamma_{t_rand}^g$, can be used to explain loss of coherence and statistical analysis of natural phenomena on ground-scattering dominant pixels. It is worth

noting that pixels with high α_g and μ are usually less affected by the contribution of the volume. This implies that the perpendicular baseline criterion is unnecessary, and that pairs with higher baseline are available for extracting $\gamma_{t_rand}^g$.

The fifth step is the extraction of the model parameters, $\gamma_{t_rand}^g$, and $\gamma_{t_rand}^v$, in the pixels where the effects are coupled ($\alpha_g \leq 0.9$). According to the proposed temporal decorrelation model, each decorrelation caused by the temporally uncorrelated changes starts from each coherence level of the temporally correlated changes. Thus, the logical implication that “if one of the temporally correlated changes is dominant, then the corresponding temporally uncorrelated changes is dominant” is reliable. For the pixels with $0.9 \geq \alpha_g > 0.5$, the ground contribution is more dominant than the volume effect. In order to solve the equation, $\gamma_{t_rand}^v$ is thus assumed to be negligible. Likewise, $\gamma_{t_rand}^g$ should be ignored. This approach should be performed in each pixel and in each pair, because pixels have different τ_g , τ_v , and μ , and α_g and α_v are different in every timespan.

$$\text{if } 0.9 \geq \alpha_g > 0.5, \quad \gamma_{t_rand}^g = \frac{\gamma_{obs} - \frac{1}{1+\mu} \exp\left(-\frac{\Delta T}{\tau_v}\right)}{\frac{\mu}{1+\mu} \exp\left(-\frac{\Delta T}{\tau_g}\right)} \quad (3.4)$$

$$\text{if } \alpha_g \leq 0.5, \quad \gamma_{t_rand}^v = \frac{\gamma_{obs} - \frac{\mu}{1+\mu} \exp\left(-\frac{\Delta T}{\tau_g}\right)}{\frac{1}{1+\mu} \exp\left(-\frac{\Delta T}{\tau_v}\right)} \quad (3.5)$$

3.4. Probability map generation

In Chapter 3.2 and Chapter 3.3, the temporal decorrelation model was presented and the procedure for extracting the model parameters was described from multi-temporal data having single-polarization. In this section, the procedure to estimate

the changed area using model parameters will be outlined. Firstly, it is worth noting that the decorrelation effects are concentrated near the estimated envelope, as shown in Fig. 3.7. This implies that the decorrelation related to random natural changes typically induce coherence that is concentrated at a certain level. Therefore, it can be assumed that $\gamma_{t_rand}^g$ and $\gamma_{t_rand}^v$ are non-uniformly distributed. A major event, such as volcanic ash, building collapse, or landslide, has a stronger contribution to the loss of coherence than the usual decorrelation related to natural phenomena. Accordingly, a major event usually results in lower $\gamma_{t_rand}^g$ and $\gamma_{t_rand}^v$ (brown bars in Fig. 3.11). A cumulative distribution function (CDF) of reference pairs (black lines in Fig. 3.11) offers statistical information about how strong and often the natural phenomena usually affect the observed coherence. Therefore, if these model parameters extracted from the event pair set are located at the tail of the probability density function (PDF), they can be assigned as “changed pixels,” as indicated by the red rectangles in Fig. 3.11.

However, the PDF of the model parameters is undefined, the shape of the function is unknown, and the sample is also finite. Kernel density estimation (KDE) is an appropriate method for estimating unknown probability density functions by smoothing the finite and discrete samples (Bowman et al., 1997). Thus KDE can be applied to estimate the PDF and then the continuous CDF of $\gamma_{t_rand}^g$ and $\gamma_{t_rand}^v$ of reference pairs can be built.

The statistics of model parameters was analyzed depending on the dominant scattering because the numbers of available pairs are different. For example, when pixels are assigned as ground-dominant pixels ($\alpha_g > 0.9$), the interferometric pairs can be chosen without consideration of perpendicular baseline. In this study, a histogram of $\gamma_{t_rand}^g$ using 196 pairs (166 reference pairs and 30 event pairs) below 5000 m was generated to estimate PDF using the KDE method (Fig. 3.11(a)). When the pixels are affected by the ground-volume-coupled effect ($\alpha_g \leq 0.9$), then

estimation of the CDF has to be performed separately. Further, when α_g is greater than 0.5, the $\gamma_{t_rand}^g$ of reference pairs is used to estimate CDF, as shown in Fig. 3.11(b.1). Otherwise, $\gamma_{t_rand}^v$ is used, as shown in Fig. 3.11(b.1). Consequently, two CDFs can exist in the coupled effect pixels. It is also worth noting that the number of interferometric pairs used in CDF is smaller than the number of ground-dominant pixels owing to the limitation of the baseline (<1000 m). In this case, 47 reference pairs and three event pairs were generated.

On the basis of the estimated cumulative density function from the reference pair set, the probability of a region having changed can be calculated using event pairs. Because two ALOS-PALSAR scenes were acquired after the volcanic eruption, it is obvious that they include the decorrelation caused by volcanic ash. Among all coherence maps generated using event pairs, only three interferometric pairs met the required baseline criterion, as shown in Fig 3.6. One thing to keep in mind when interpreting the estimated probability is that the high probability results not only from volcanic ash, but also other factors including heavy rain, strong wind, and other temporary changes. One simple and effective way to mitigate such short-lived events, compared to volcanic ash fall, is to average the probability of all pairs spanning the event. Averaging the probability plays an important role in enhancing the contribution of the interesting event, which is volcanic ash. Fig. 3.12 (a) shows the averaged probability map, on which the effect of volcanic ash is clearly observed near the southeast of the Shinmoedake volcano. Further, significantly high probability values are sparsely distributed in Kirishima city (Fig. 3.12(b)). This implies that Kirishima city was not affected by regional changes such as volcanic ash. Therefore, the result of Kirishima city clearly proves that the method proposed in this research effectively discriminates changed regions from unchanged regions.

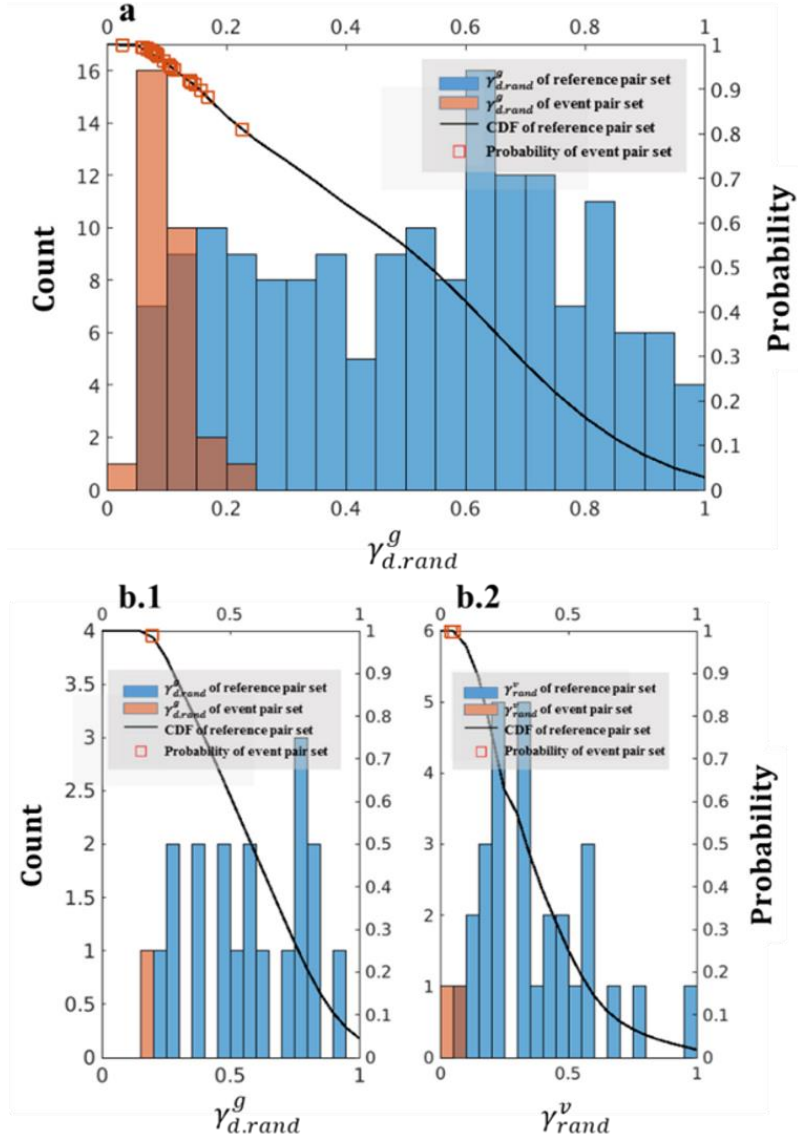


Fig. 3. 11. (a) Histograms (blue bar) of $\gamma_{t.rand}^g$ in ground-dominant pixels and (b) $\gamma_{t.rand}^g$ and γ_{rand}^v in ground-and-volume-coupled pixels. Brown histograms indicate corresponding value in event pair. Black lines are the estimated cumulative density functions using KDE, and red boxes are probability of event. This analysis was performed in the area denoted as A and D in Fig. 3. 8

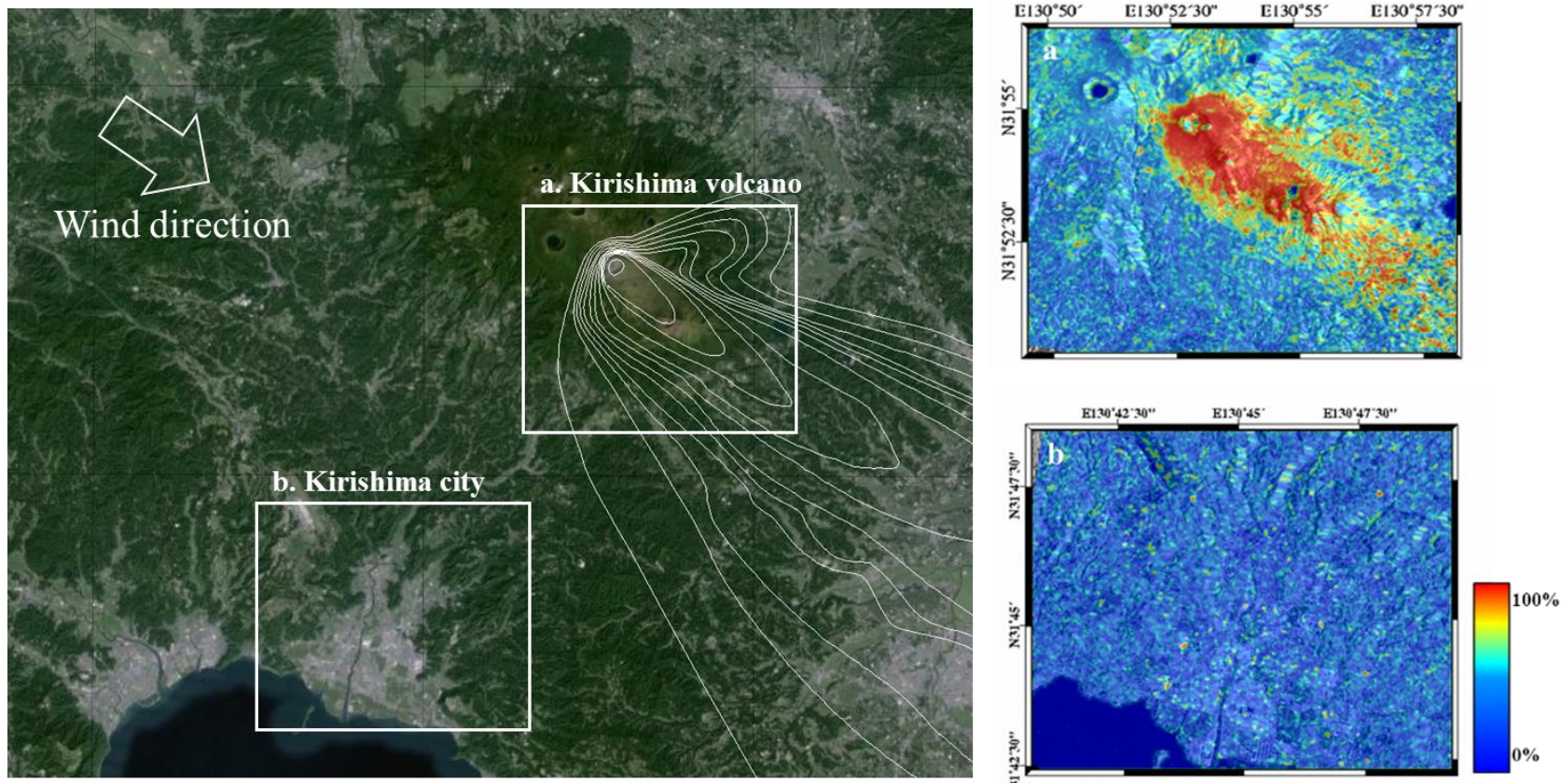


Fig. 3. 12. Calculated probability change map for (a) Kirishima volcano and (b) Kirishima city.

3.5. Mapping volcanic ash

To map volcanic ash, the probability maps, the in-situ measurement and the contour lines created from in-situ data were compared (Miyabuchi et al., 2013; Technology, 2011). According to (Miyabuchi et al., 2013), the tephra plumes after eruption were dispersed by the wind and deposited southeast of the Shinmoedake volcano. Further, the thickness of volcanic ash deposits reached 4.5 to 25 cm in the proximal area. A comparison between the depth of the volcanic ash deposit and the probability map generated from this analysis showed a high probability over 2 cm, which corresponds to approximately 75%. For comparison with the contour lines, the probability values, which are located between the contour line and the next level of the contour line, were averaged. Accordingly, the values at the x-axis in Fig. 3.13(d) represent the levels between two contour lines. The analysis with the area density shows a high correlation over 10 kg/m^2 . This result does not mean that the calculated probability is directly related to the depth or the area density of the volcanic ash. In general, thicker volcanic deposit might cause more phase alteration and thus strong temporal decorrelation. In addition, the probabilities at manmade structures are higher than other areas over 10 kg/m^2 . The estimated probability is determined by the temporal behavior of coherence of the scatterers. If the scatterers are less affected by the natural phenomena, the historical coherence tends to be concentrated on a certain level. If a small amount of volcanic ash induces relatively low coherence, it can result in a high probability. This implies that even though the same amount of volcanic ash was deposited, the sensitivity of change detection could be different. In the forest area, the random motion of volume and temporally uncorrelated dielectric changes are coupled in a complicated manner. This area is prone to decorrelation, and the coherence is concentrated in the low values. Thus, the decorrelation caused by a small amount of the volcanic ash may be hidden or

unclear owing to the strong natural changes.

The analysis also shows that volcanic ash deposit below 10 kg/m^2 is uncorrelated with the probability. In order to mask out uncorrelated probability, 75% level was selected as the threshold because 1σ (standard deviation) of uncorrelated probability reaches a maximum of 75%. Finally, the change detection maps caused by the deposit of volcanic ash can be generated, as shown in Fig. 3.13 (a).

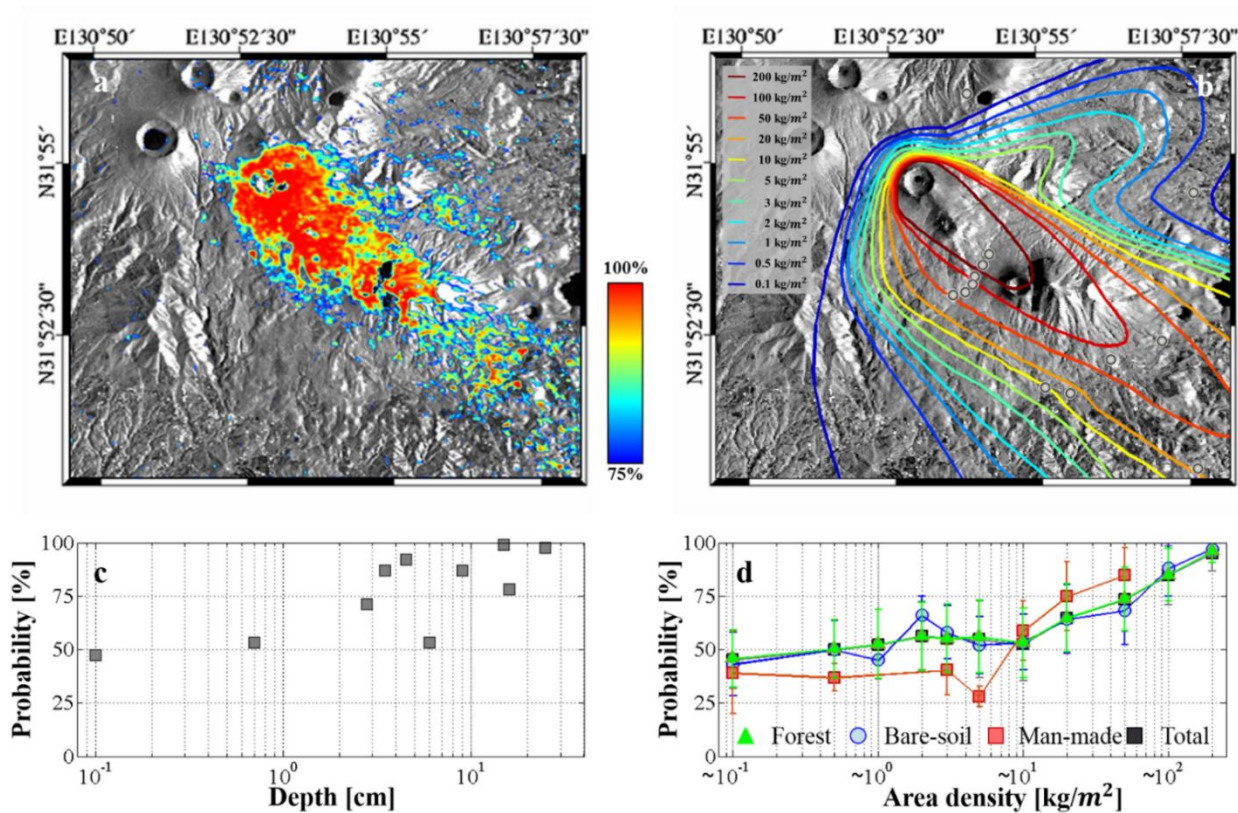


Fig. 3. 13. (a) Estimated probability map over 75% and (b) the predicted distributed map of the volcanic ash and location of in-situ depth data. Comparison between estimated probability and (c) the depth of volcanic deposits and also between (d) area densities.

3.6. Discussion

In this study, the temporal decorrelation model is proposed for coherence maps generated by multi-temporal and single-polarimetric data to identify regions changed as a result of the deposit of ash that follows volcanic eruptions. The proposed temporal decorrelation model uses the ground-to-volume ratio, random motion of volume, temporally correlated dielectric changes in volume and ground, and temporally correlated changes in volume and ground. Because the number of variables involved in the temporal decorrelation exceeds the number of available equations, several plausible assumptions were made. Also, pixels with many scatterers have different temporal decorrelation behaviors depending on the temporally correlated dielectric changes and ground-to-volume ratio. In addition, the temporally uncorrelated dielectric changes and random motion of volume were also estimated based on analysis of the portion of ground and volume coherence. To identify the coherence changes related to alterations in natural conditions, such as seasonal changes and meteorological phenomena, the KDE method was used to estimate the CDF for each pixel. Extreme changes caused by unexpected events such as deposition of volcanic ash, which yield abnormal values in the coherence map, were successfully extracted based on the CDF.

The proposed temporal decorrelation model was applied into CCD and used it to estimate the physical parameters of the forest. The model carries out quantitative analysis involving physical parameters, which is not a common approach in CCD techniques. Consequently, it is very useful in areas with a variety of decorrelation sources. The special significance of the proposed method is that the model considers most of the decorrelation effects in order to be useful for many realistic and complex change detection applications. Also, the extracted parameters from the temporal

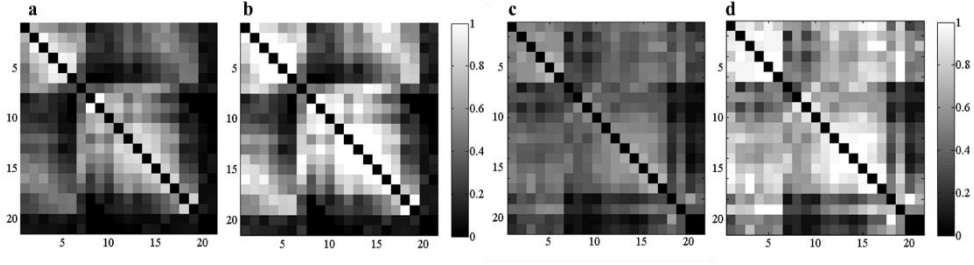


Fig. 3. 14. (a and c) Two examples of coherence covariance matrix and (b and d) $\gamma_{t,rand}^g$ matrices. (a) and (b) show the temporal behavior of bare soil, denoted A in Fig. 3.6, and (c) and (d) are denoted B in Fig. 3.6.

decorrelation, which contains one of the natural change information, can enhance its event information by reducing the effect of the temporally correlated changes as shown in Fig 3.14. This advantage makes the technique detect the event better.

However, the several assumptions used to solve the main equation could still be controversial. Fortunately, recently developed fully polarimetric and interferometric SAR sensors onboard UAVSAR and ALOS-2 could reduce the effect of the assumptions or even render them more realistic. Further research using these sensors can show the usefulness of the temporal decorrelation model for the extraction of reliable physical parameters, and generate more robust damage detection maps.

Chapter 4.

Damage mapping using temporal decorrelation model for multi-temporal and fully-polarized SAR data

SAR system and its applications have been dramatically developed during past decades. Recently advanced SAR systems can obtain fully-polarized images which can be applied to the interferometric techniques, which is called as Polarimetric and Interferometric SAR (PolInSAR). The development of SAR system has introduced the innovative applications of remote sensing and Earth system science studies. Also, the PolInSAR system is able to overcome the limitation of the conventional interferometry which has an uncertainty of phase center by providing the sensitive information of vertical distribution related to scattering mechanism. Based on this advance, the applications of PolInSAR can estimate accurately the physical parameters of forest including the canopy height.

However, the coherence change detection and damage mapping using PolInSAR, which is major subjective of remote sensing studies, is not fully studied. Firstly, the many applications for change detection utilize the amplitudes which have information of scattering mechanism. PolInSAR techniques measure not only the amplitude of scatterers but also the phase information related to the distance. For this advantage, more information could be exploited. Secondly, since the existence of the temporal decorrelation is not fully understood and may restrict the application by yielding the ambiguity of the physical interpretations. Thus, the temporal decorrelation involved in PolInSAR needs to be studied for better interpretation.

In the previous Chapter 2, a temporal decorrelation model was formulated to explain the coherence behaviors observed in time-series data with long temporal

baselines and single polarized data (Jung et al., 2016). The damage detection was successful, even in vegetated areas, using a temporal decorrelation model estimated from the historical statistics of natural change. However, the estimation uncertainty of model parameters still remained, because parameter extraction from single polarization data required several assumptions due to the unmatched number of observations and unknowns.

In contrast to Chapter 3, here fully-polarimetric-interferometric Uninhabited Aerial Vehicle SAR (UAVSAR) data will be used to address the uncertainty in the temporal decorrelation of the ground and volume layers. The remainder of this chapter is organized as follows. In Chapter 4.1, Lake Fire in California (2015) and the UAVSAR data used in this study are introduced. Chapter 4.2 address the conventional methods for change detection and evaluate the performance. The limitations of these methods are also revealed. In Chapter 4.3, the damage mapping algorithm proposed in this study will be explained in detail. Furthermore, the damage mapping result is evaluated. Chapter 4.4 explains the applicable conditions that this algorithm can be applied. In Chapter 4.5, the quantitative comparison between the damage mapping algorithms in Chapter 4 and Chapter 3 is carried out. Finally, the key finding and the potential issue in this study is summarized in Chapter 4.6.

4.1. Description of Lake Fire and UAVSAR data

UAVSAR is an airborne SAR system developed and operated by the Jet Propulsion Laboratory (JPL) (Hensley et al., 2008). The UAVSAR instrument is mounted on a Gulfstream-III aircraft and employs a full quad polarimetric L-band system with a bandwidth of 80 MHz. Accordingly, the theoretical slant range resolution is 1.87 m and the azimuth resolution is about 0.8 m. The mean flight altitude is 12.5 km and look angle ranges from 28° to 66°. One benefit of using the

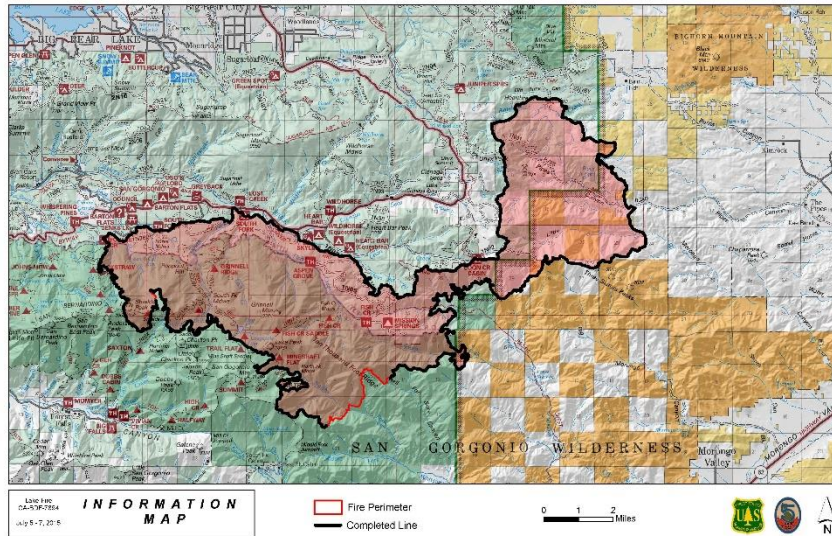


Fig. 4. 1. A burnt area map of Lake fire. The image is provided from the Incident Information System (<http://inciweb.nwcg.gov/>).

UAVSAR system is that the position of UAVSAR can be controlled precisely to within 5 m diameter tube of the designed flight track, making it suitable for repeat-pass interferometry with the assumption of zero spatial baselines. A specification of UAVSAR is summarized in Table. 1.

In this study, a stack of 15 repeat-pass polarimetric UAVSAR images acquired from 2009 to 2015 over the San Bernardino National Forest in California, United States, is used in order to evaluate the potential of the coherence model to delineate the damaged area. The natural disaster event this study focused on is the wildfire Lake Fire, which burned more than 31,350 acres from June 17, 2015, to July 21, 2015. The UAVSAR instrument was deployed on June 29, 2015, during the wildfire in coordination with NASA headquarters and the UAVSAR team at JPL. Due to this effort, 14 scenes before the event, and 1 scene during the event were able to be collected. For simplicity, hereafter the interferometric pairs acquired before the event are referred as the *reference set*, and those acquired spanning the event as the *event set*. Each acquisition date is listed in Table. 2. The minimum and maximum temporal

baselines were 43 and 2,258 days, respectively, which can be categorized as interferometric pairs with a long temporal baseline. The spatial interferometric baseline for all flights of the reference and event sets was within 5 m. The limiting value of 5m for the spatial baseline corresponds to a vertical wavenumber of 0.04 rad/m and 0.01 rad/m in near and far range, respectively. Assuming a reference tree height of 30m, the volumetric decorrelation calculated from a conservative SINC model is 0.94 and 0.99, respectively (S. R. Cloude, 2010). Thus, it is reasonable to assume that the geometric and volumetric decorrelations were negligible and that the estimated coherence carries only the effects of temporal decorrelation.

Table 4. 1. Sensor parameters of UAVSAR system.

parameter	Value
Frequency	L-Band 1217.5 to 1297.5 MHz
Bandwidth	80 MHz
Resolution	1.67 m Range, 0.8 m Azimuth
Polarization	Full Quad-Polarization
ADC Bits	2,4,6,8,10 & 12 bit selectable BFPQ, 180Mhz
Waveform	Nominal Chirp/ Arbitrary Waveform
Antenna Aperture	0.5 m range /1.5 azimuth (electrical)
Azimuth Steering	Greater than $\pm 20^\circ$ ($\pm 45^\circ$ goal)
Transmit Power	> 3.1 kW
Polarization Isolation	<-25 dB (<-30 dB goal)
Swath Width	> 23 km

Table 4. 2. UAVSAR data used in this study.

Index	Acquisition date	Index	Acquisition date
1	2009.04.23	9	2012.04.27
2	2009.09.18	10	2013.05.31
3	2010.03.03	11	2014.01.17
4	2010.04.15	12	2014.10.23
5	2010.10.14	13	2015.01.08
6	2010.12.07	14	2015.05.11
7	2011.07.08	15	2015.06.29
8	2011.10.28		

4.2. Brief analysis of SAR amplitude and interferometric coherence

According to the land cover data, the west part of the image contains Pinyon-Juniper Woodland, Dry-mesic Mixed Conifer Forest, and Jeffrey Pine-(Ponderosa Pine) Woodland (Homer et al., 2007). In contrast, the desert scrub and outcrop area are mainly observed over the east part of the scene. The different land cover yields the different signature of polarimetric SAR images. As observed in Fig. 4. 3, which is constructed using Pauli basis, the relatively strong volume scattering is observed in western part, while the surface scattering is dominant in eastern parts.

One of the simple and robust change detection methods is to generate the difference or ratio of the amplitude of SAR images acquired before and after the event, which is categorized as the incoherent change detection. The studies to evaluate the amplitude or intensity changes due to the fire has been proposed in the literature (Bourgeau-Chavez et al., 2007; Goodenough et al., 2012; Florian Siegert et al., 2000; F Siegert et al., 2000). For testing the potential of the incoherent

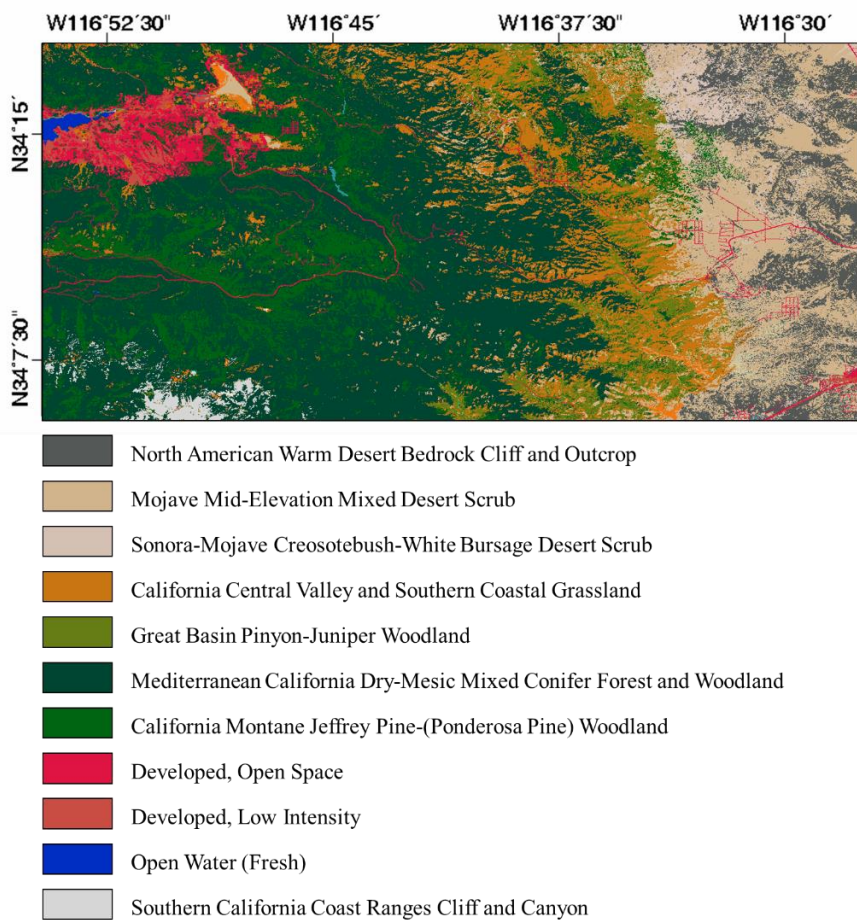


Fig. 4. 2. Land cover maps of Study area provided from National Gap Analysis Program.

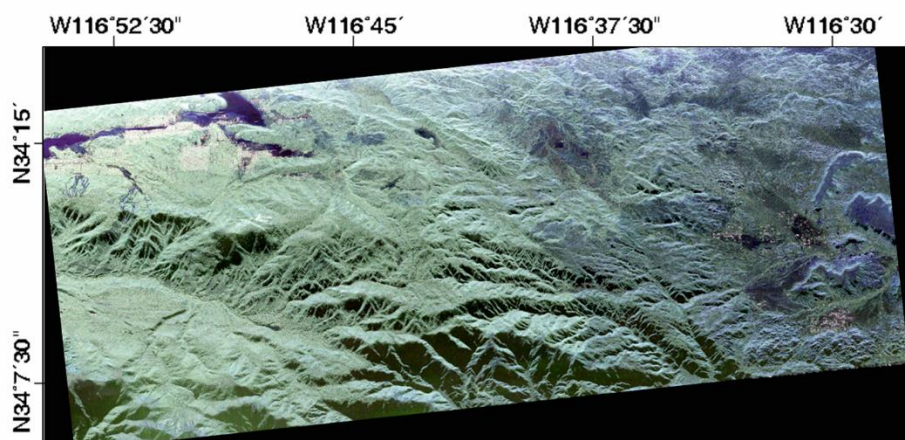


Fig. 4. 3. UAVSAR image acquired on April 23, 2009. The color composite image was reconstructed using Pauli basis. R: HH-VV, G: 2HV, B: HH+VV.

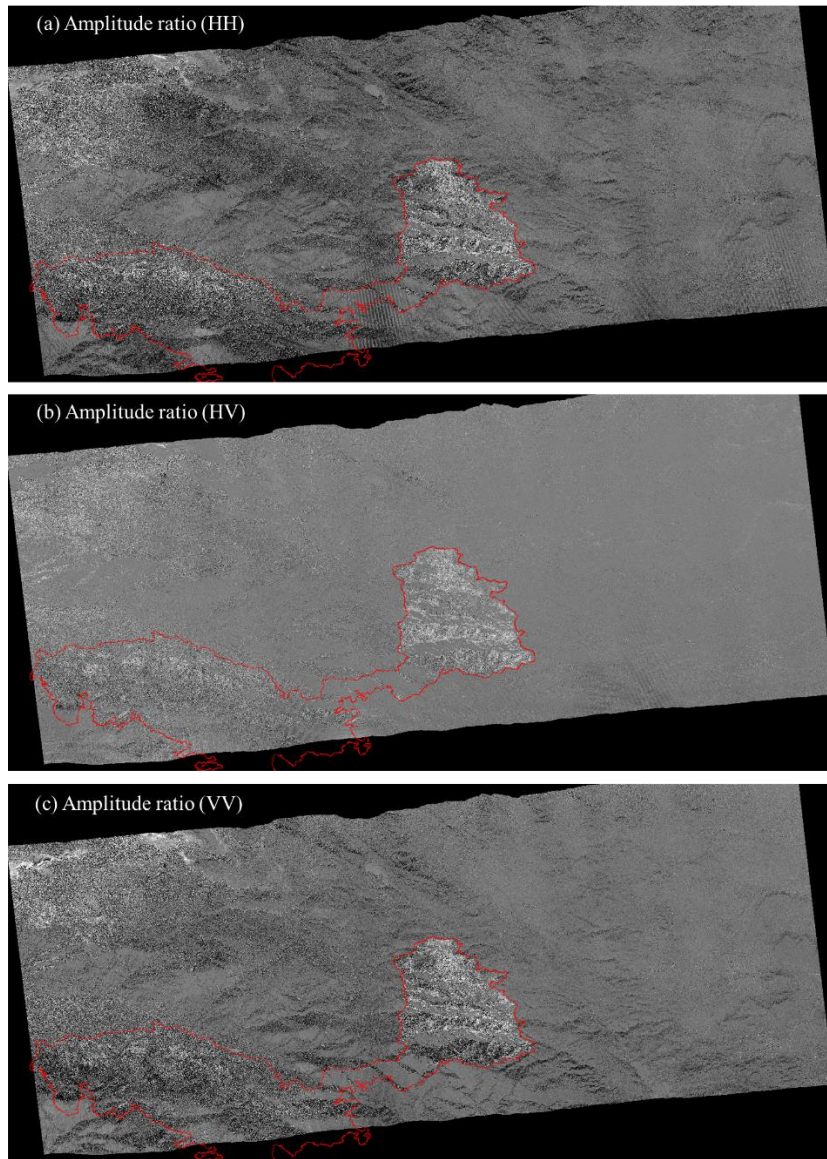


Fig. 4. 4. Amplitude ratio between images acquired on May 11, 2015, and June 29, 2015, for (a) HH, (b) HV, and (c) VV polarizations.

change to detect the damaged area, the amplitudes of the scene with HH, HV, and VV polarization acquired on May 11, 2015, were simply divided by the polarimetric amplitude acquired on June 29, 2015. The results are illustrated as log scale in Fig. 4. 4. According to the study exploiting the backscattering change after fire, the

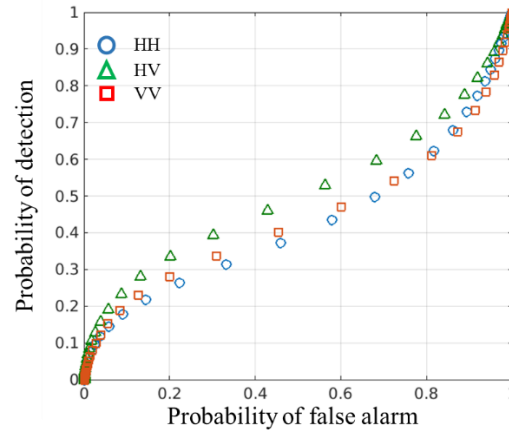


Fig. 4. 5. ROC curve for amplitude ratio in Fig. 4. 4.

backscattering signal decrease, especially in HV polarization (Goodenough et al., 2012; Siegert & Ruecker, 2000). Similarly, the burnt area located in the center of images shows high value due to the decreased backscattered signal. However, the burnt scar cannot be discriminated accurately on the left side of images. The receiver operating characteristic (ROC) curve shows the quantitative potential to discriminate the burnt area from the unburnt area. However, the amplitudes in all polarization have poor sensitivity to the damage caused by fire, although HV polarization amplitude ratio is slightly more sensitive.

The polarimetric characteristics of elements in the resolution cell affect not only the scattering mechanism of polarimetric SAR but also yield different coherence behaviors. As mentioned, the coherences generated from the interferometric approaches is determined by the thermal and temporal decorrelation only. If the SNR is assumed high enough to ignore the thermal decorrelation, the temporal decorrelation is the only main determinants of the coherence. Under this assumption, the averaged coherence using SAR data acquired before the event shows relatively low coherence (0.3~0.5) in western area where the volume scattering is strong. The possible explanation is that the resolution cell with vegetated area is prone to be

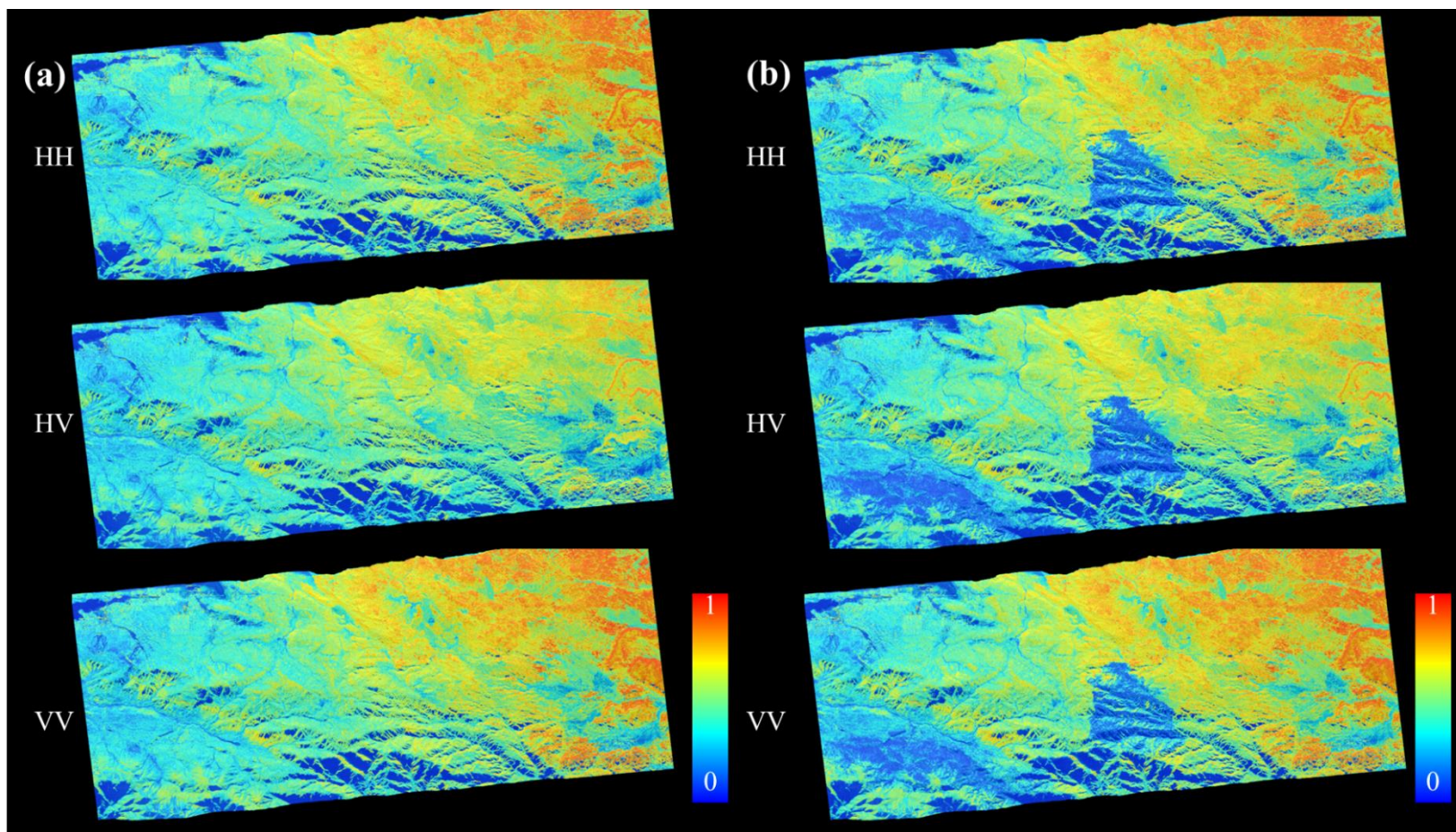


Fig. 4. 6. Averaged coherence maps using HH, VV, and HV images (a) acquired before the fire and (b) acquired crossing the fire.

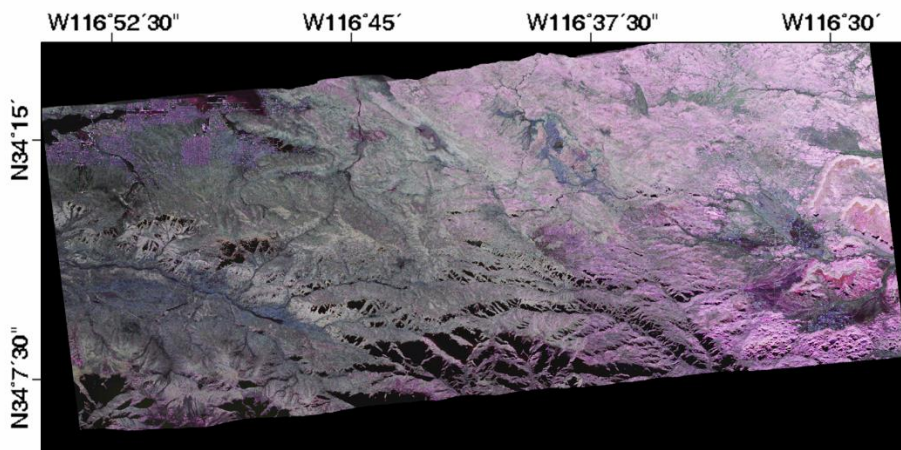


Fig. 4. 7. Color composite image using coherence maps generated from interferometric pairs acquired before the fire. R: VV coherence G: HV coherence B: HH coherence.

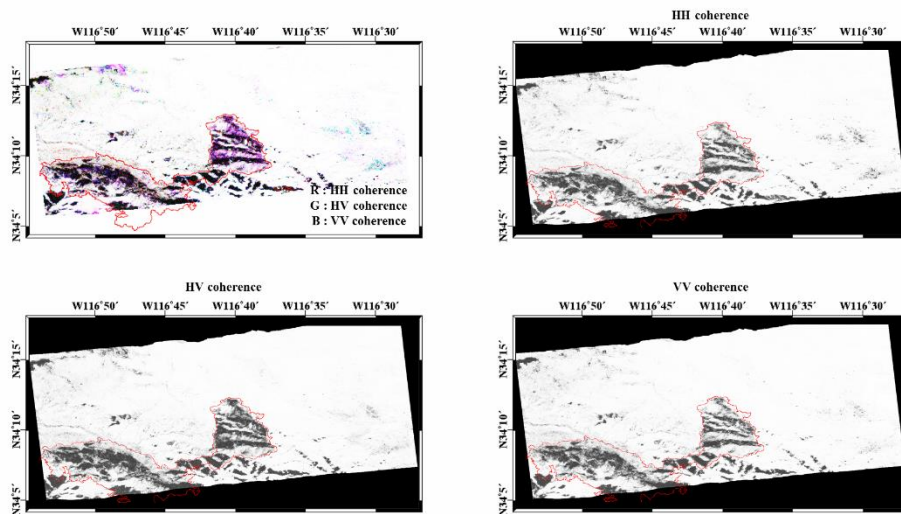


Fig. 4. 8. Coherence maps generated from the interferometric pairs acquired on May 11, 2015, and June 29, 2015, for HH, VV, and HV polarization. The Lake fire started on June 17, 2015.

affected by biological growth, and motions of volume layer such as leaves or branches caused by the wind. The eastern area which the only low vegetation exist shows high coherence (0.6~0.9) in HH, HV, VV image comparing the western site. The high coherence implies the area has high phase stability in time because of low precipitation and low contribution of vegetation.

The effect of the changes caused by Lake Fire can be analyzed via the coherence changes analysis before and after the event. Two interferometric pairs were chosen, i.e. 2015.01.08 ~ 2015.05.11 and 2015.05.11 ~ 2015.06.29. As expected, the coherence of all polarizations decreased after the event where the fire occurred. The significant decrease is observed in HV polarization because the leaves to be sensitive to volume scattering is prone to be affected by the fire. However, the low coherence in area A does not fit to the predefined burnt area, while the low coherence in area B shows good agreement. The reason why the area A shows the discordance with the actual fire area could be that the area is less affected by the fire. A few coherent changes can be enhanced by differentiating the coherence maps before the events (2015.05.11 ~ 2015.06.29) with that across the event (2015.01.08 ~ 2015.05.11). This approach has been applied to extract the damaged area caused by the natural hazard. The coherence calculated from the interferometric pairs before the event contains the information of natural changes. If the similar amount of the natural changes is assumed in two interferometric pairs, the difference of two coherence maps means the stronger decorrelation caused by the event. The results show higher agreements with the predefined fire area comparing the method using only coherence. However, the method may have two critical limitations. Firstly, the assumption that the decorrelation caused by the natural change is same in the coherence maps should be satisfied in pixel by pixel. The temporal decorrelation of vegetated area is determined by the motions of leaves, and dielectric changes caused by natural

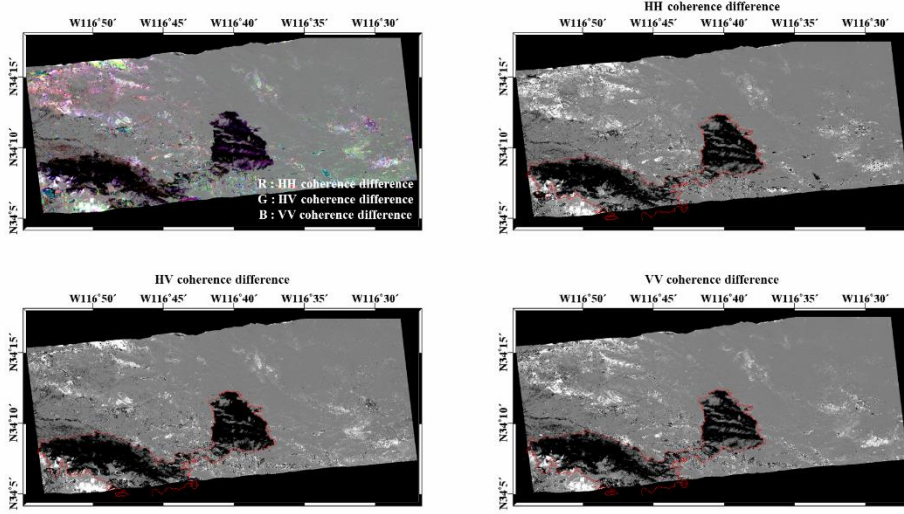


Fig. 4. 9. Coherence difference maps. The reference coherences are generated from the interferometric pair acquired on January 08, 2015 and May 11, 2015. The event coherence maps are calculated from the interferometric pair between May 11, 2015, and June 29, 2015. The black area means lowered coherence with respect to the reference coherence.

changes. However, the case is hardly satisfied. In addition, since the temporal baselines are different in the scene by scene, the effect of temporal decorrelation could be different. Also, the physical interpretation of the coherence differences is difficult even though the approach is simple and sometimes robust. Therefore, the coherence maps need to be interpreted using temporal decorrelation, then it should be extended to the applications.

4.3. Damage mapping algorithm using coherence model

In this chapter, the damage mapping algorithm using coherence model will be presented. The procedure for this algorithm consists of main three steps. The first is coherence optimization. Before the parameter inversion, the coherence is optimized

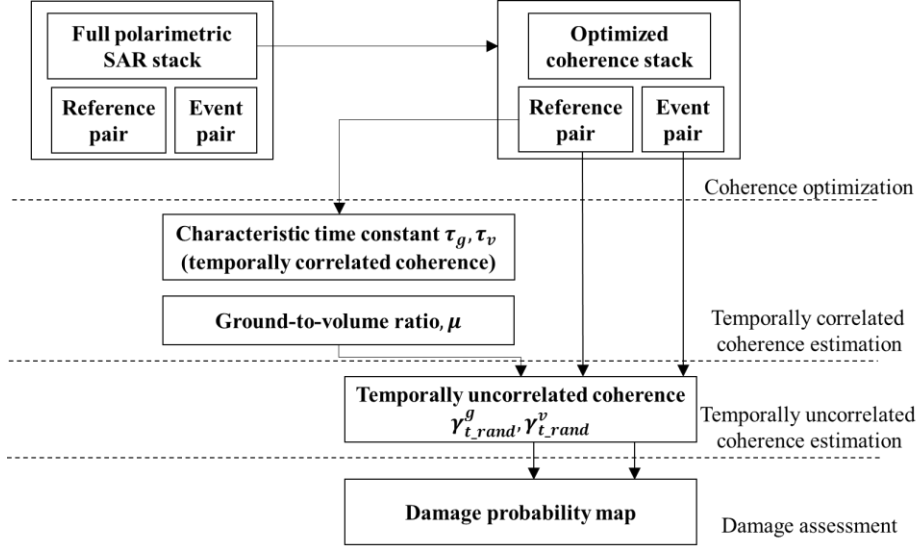


Fig. 4. 10. Flow chart for damage mapping.

in order to find the best polarization to explain the temporal decorrelation. Then, in the second step, the temporally-correlated coherence estimation is carried out. In the third step, the randomly occurring events in coherence stack are calculated. Finally, the probability related to the natural disaster is calculated.

4.3.1. Coherence optimization

Polarimetric SAR interferometry (PolInSAR) leads to the separation of scattering centers within a resolution by compromising the polarimetric and interferometric information. If the scattering matrix of one polarization basis is defined, the different orthogonal-basis can be generated by varying the polarization state. As the polarimetric basis changes, the unitary complex vectors can be obtained to optimize the coherence values and scattering mechanism (Qong, 2005). The conventional polarizations have separable phase centers and different coherences, but they are not optimized. The optimization process makes it possible to resolve the formulated

model as the algorithm provides the three independent scattering mechanisms

The basic observable of PolInSAR data is 6x6 coherency matrix, and can be described as,

$$\langle kk^{*T} \rangle = \begin{bmatrix} T_{11} & \Omega_{12} \\ \Omega_{21} & T_{22} \end{bmatrix} \quad (4.1)$$

Here, k means Pauli-vector of polarimetric radar observable.

$$k = \frac{1}{\sqrt{2}} [S_{hh}^1 + S_{vv}^1 \quad S_{hh}^1 - S_{vv}^1 \quad 2S_{hv}^1 \quad S_{hh}^2 + S_{vv}^2 \quad S_{hh}^2 - S_{vv}^2 \quad 2S_{hv}^2]^T \quad (4.2)$$

$$\begin{aligned} & [T_{11}] \\ &= \begin{bmatrix} \langle |S_{hh}^1 + S_{vv}^1|^2 \rangle & \langle (S_{hh}^1 + S_{vv}^1)(S_{hh}^1 - S_{vv}^1)^* \rangle & 2\langle (S_{hh}^1 + S_{vv}^1)S_{hv}^{1*} \rangle \\ \langle (S_{hh}^1 - S_{vv}^1)(S_{hh}^1 + S_{vv}^1)^* \rangle & \langle |S_{hh}^1 - S_{vv}^1|^2 \rangle & 2\langle (S_{hh}^1 - S_{vv}^1)S_{hv}^{1*} \rangle \\ 2\langle S_{hv}^1(S_{hh}^1 + S_{vv}^1)^* \rangle & 2\langle S_{hv}^1(S_{hh}^1 - S_{vv}^1)^* \rangle & \langle |4S_{hv}^1|^2 \rangle \end{bmatrix} \end{aligned} \quad (4.3)$$

$$\begin{aligned} & [T_{22}] \\ &= \begin{bmatrix} \langle |S_{hh}^2 + S_{vv}^2|^2 \rangle & \langle (S_{hh}^2 + S_{vv}^2)(S_{hh}^2 - S_{vv}^2)^* \rangle & 2\langle (S_{hh}^2 + S_{vv}^2)S_{hv}^{2*} \rangle \\ \langle (S_{hh}^2 - S_{vv}^2)(S_{hh}^2 + S_{vv}^2)^* \rangle & \langle |S_{hh}^2 - S_{vv}^2|^2 \rangle & 2\langle (S_{hh}^2 - S_{vv}^2)S_{hv}^{2*} \rangle \\ 2\langle S_{hv}^2(S_{hh}^2 + S_{vv}^2)^* \rangle & 2\langle S_{hv}^2(S_{hh}^2 - S_{vv}^2)^* \rangle & \langle |4S_{hv}^2|^2 \rangle \end{bmatrix} \end{aligned} \quad (4.4)$$

$$\begin{aligned} & [\Omega_{12}] \\ &= \begin{bmatrix} \langle (S_{hh}^1 + S_{vv}^1)(S_{hh}^2^* + S_{vv}^2^*) \rangle & \langle (S_{hh}^1 + S_{vv}^1)(S_{hh}^2 - S_{vv}^2)^* \rangle & 2\langle (S_{hh}^1 + S_{vv}^1)S_{hv}^{2*} \rangle \\ \langle (S_{hh}^1 - S_{vv}^1)(S_{hh}^2 + S_{vv}^2)^* \rangle & \langle (S_{hh}^1 - S_{vv}^1)(S_{hh}^2 - S_{vv}^2)^* \rangle & 2\langle (S_{hh}^1 - S_{vv}^1)S_{hv}^{2*} \rangle \\ 2\langle S_{hv}^1(S_{hh}^2 + S_{vv}^2)^* \rangle & 2\langle S_{hv}^1(S_{hh}^2 - S_{vv}^2)^* \rangle & \langle 4S_{hv}^1S_{hv}^{2*} \rangle \end{bmatrix} \end{aligned} \quad (4.5)$$

where subscription 1 and 2 represents the measurement at two acquisitions. T matrix is coherency matrix which has information of scattering mechanism. Ω matrix is polarimetric and interferometric matrix which its components have information of distance at each polarization. By introducing the unitary vector ω_i and ω_j , the generalized complex correlation is written as,

$$\gamma_{ij}(\omega_i, \omega_j) = \frac{\omega_i^* \Omega_{ij} \omega_j}{\sqrt{\omega_i^* T_{ii} \omega_i \omega_j^* T_{jj} \omega_j}} \quad (4.6)$$

where $i \in [1, 2, 3, \dots, N]$, $j \in [1, 2, 3, \dots, N]$ and $0 \leq |\gamma_{ij}(\omega_i, \omega_j)| \leq 1$. Depending on choice of the arbitrary vectors ω_i and ω_j , the coherence changes on the defined basis.

For the optimization problem, the several approaches can be applied depending on the assumptions of unitary vectors (S. R. Cloude, 2010; Neumann et al., 2008; Qong, 2005). Here, the two representative methods are introduced by assuming two different unitary vectors or common unitary vectors.

Multi-scattering mechanism

The coherence optimization problem can be dealt with two cases; single baseline and multi-baseline data. If the available data is acquired at single baseline, the optimization process is confined with only finding the eigenvectors for two scattering mechanisms. The coherence optimization can be achieved by introducing the Lagrangian L and multipliers λ_i and λ_j .

$$L = \omega_i^* \Omega_{ij} \omega_j - \lambda_i (\omega_i^* T_{ii} \omega_i - 1) - \lambda_j (\omega_j^* T_{jj} \omega_j - 1) \quad (4.7)$$

The optimization of the Lagrangian problem is solved using its partial derivatives with respect to the variables.

$$\frac{\partial L}{\partial \lambda_i} = \omega_i^* T_{ii} \omega_i - 1 = 0 \quad (4.8)$$

$$\frac{\partial L}{\partial \lambda_j} = \omega_j^* T_{jj} \omega_j - 1 = 0 \quad (4.9)$$

$$\frac{\partial L}{\partial \omega_i^*} = \Omega_{ij} \omega_j - \lambda_i T_{ii} \omega_i = 0 \quad (4.10)$$

$$\frac{\partial L}{\partial \omega_j^*} = \Omega_{ij} \omega_i - \lambda_j T_{jj} \omega_j = 0 \quad (4.11)$$

Then, two 3 x 3 complex eigenvalue problem is obtained with common eigenvalues.

$$T_{jj}^{-1} \Omega_{ij}^* T_{ii}^{-1} \Omega_{ij} \omega_i = v \omega_j \quad (4.12)$$

$$T_{ii}^{-1} \Omega_{ij} T_{jj}^{-1} \Omega_{ij}^* \omega_i = v \omega_i \quad (4.13)$$

$$v = \lambda_i \lambda_j \quad (4.14)$$

The eigenvectors corresponding to eigenvalues can project the scattering vectors of each SAR images onto the new vectors to derive the optimized coherence.

$$nk_{i,opt} = \omega_{i,opt}^* k_i \quad (4.15)$$

$$nk_{j,opt} = \omega_{j,opt}^* k_j \quad (4.16)$$

The procedure is valid for the extraction of two scattering mechanisms of one polarimetric SAR interferometric pair. If the multi-temporal or multi-baseline data is available, the optimized coherences of each pair can be obtained by iterating the same procedure to each pair, independently. Let the number of images is N, then $N(N+1)/2$ interferometric pairs can be generated. The optimization process based on the single-baseline multi-scattering-mechanism (SB MSM) yields N-1 vectors for one reference image with respect to the remaining images. It is worth noting that the absolute phase of the vectors is not uniquely defined using eigenvalue problem. The interferometric phase is required so that

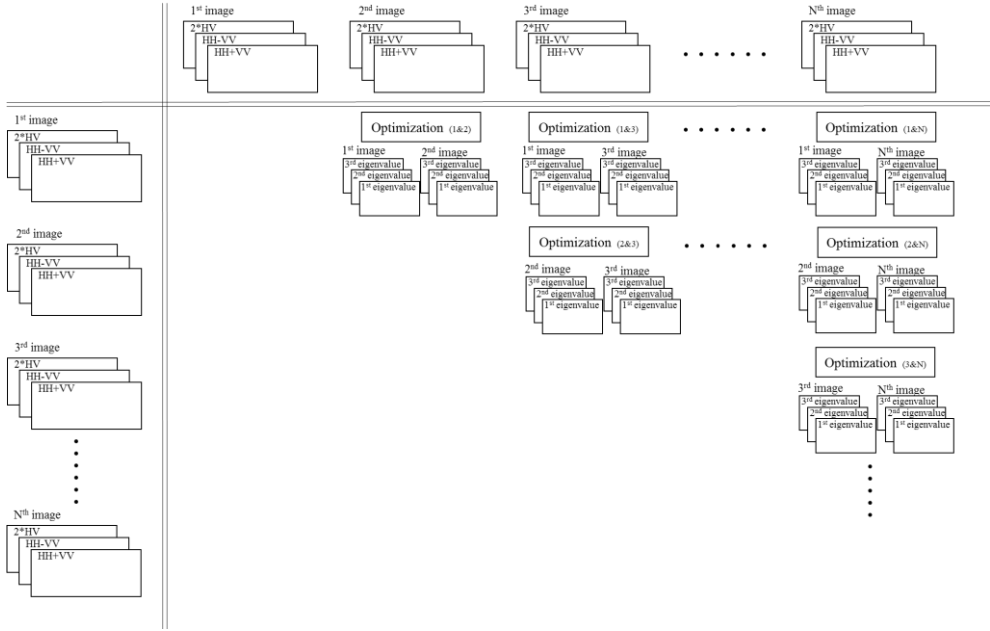


Fig. 4. 11. Interferometric coherence optimization scheme using single-baseline multi-scattering mechanism.

$$\arg(\omega_{i,opt}^* \omega_{j,opt}) = 0 \quad (4.17)$$

Thus, the additional compensation may be required as

$$\phi = \arg(\omega_{i,opt}^* \omega_{j,opt}) \quad (4.18)$$

$$\omega'_{j,opt} = \omega_{j,opt} \exp(-i\phi) \quad (4.19)$$

If more than 2 data are needed for the coherence optimization, another approach can be taken into the consideration, which calculates coherence using all available data.

This procedure is called as multi-baseline multi-scattering-mechanism (MB MSM)

The Lagrangian problem is written as

$$L = \sum_{i=1}^N \sum_{j=1 \neq i}^N \omega_i^* \Omega_{ij} \omega_j + \sum_{i=1}^N \lambda_i (\omega_i^* T_{ii} \omega_i - 1) \quad (4.20)$$

Then, partial derivatives of Lagrangian problem is rewritten as,

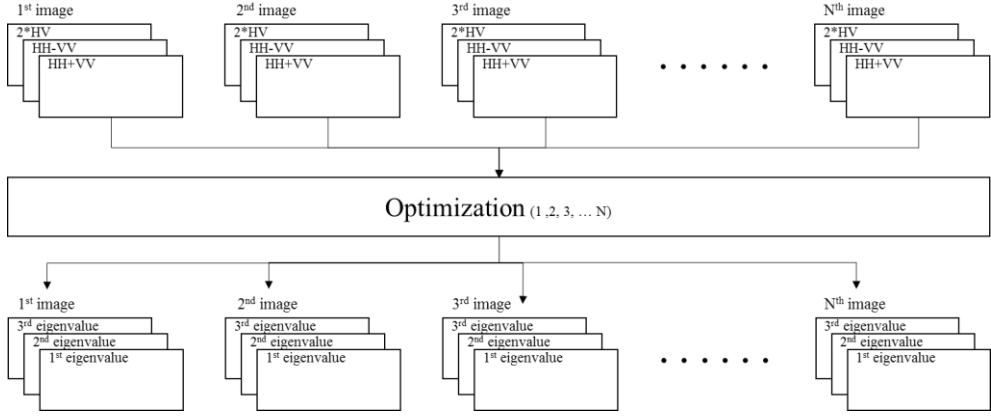


Fig. 4. 12. Interferometric coherence optimization scheme using multi-baseline multi-scattering mechanism.

$$\frac{L}{\omega_i^*} = \sum_{j=1 \neq i}^N \Omega_{ij} \omega_j + \lambda_i T_{ii} \omega_i = 0 \quad (4.21)$$

$$\begin{bmatrix} 0 & \Omega_{12} & \cdots & \Omega_{1N} \\ \Omega_{21} & 0 & \cdots & \Omega_{2N} \\ \vdots & \vdots & \ddots & \vdots \\ \Omega_{N1} & \Omega_{N2} & \cdots & 0 \end{bmatrix} \begin{bmatrix} \omega_1 \\ \omega_2 \\ \vdots \\ \omega_N \end{bmatrix} = \lambda \begin{bmatrix} T_{11} & \Omega_{12} & \cdots & 0 \\ \Omega_{21} & T_{22} & \cdots & 0 \\ \vdots & \vdots & \ddots & \vdots \\ 0 & 0 & \cdots & T_{NN} \end{bmatrix} \begin{bmatrix} \omega_1 \\ \omega_2 \\ \vdots \\ \omega_N \end{bmatrix} \quad (4.22)$$

The partial derivative of the Lagrangian problem yields the generalized eigenvalue problems. By solving the generalized eigenvalue problem, the largest eigenvalue can be obtained and it equals to the optimized coherence. If the data consist of N multi-temporal or multi-baseline images, this approach yields one eigenvector of one reference image with respect to the remaining images. In optimization process, the eigenvector is calculated to the overall coherence of remaining images, which means effectively averaged coherence of remaining images, not individual images. Thus, the coherence based on extracted vector is closest to the weighted optimized coherence rather than largest coherence.

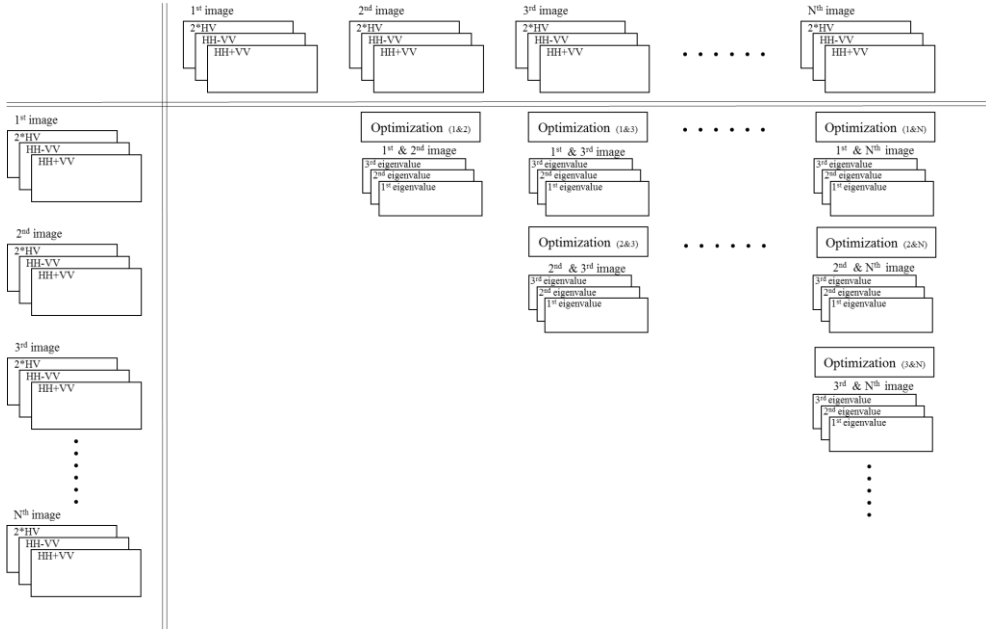


Fig. 4. 13. Interferometric coherence optimization scheme using single-baseline equal-scattering mechanism.

Equal-scattering mechanism

In contrast with MSM, the scattering mechanism could be preserved, thus, T_{ii} is similar between data sets. This is a reliable assumption when data have a small temporal baseline and spatial baseline. If the different scattering mechanisms is not necessary, the equal scattering mechanism, which has the same vector to project the optimized plane, can be used, and it is called as “Equal-scattering-mechanism”. For optimum of coherence, the following matrix can be defined.

$$\Pi_{ij} = T_s^{-1/2} \Omega_{ij} T_s^{-1/2} \quad (4.23)$$

$$\gamma_{ij}(\omega) = \frac{\omega^* \Omega_{ij} \omega}{\sqrt{\omega^* T_s \omega}} \quad (4.24)$$

$$T_s = \frac{1}{N} \sum_{i=1}^N T_i \quad (4.25)$$

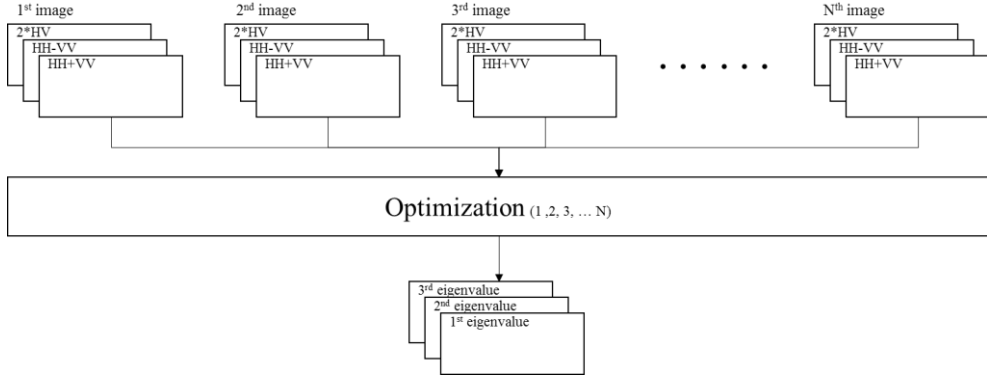


Fig. 4. 14. Interferometric coherence optimization scheme using multi-baseline equal-scattering mechanism.

The coherence corresponding the change of basis is defined as,

$$\gamma_{ij}(\omega) = \omega^* \Pi_{ij} \omega \quad (4.26)$$

By iteratively changing its basis, corresponding range of the matrix, $r(\Pi_{ij})$, changes, then the maximum of the coherence is obtained.

$$r(\Pi_{ij}) = \max\{|\omega^* \Pi_{ij} \omega| : \omega^* \omega = 1\} \quad (4.27)$$

The approach to finding the optimum using two data assuming the common ω is called as single baseline equal scattering mechanism (SB ESM). In the process, the process to find ω of the two data is repeat using each pairs as shown in Fig. 4. 10. However, for the multi-baseline case, the common ω should be defined for the all data. For this, estimate of the coherence optimum can be obtained.

$$H = \sum_{i=1}^N \sum_{j=1 \neq i}^N \Pi_{ij} \exp(-i\theta_{ij}) \quad (4.28)$$

$$Hw = \lambda w \quad (4.29)$$

The optimal vector, w , is calculated from the eigenvalue problem.

Comparison of optimized coherences

In order to optimize the interferometric coherence, the four methods could be applied, as mentioned in the previous section. Since the described methods have different physical meaning, the appropriate approach is required before the optimizations. In procedure assuming Single-baseline (or single-temporal-baseline), the optimization is repeated for the all possible pairs. Thus, the extracted vectors corresponding to the optimum vary depending on the selected pairs. The highest coherence values could be extracted via this approaches because it mathematically calculated highest coherence value. However, it is not easy to find the interpretation of the physical meaning for changing vector with respect to the other scenes. Meanwhile, the approach using multi-baseline (or multi-temporal) assumption results in the unique vector for pixels of one scene. The vectors to optimize the coherence describes the polarimetric state at the acquisition of the image. Thus, physical interpretation is reasonable even though the coherence values could be lower than single baseline case.

Also, the assumption about the scattering mechanism should be taken into account. The multi-scattering-mechanism (MSM) assume the different scattering mechanism in optimization. Thus, the vectors to define the optimum are different for the different scenes. Meanwhile, the resolution cells of different scenes share a common vector to define the optimum coherence in equal-scattering-mechanism (ESM) method. These two methods were evaluated using real data using multi-baseline approach. As shown in Fig. 4. 12, the overall coherence of MSM is higher than ESM. In outcrop area denoted as A, the coherence values are similar. In contrast, the forested area denoted as B, the coherence is much higher in MSM cases. This differences may indicate the forested area could be not optimized if ESM is applied. The possible explanation is that the common vectors used in EMS cannot represent the scattering mechanism of the vegetated area because the forested area is likely to

be affected by the temporal decorrelation.

The temporal comparison is also performed for the several test area denoted in Fig. 4. 12. The area denoted as A is mainly covered by outcrop or desert bush. The areas denoted as B, C, and D are the forested area, and area C and D were burnt due to Lake fire. The MSM shows high coherences for the outcrop area over entire time spans. Similarly, the ESM also yields high coherences, even though lower coherences are observed in some time-spans. For the coherence covariance matrices of forested area, two approaches show different coherence trends along the time span, hence, the coherence of MSM is higher than ESM. The results support that MSM approach could higher coherences than ESM similarly with the spatial analysis.

The spatial and temporal analysis imply that the dataset affected by the temporal decorrelation could be optimized using MSM approach for the higher coherence. If the temporal decorrelation is not present in the data, both approaches may yield similar coherence values.

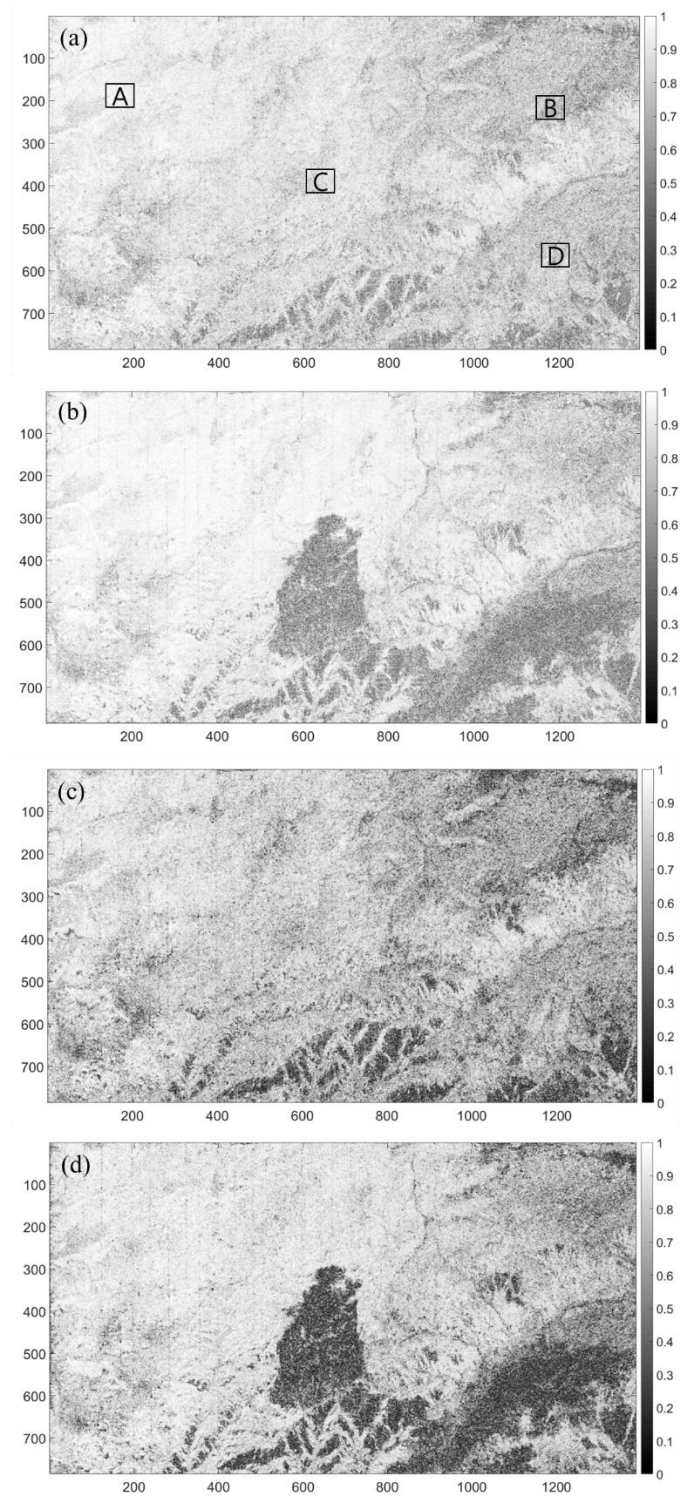


Fig. 4. 15. Optimized coherence using multi-baseline (a-b) multi-scattering-mechanism and (c-d) equal-scattering mechanism. After optimization, the coherence was obtained for interferometric pairs (a, c) January. 08.2015-May.11.2015 and (b, d) May.11.2015-June.29.2015.

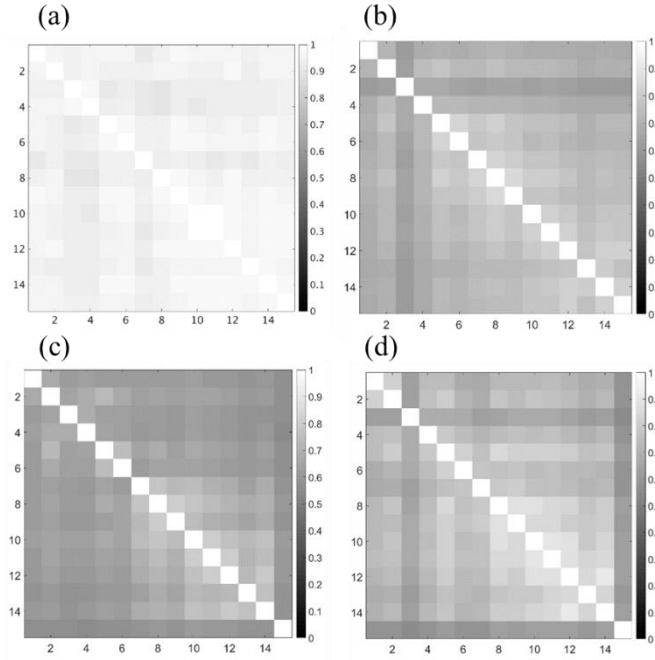


Fig. 4. 16. Coherence covariance matrices using multi-baseline multi-scattering-mechanism. (a) outcrop area, (b) unburnt forested area, (c) burnt forested area, and (d) burnt forested area which are denoted as A, B, C, and D in Fig. 4.12.

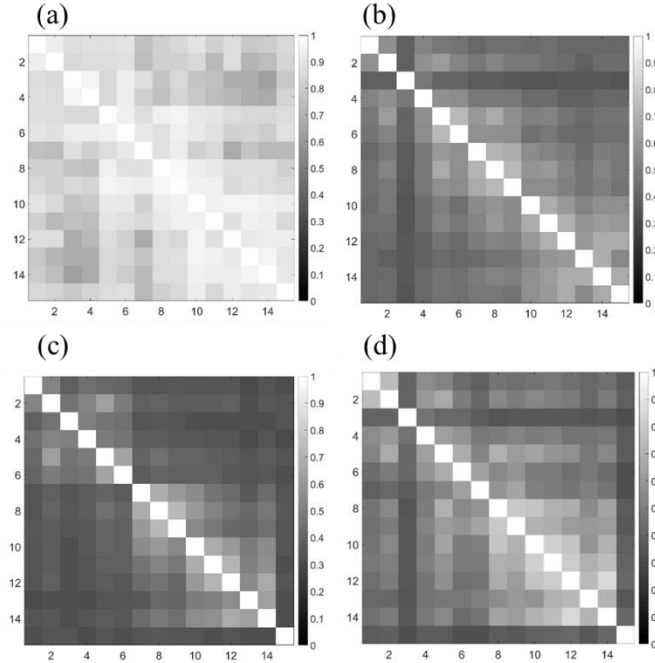


Fig. 4. 17. Coherence covariance matrices using multi-baseline equal-scattering-mechanism. (a) outcrop area, (b) unburnt forested area, (c) burnt forested area, and (d) burnt forested area which are denoted as A, B, C, and D in Fig. 4.12.

4.3.2. Temporally correlated coherence estimation

According to the model formulated in Chapter 2, the coherence model for UAVSAR data (zero-spatial baseline, multi-temporal, and quad-polarimetric SAR images) can be formulated as

$$\gamma(w) = \frac{\exp\left[-\frac{\Delta T}{\tau_v}\right] |\gamma_{t_{rand}}^v| + \mu(w) \exp\left[-\frac{\Delta T}{\tau_g}\right] |\gamma_{t_{rand}}^g| \exp\left(i\phi_{\gamma_t^g}\right)}{1 + \mu(w)} \quad (4.30)$$

In order for the inversion to be successful, the number of observations must match the number of unknowns. Throughout this chapter, let N be a number of scenes for multitemporal SAR data with a single-polarization channel, then the number of interferometric pairs is $N(N-1)/2$. In a multi-temporal polarimetric interferometric scenario, the additional polarimetric channel increases the number of new observations by a factor of $N(N-1)/2$. The formulated coherence model in Eq. (4.30), which has a zero-spatial baseline, and long temporal baseline, has 6 unknown parameters (μ , τ_g , τ_v , $\gamma_{t_{rand}}^g$, $\phi_{\gamma_t^g}$, $\gamma_{t_{rand}}^v$) for a single-polarization interferometric pair. However, the number of unknowns changes depending on 1) characteristics of model parameter, 2) additionally available polarizations, and 3) the number of available data.

As described in Chapter 2, the temporally-uncorrelated changes have different characteristics depending on the physical source inducing the decorrelation. If wind-induced motions are assumed, hence $\phi_{\gamma_t^g}$ is zero, then $\gamma_{t_{rand}}^g$ becomes real-valued and polarization-independent. Consequently, the numbers of γ_t^v and γ_t^g , become $N(N-1)/2$ and $N(N-1)/2$. Also, the total number of unknowns is $N(N-1)+3$, where the ground-to-volume ratio and the two characteristic time constants of the volume and ground layers are pair-independent parameters. An additional polarization introduces one unknown ground-to-volume ratio corresponding to the newly added polarization. If three-polarizations are available, the total numbers of unknowns and observables

are $N(N-1)+5$ and $3N(N-1)/2$.

However, if $\gamma_{t_rand}^g$ is polarization-dependent and complex valued (i.e. $\varphi_{\gamma_t^g} \neq 0$), not only the amplitude of complex coherence, but also the phase information needs to be accounted for. Hence, in the case of three-polarization, the $3N(N-1)/2+5$ real parameters are mapped onto the $3N(N-1)/2$ complex coherences. Thus, the number of the observations can be matched unknowns. In this section, the detailed inversion procedure and the extracted model parameter from UAVSAR data are discussed.

In order to estimate the model parameters, the optimized coherences were linked to the model parameters. The five unknown parameters, three ground-to-volume ratios (μ_{opt_1} , μ_{opt_2} , μ_{opt_3}) corresponding to the optimized coherences, and two temporally correlated coherence ($\gamma_{t_corr}^g$, $\gamma_{t_corr}^v$), which are pair-independent parameters, can be estimated first. If the temporally uncorrelated changes of the ground and volume layers are negligible, i.e., $\gamma_{t_rand}^{v, g} = 0$, the equation can be rewritten as:

$$\gamma_{ij.no_rand}^{opt_m} = \frac{\exp\left[-\frac{\Delta T_{ij}}{\tau_v}\right] + \mu(\omega^{opt_m}) \exp\left[-\frac{\Delta T_{ij}}{\tau_g}\right]}{1 + \mu(\omega^{opt_m})} \quad (4.31)$$

Eq. (4.31) indicates hypothetical envelope line to describe the coherence determined by the temporally correlated changes (Jung et al., 2016). Thus, the hypothetical envelope can be estimated in the subspace between 1 and the maxima of coherence values plotted as a function of temporal baseline. Furthermore, the curve is expressed as the sum of two exponential functions of the temporal baseline and an exponentially decayed envelope. Thus, the nonlinear unknown parameters are Thus, the nonlinear unknown parameters are estimated to satisfy $\min(\|D\|)$ and $D>0$, where $\|\dots\|$ indicates the Euclidean vector norm:

$$D = \begin{bmatrix} \gamma_{ij,no_rand}^{opt_1} \\ \gamma_{ij,no_rand}^{opt_2} \\ \gamma_{ij,no_rand}^{opt_3} \end{bmatrix} - \begin{bmatrix} \gamma^{opt_1} \\ \gamma^{opt_2} \\ \gamma^{opt_3} \end{bmatrix} \quad (4.32)$$

In the estimating procedure, note that the temporal decorrelation components of the ground and volume layers are assumed to be polarization invariant; thus, the coherence from each polarization is associated with the ground-to-volume-ratio. In addition, it is necessary to preserve the physical range of the model parameters (i.e. $0 \leq \gamma_{t_rand}^{v \& g} \leq 1$). Accordingly, the following constraints can be set for the estimation of the ground-to-volume-ratios:

$$\frac{\widetilde{\mu}_1}{1 + \widetilde{\mu}_1} \geq \frac{\widetilde{\mu}_2}{1 + \widetilde{\mu}_2} \frac{\gamma_{ij}^{opt_1}}{\gamma_{ij}^{opt_2}} \geq \frac{\widetilde{\mu}_3}{1 + \widetilde{\mu}_3} \frac{\gamma_{ij}^{opt_1}}{\gamma_{ij}^{opt_3}} \quad (4.33)$$

$$\frac{\widetilde{\mu}_1}{1 + \widetilde{\mu}_1} \geq \frac{\widetilde{\mu}_2}{1 + \widetilde{\mu}_2} \left(\frac{\gamma_{t_corr}^v - \gamma_{ij}^{opt_1}}{\gamma_{t_corr}^v - \gamma_{ij}^{opt_2}} \right) \geq \frac{\widetilde{\mu}_3}{1 + \widetilde{\mu}_3} \left(\frac{\gamma_{t_corr}^v - \gamma_{ij}^{opt_1}}{\gamma_{t_corr}^v - \gamma_{ij}^{opt_3}} \right) \quad (4.34)$$

for the case of $\gamma_{ij}^{opt_1} \geq \gamma_{ij}^{opt_2} \geq \gamma_{ij}^{opt_3}$. If the above constraints are not taken into consideration, the remaining parameters have physically unexplainable values. Therefore, the estimation of parameters under constraints is a notable point in this approach. The obtained characteristic time constants are linked to the ground or volume layers. Here, it is assumed that the ground is more stable than the volume in terms of coherence, i.e., $\tau_g > \tau_v$. This is a reasonable assumption because the temporally correlated changes represent the expected amount of coherence change and the volume is more likely to be affected than ground by wind or tree growth. Starting from the optimized coherence images obtained UAVSAR, the characteristic time constants of the ground and volume layers were estimated as shown in Fig. 4. 18 (a) and (b). In the case of the ground layer, high values were observed over bare soil area on the right side of the Fig. 4. 18 (a), which means that the coherence in this area could be high, even over a long time span. In contrast, the left side of Fig. 4. 18 shows relatively low values because the ground was covered by forest. A possible

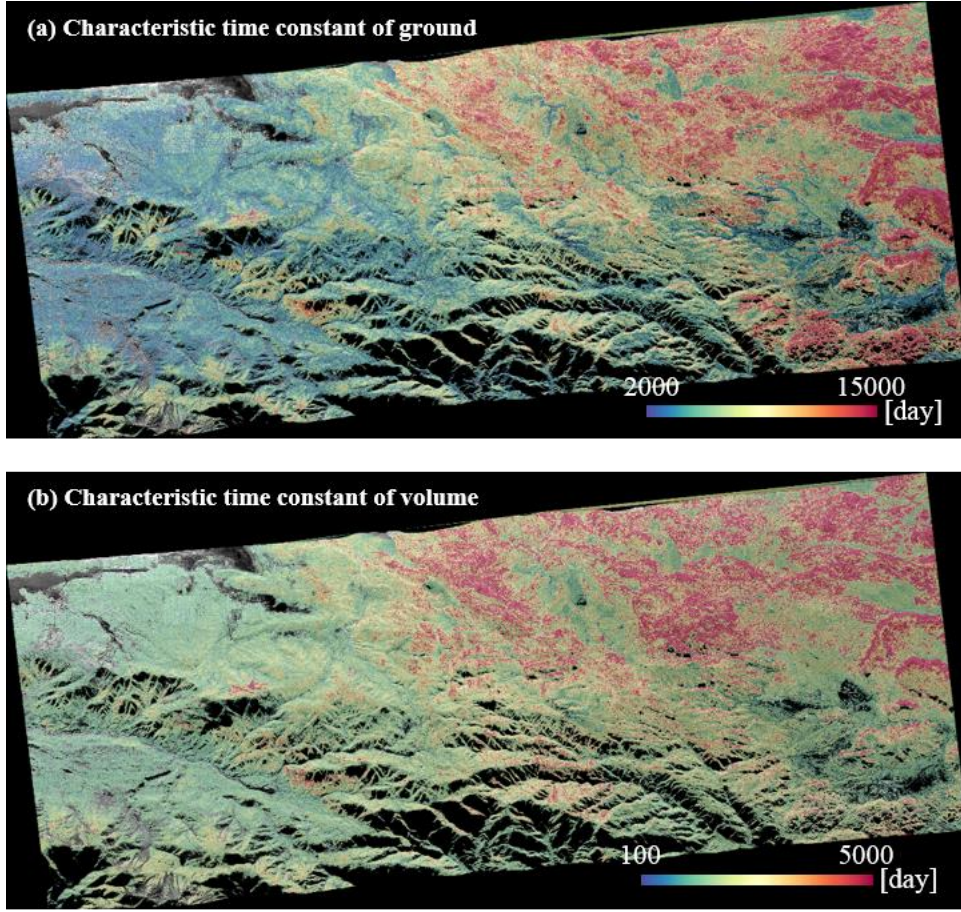


Fig. 4. 18. Characteristic time constants of (a) ground and (b) volume layers. High values of characteristic time constant mean the high coherence can be expected even in long temporal baseline.

explanation might be that the surface underlying forest is affected by fall of leaves or frequent precipitation.

4.3.3. Estimation of temporally uncorrelated coherence

Assuming no response from the ground at one optimized coherence (i.e. $\mu_{opt_3} = 0$), the numbers of pair-dependent parameters, γ_{ij,t_rand}^g and γ_{ij,t_rand}^v , are now $N(N-1)$ in complex domain and $N(N-1)/2$ in real domain, while the number of observations is $3N(N-1)/2$ in complex domain. Thus, the inversion problem has

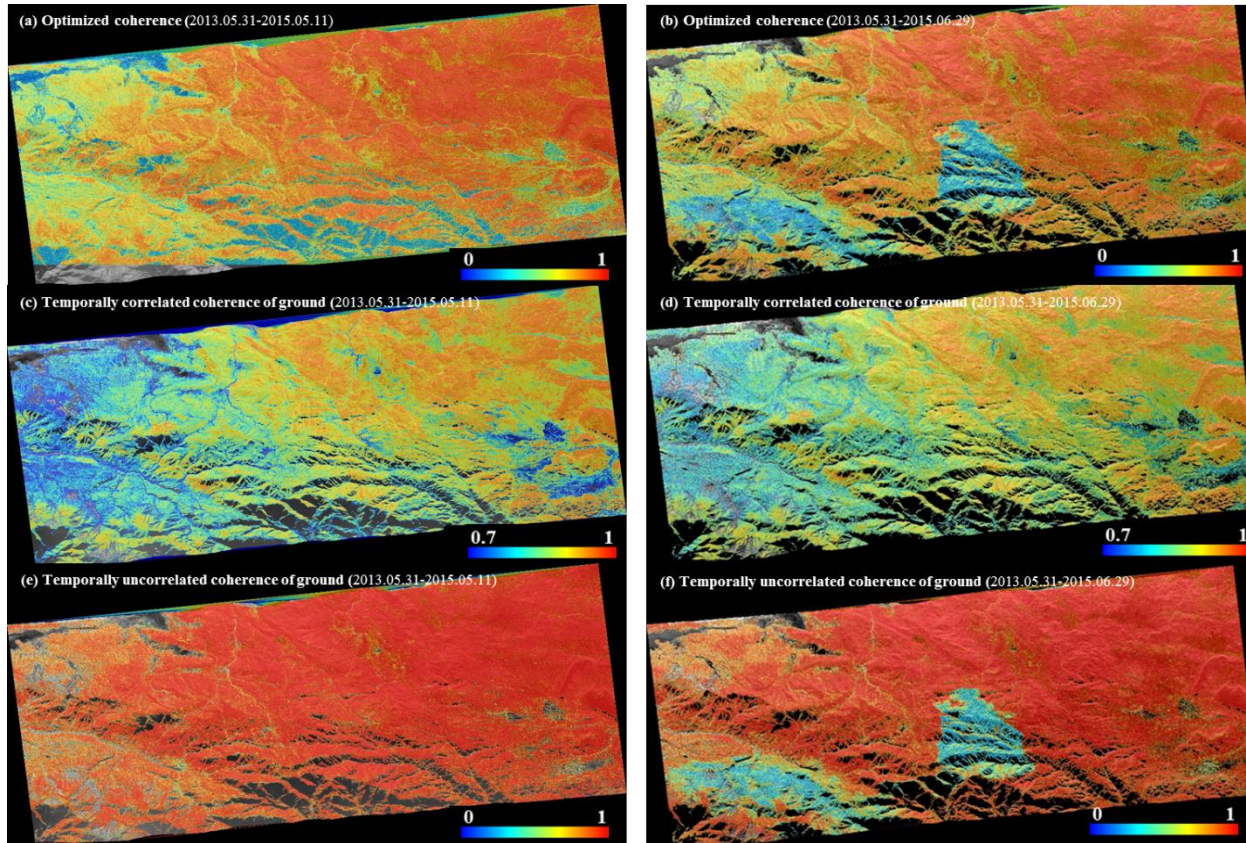


Fig. 4. 19. Model parameter extraction for the ground layer. (a) Optimized coherence before the fire. (b) Optimized coherence during the fire. The temporally correlated coherence of ground layer for (c) 710 days and (d) 759 days. The temporally uncorrelated coherence of ground layer (e) before the fire and (f) during the fire. For the pair before the fire, the scenes acquired on May 31, 2013, and May 11, 2015, are used.

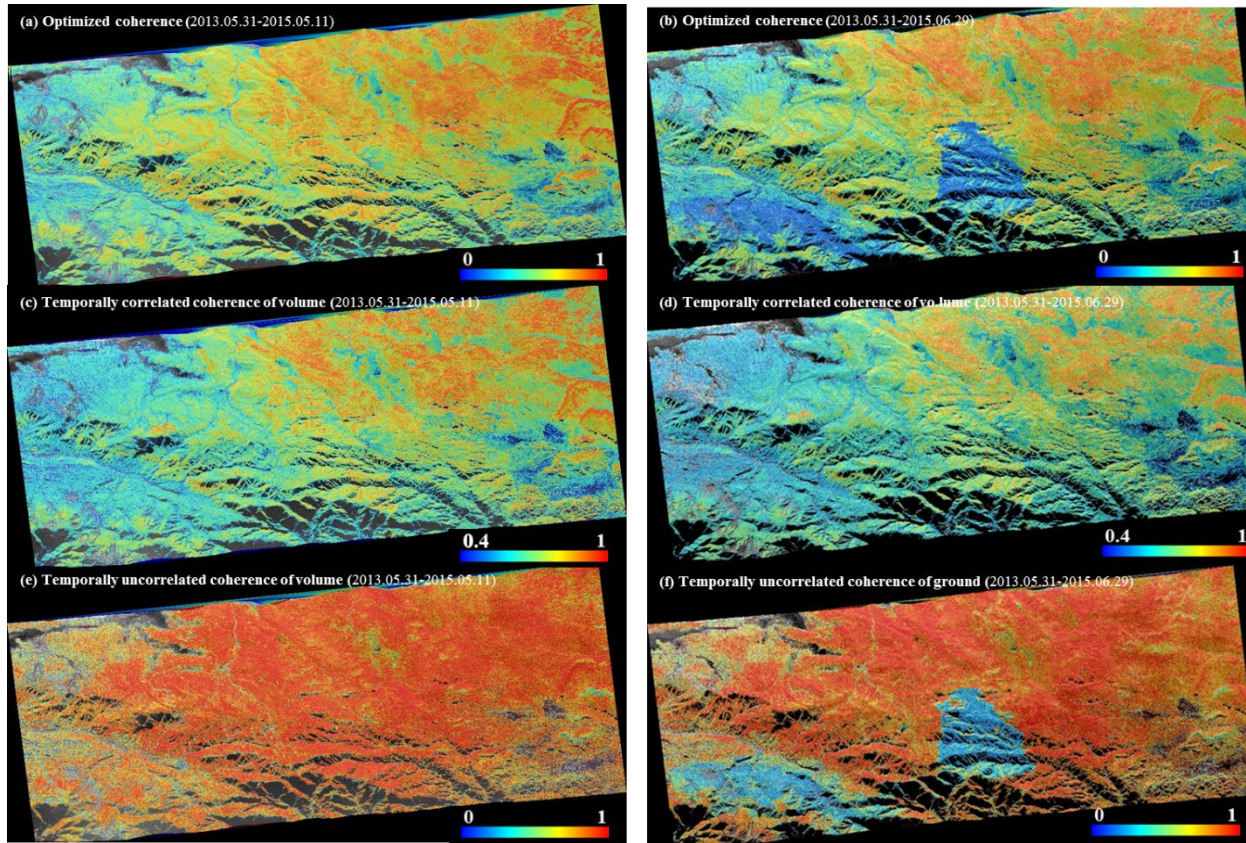


Fig. 4. 20. Model parameter extraction for volume layer. (a) Optimized coherence before the fire. (b) Optimized coherence during the fire. The temporally correlated coherence of volume layer for (c) 710 days and (d) 759 days. The temporally uncorrelated coherence of volume layer (e) before the fire and (f) during the fire. For the pair before the fire, the scenes acquired on May 31, 2013, and May 11, 2015, are used.

unique solution. Theoretically, both γ_{ij,t_rand}^g and γ_{ij,t_rand}^v can be inverted by finding the minimum as Eq. (4.35)

$$\min \left\| \begin{bmatrix} \gamma_{ij}^{opt_1} \\ \gamma_{ij}^{opt_2} \\ \gamma_{ij}^{opt_3} \end{bmatrix} - \begin{bmatrix} \gamma(\mu_{opt_1}, \tau_v, \tau_g, \gamma_{ij,t_rand}^v, \gamma_{ij,opt_1,t_rand}^g) \\ \gamma(\mu_{opt_2}, \tau_v, \tau_g, \gamma_{ij,t_rand}^v, \gamma_{ij,opt_2,t_rand}^g) \\ \gamma(\mu_{opt_1}, \tau_v, \gamma_{ij,t_rand}^v) \end{bmatrix} \right\| \quad (4.35)$$

Fig. 4. 19 and 20 show the coherences and decomposed coherences for the pair acquired on May 31, 2013, and June 29, 2015. This pair contains information of the Lake Fire, and its temporal baseline was 759 days. The fire scar caused by the Lake Fire was observed on the left to the middle of the coherence image, as shown in Fig. 5(a) and (b). However, the boundaries were unclear because of the strong temporal decorrelation of the forest area. Based on the characteristic time constants in Fig. 4. 18 and the temporal baseline of this pair (759 days), the temporally correlated coherence values were estimated as shown in Fig. 4. 19 (d) and 20 (d). These coherence images were the expected values when the pair has the temporal baseline of 759 days without any temporally uncorrelated changes. These values would be the same for all pairs with the same temporal baseline. As expected, the damage caused by the fire was observed in the temporally uncorrelated changes because such an event is categorized as the temporally uncorrelated coherence. In comparison with the optimized coherences in Fig. 4. 19 (a) and (b) and Fig. 4. 20 (a) and (b), the effect of damaged area in the temporally uncorrelated coherence was enhanced, such that it was possible to identify the periphery of the burn scar. The histograms of coherence images shown in Fig. 6 also support the effectiveness of the approach. The mean coherences of γ^{opt_1} of damaged and undamaged area are 0.34 and 0.69, respectively. The mean values of γ_{opt_1,t_rand}^g are 0.53 and 0.93 in damaged and undamaged area. Hence, the differences between the changed and unchanged areas in the temporally uncorrelated coherence is higher than in the observed coherence. Similarly, the differences of γ^{opt_3} and $\gamma_{t_rand}^v$ is 0.33 and 0.4. Therefore, applying

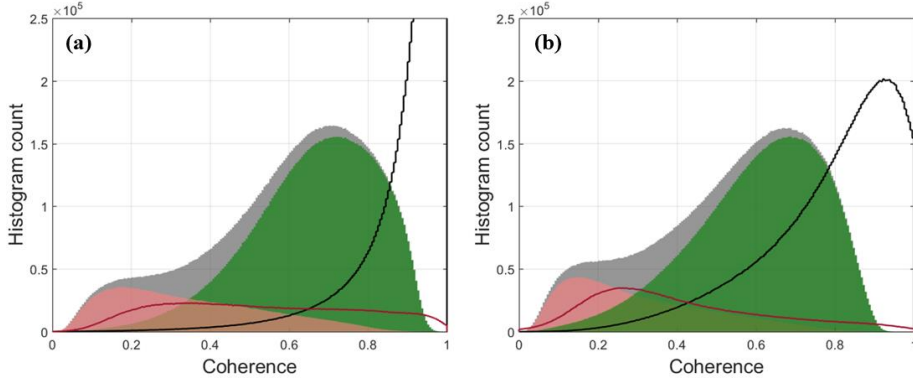


Fig. 4. 21. Histograms of total coherence (gray), the coherence of damaged area (pink), the coherence of undamaged area (green), the temporally uncorrelated coherence of damaged area (red curve), and temporally uncorrelated coherence of undamaged area (black curve) for (a) the ground and (b) the volume layer.

the coherence model is beneficial not only to the interpretation of the physical status of the scatterers but also to the damage mapping by widening the distance between undamaged and damaged values.

4.3.4. Damage probability calculation

One of the critical limitations in CCD is that the coherence images contain not only the decorrelation caused by the natural disaster but also the decorrelation due to natural changes of scatterers. In particular, delineating the perimeter of a damage of a forested area often appears on top of natural changes. In this section, this study aim to distinguish the natural disaster event from natural changes.

According to the model used in this study, the decorrelation caused by a disaster event is considered temporally uncorrelated changes because it occurs randomly in time. The temporally uncorrelated decorrelation before the event contains the effect of randomly occurring natural phenomena such as rain, snow, and wind. The effect of the event on the coherence is contained in the coherence generated from pairs acquired before and after the event. Thus, the probability of the event was estimated by comparing the temporally uncorrelated coherence of reference with those of the event. To do this, the probability density function, $p(t)$, was constructed using the

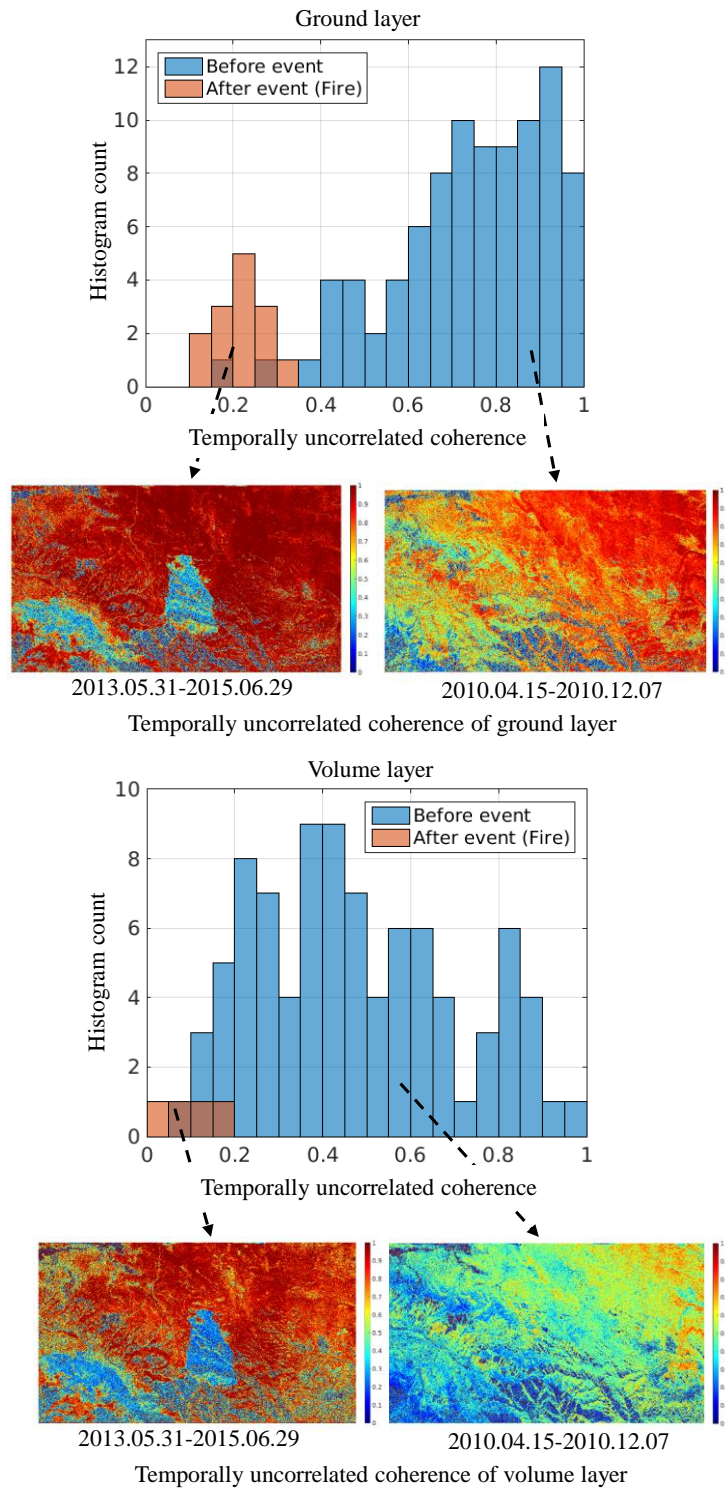


Fig. 4. 22. Damage probability calculation. The histograms can be built using history of the temporally uncorrelated coherence of ground (upper) and volume (lower) layer, respectively.

temporally uncorrelated changes of the volume and ground layers from pairs before the event (reference set), which represents statistical character of natural changes. Then, the probability of the event can be calculated from the pairs before and after event by comparing the built probability density functions:

$$\Pr(\gamma_{mn.t_{rand}}^{g\&v}) = 1 - \int_0^{\gamma_{mn.t_{rand}}^{g, v}} p_{g\&v}(t) dt \quad (4.36)$$

where \Pr indicates the probability. The indices of the scene, m , and n indicate the scene acquired before the event and after the event, respectively. Because the probability is calculated based on the probability density function of natural changes, the decorrelation caused by an event should be stronger than that induced by natural changes. Thus, this damage mapping algorithm is effective when the scatterers have suffered moderate temporal decorrelations caused by the natural changes. If the scatterers are prone to the decorrelation or the effect of the natural change is too strong, the decorrelation induced by the event cannot be distinguished.

From Eq. (4. 36), the multiple probability maps were generated corresponding to the event pairs in Fig. 7(a) and (b). In practical, the number of event pairs is 14. Some event pairs might have strong decorrelation caused by natural change, such as heavy rain, in a region where the event has not occurred, because coherence is defined as the relative difference of scatterer status. Averaging the stack of the probability maps is one way to mitigate this effect, because every event pair has the decorrelation of the event, while only a few event pairs have the decorrelation of strong natural changes. The final products of the averaged probability maps of the ground and volume layers are shown in Fig. 4. 23, respectively. It is worth note that the damaged area can be estimated in volume and ground layer separately.

To evaluate the damage mapping performance, the ancillary boundary line information provided from California Department of Forestry and Fire Protection (CAL FIRE) was rasterized in accordance with the resolution of the probability maps

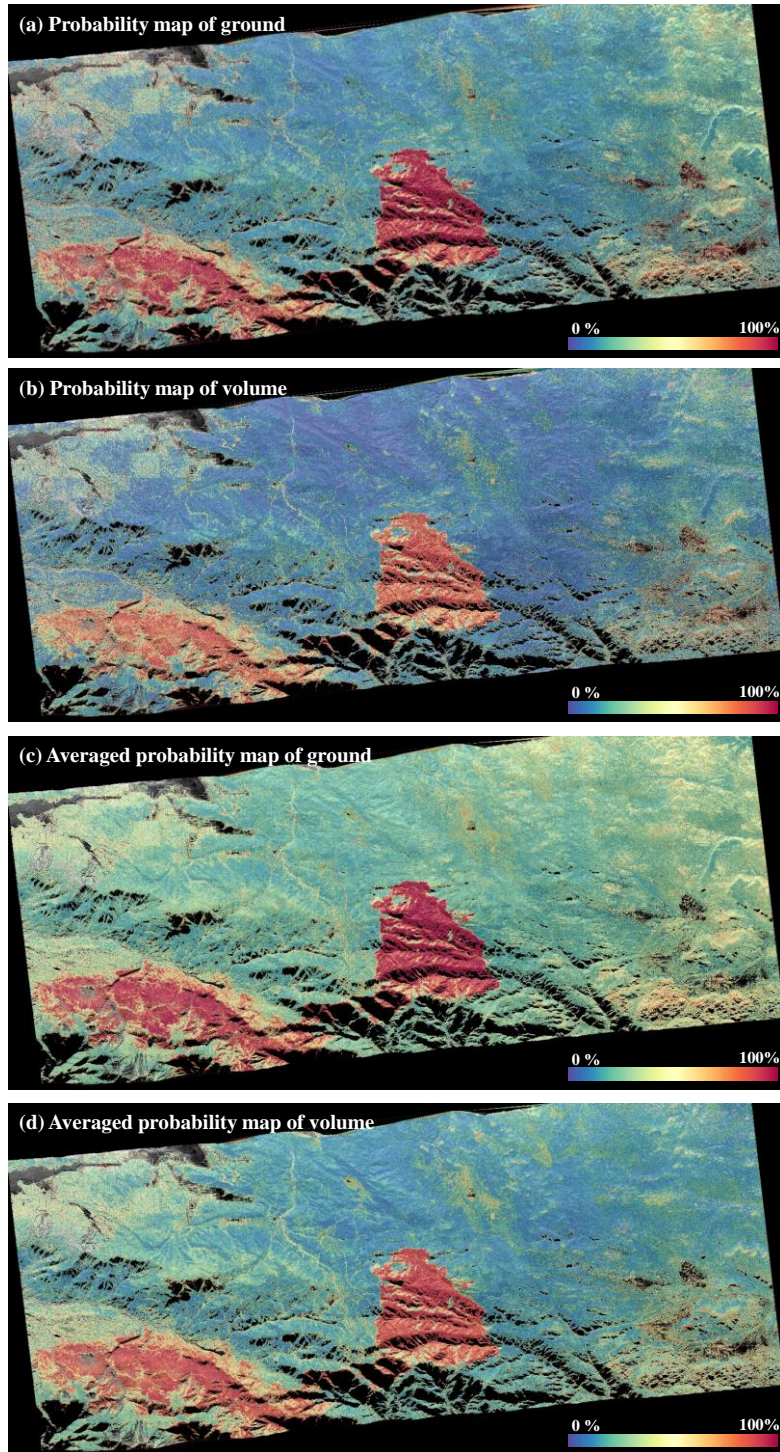


Fig. 4. 23. The calculated damage probability for (a) ground layer and (b) volume layer. The multiple probability maps of ground and volume layer can be averaged to reduce the effect of natural phenomena.

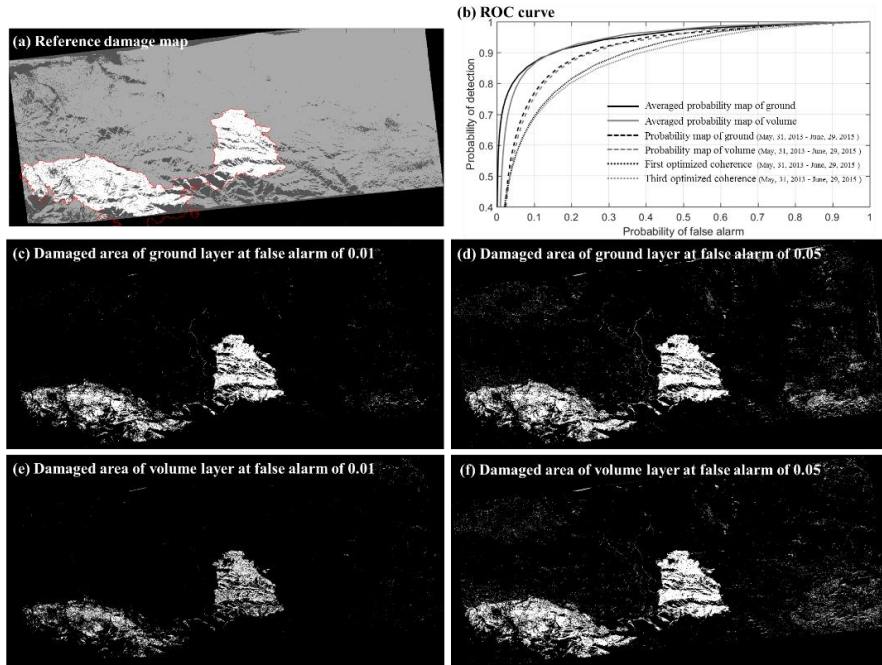


Fig. 4. 24. Performance evaluation of damage mapping algorithm. (a) reference damage map and (b) ROC curve. (c and d) The binary image of the ground layer when the false alarms are 0.01 and 0.05, respectively. (e and f) The binary image of volume layer when false alarms are 0.01 and 0.05.

and coherences. Since the boundary line of the damaged area exceeded the boundary of the SAR imaging swath, only the overlapped areas were compared. In addition, the low coherence areas due to shadow, water, and flat surfaces were also masked out. Thus, the white area was only used for comparison (Fig. 4. 24 (a)). A receiver operating characteristic (ROC) curve has been widely used for evaluating performance in change detection research. The ROC curve results show that the best performance can be obtained when the averaged probability maps (Fig. 4. 23. (c) and (d)) are used. Their probabilities of detections (PD) are 0.81 and 0.80 when the probability of false alarms (PF) is 0.05. Meanwhile, PDs are 0.58 and 0.57 when PF is 0.05 in the case of the first and third optimized coherences (Fig. 4. 19 (b) and Fig. 4.20 (b)), respectively. The PDs using the probability map of the ground and volume layers (Fig. 4.23 (a) and (b)) are 0.64 and 0.65. These prove the proposed approach effective in damage mapping.

4.4. Applicable conditions of damage mapping algorithm using coherence model

4.4.1. Coherence condition

So far, the damage mapping algorithm using coherence model has been introduced. The main concept of this algorithm is that the history of the coherence behavior which is not affected by the natural disaster can emphasize the effect of the natural disaster. To do this, the reliable coherences before the event need to be available in order to generalize the coherence behavior for each pixel. Generally, the immoderate changes including the soil moisture change and vertical profiles change can induce not only the phase disturbance but also the amplitude of the scattering change. If the pixels have been suffering excessive dielectric change, the coherence is almost zero and the incoherent approach is more proper rather than coherent approach. Thus, it is necessary to find the certain conditions which enable this algorithm applicable.

In non-zero spatial baseline case, the phase of volumetric coherence has a dependency on the ground-to-volume ratio, canopy height, and extinction coefficient because the integral term in RVoG model results in the complex values. Accordingly, the interferometric phase varies on the arbitrary polarization when the spatial baseline is nonzero. In contrast, the coherence model exploiting the temporal decorrelation without the volume decorrelation is explained under the assumption that the temporal decorrelations of ground and volume layers are complex and real values, respectively. If the significant amount of the temporal decorrelation in volume layer, which is related to the vertical profiles changes, the temporal decorrelation in volume layer can be complex. Then the accurate extraction of the model parameter may fail. Thus, the temporal decorrelation of volume layer needs to be ensured whether it is complex or not. Unfortunately, the verification of

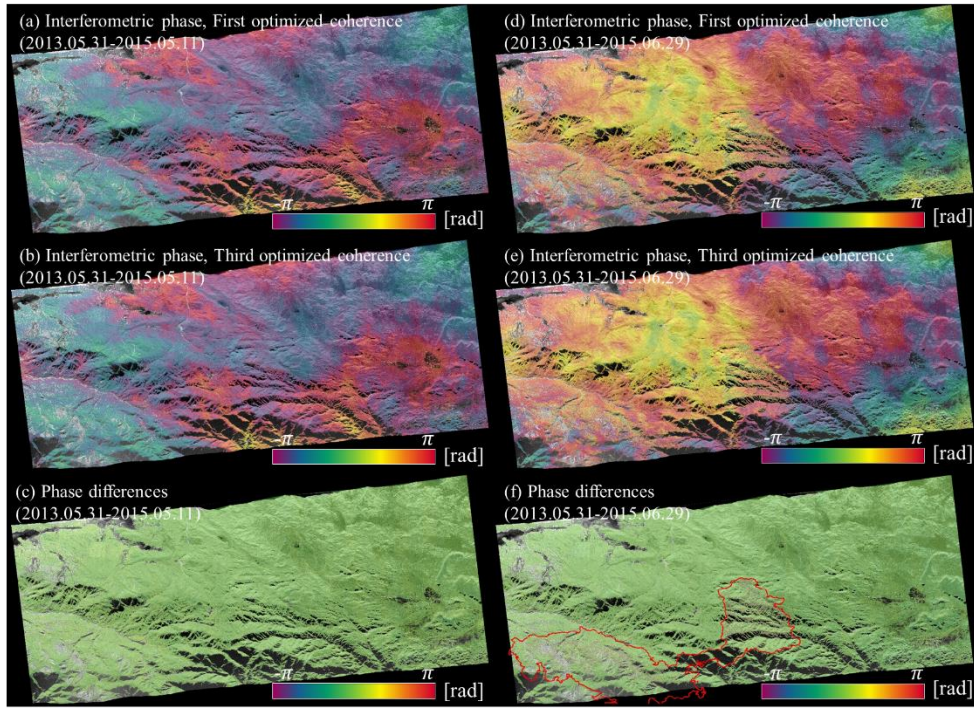


Fig. 4. 25. (a and b) The interferometric phase of optimized coherence before the fire. (c) The phase difference between two optimized coherence (i.e. (a) and (b)). (d and e) The interferometric phase of optimized coherence during the fire. (f) The phase difference between two optimized coherence (i.e. (d) and (e)).

the properties of temporal decorrelation is difficult because the parameter cannot be retrieved without the prior knowledge. Instead, the significant amount of the dielectric change can be identified by searching phase differences of each polarizations, indirectly.

The UAVSAR dataset used in this study are acquired with the zero-spatial baseline and for repeat pass scenarios. Hence, the phase associated with the topographic elevation and canopy height is ignorable. The interferometric phase can be interpreted as the contributions of the displacement of surface and atmospheric phase delay. Fig .4. 25 show the interferometric phase generated from the optimized complex coherences. Since the surface displacement and atmospheric phase delay are independent to the polarization, the interferometric phases induced by both effects are coincident at arbitrary polarizations. The differences between

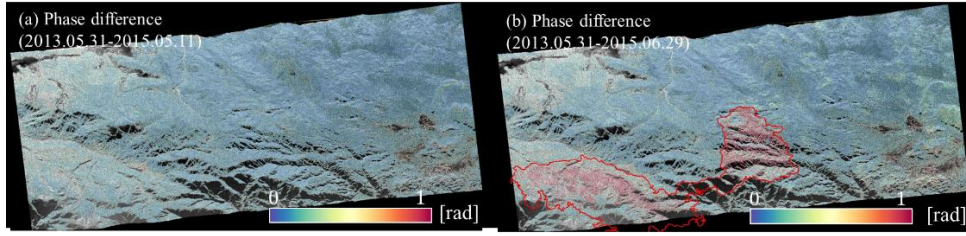


Fig. 4. 26. The absolute value of phase difference in Fig. 4. 25. (a) Before fire. (b) During fire.

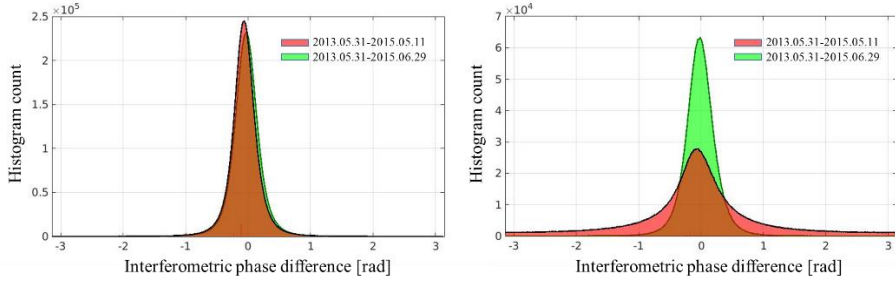


Fig. 4. 27. Histograms of phase differences in (a) unburnt area and (b) burnt area.

interferometric phases can be considered as the phase induced by the temporal decorrelation. Fig. 4. 25 (c) shows the phase differences between the first and third optimized coherences from the pair of May.31.2013 and May. 11. 2015. Almost pixels shows near zero value of phase, which indicates the phase difference between two optimized complex coherence is not severe. In terms of the physical interpretation, this implies that the temporal decorrelation event inducing the complex coherence value is not severe. However, the pair which is acquired before and after the event shows the non-zero value where the wildfire occurred. In order to emphasize this effect, and compare the non-event pair, the absolute values of phase difference are illustrated in Fig. 4. 26. In particular, the non-zero values are clearly observed over the damaged area. Hence, the certain event such as wildfire disturb the vertical structures of the target media, and accordingly, this event induced the complex value. Histograms of the phase differences over the unburnt area also verify that phase differences maintain their distribution regardless of conditions

(temporal baseline and natural condition at acquisition time). As a result, the coherence model can be applied to the pairs before the event, and the extraction of the model parameters is possible. Also, the damage mapping method can be successful by comparing the historical coherence behavior with the phenomena induced by the event.

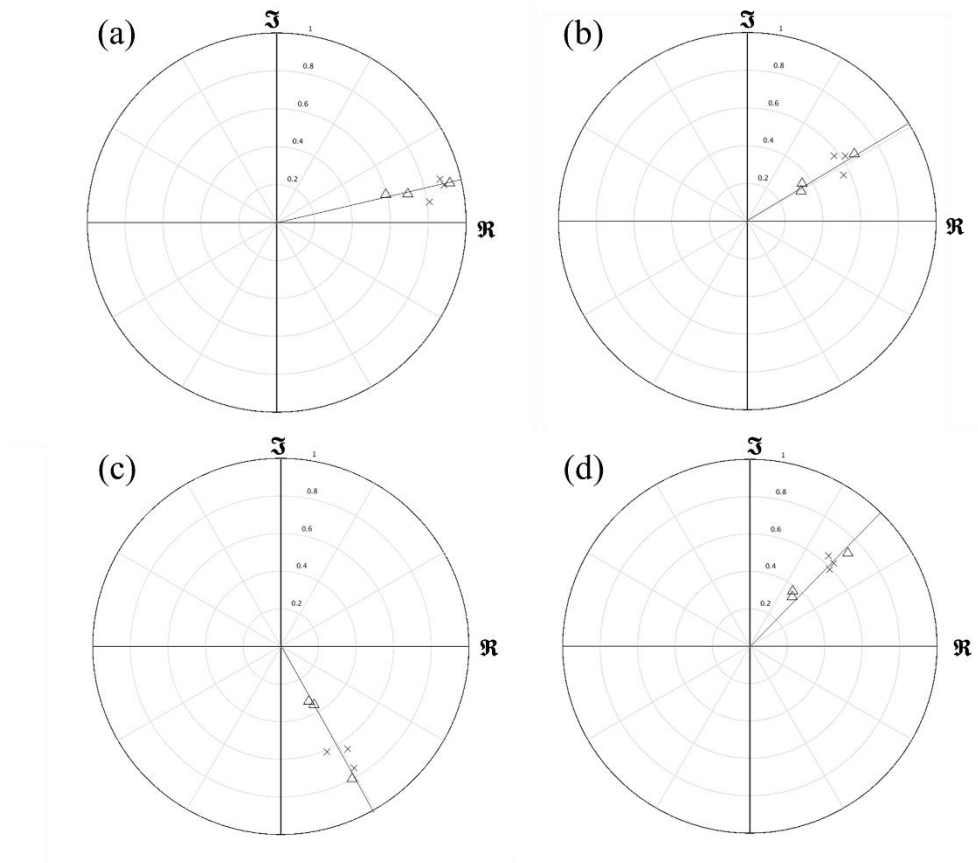


Fig. 4. 28. Complex correlation plotted in the complex plane. (a) outcrop area, (b) unburnt forested area, (c) burnt forested area, and (d) burnt forested areas which are denoted as A, B, C, and D in Fig. 4.12.

4.4.2. Number of available scenes and interferometric pairs

The key to reliable estimation of the model parameter and successful delineation of damage area is the number of the available data. In order to build the historical change belonging to the natural phenomena, the enough data to characterize the coherence behavior is required. The UAVSAR data used in this study consists of 14 scenes before the disaster event, and one scene after the event. To find out the minimum number of the scenes and the interferometric pairs can be achieved by the changing the scene list for processing, and evaluating their performances.

Tests were carried out for the step to calculate the probability by building the histograms involving the natural changes. Starting from 2 scenes, the number of the scene which will be used for histogram were increased to 14 scenes. The performance is evaluated at each time using ROC curve analysis. As shown in Fig. 4. 29, the true detection, which is accuracy of the damage detection, increase as the number of scenes increases. The increasing trend of the accuracy is observed up to 7 scenes. After 7 scenes are available, the accuracy does not increase dramatically. This indicates that if 7 scenes are available, the reliable information about the influence of the natural phenomena on the coherence can be obtained. In order to confirm this finding, the analysis was carried out for the interferometric pairs. The maxima of the interferometric pairs which can be generated from the 14 scenes is 91 pairs. The performance was recalculated by repeatedly increasing the interferometric pairs. Up to 25 pairs, the accuracy is gradually improved. Over the 25 pairs, the accuracy improvement is not seen. This result coincides to the analysis for the available scenes. If 7 scenes are available, the maxima number of the pairs is 21 pairs. The damage mapping algorithm assumes that the every interferometric pairs have only information of the temporal decorrelation. If the spatial baseline is non-zeros as in the space-borne SAR system, the interferometric pairs with the long spatial baseline should be excluded. Then, the more than 7 scenes may be required.

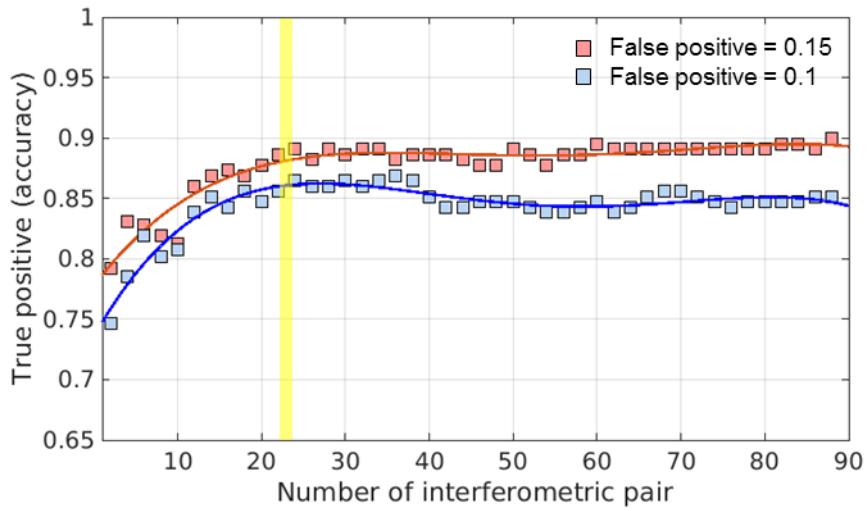
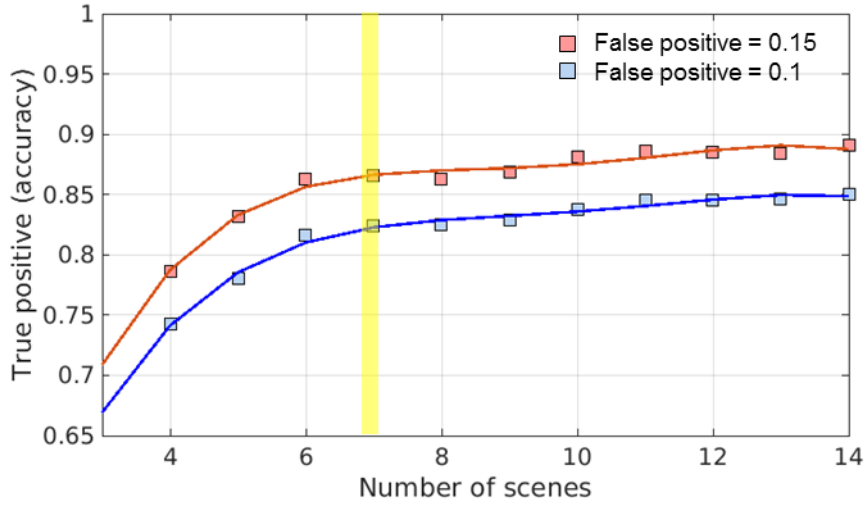


Fig. 4. 29. Performance evaluation for different number of available scenes and interferometric pairs. Red line and squares indicate the true positive changes at 0.15 false positive. Blue line and squares represent the true positive change at 0.1 false positive.

4. 5. Comparison of model inversion results and damage mapping algorithm results

In Chapter 2, the recently developed temporal decorrelation models assuming two layers were presented such as RMoG and RVoG+VTD models. In order to discriminate the temporally decreasing coherence, the model is extended and reformulated to have the terms describing the exponential function. Also, the temporal decorrelation sources are different from the RMoG and RVoG+VTD models by setting the complex coherence change related to the soil moisture change. Accordingly, the model parameter inversion adopted a different approach. Thus, it is worth quantitatively comparing the result derived from the RMoG model and the model formulated in this study.

In addition, the damage mapping algorithm using single-polarized SAR data was addressed in Chapter 3. In contrast, Chapter 4 is focusing on the damage mapping approach using full-polarized SAR. Both methods were separately evaluated and demonstrated successfully their performance. This subsection will present the quantitative comparison in terms of the model parameter inversion and damage mapping performance.

4.5.1. Comparison with RMoG model

The RMoG model is designed to extract the physical parameter of forest from polarimetric interferometric data. Hence, the RMoG model is applicable even in the case of the non-spatial baseline. The form of the model can be described as:

$$\gamma_{\text{RMoG}} = e^{i\phi_0} \frac{\gamma_{vt}^v e^{-i\phi_0} + \mu \gamma_{tg}}{\mu + 1} \quad (4.37)$$

where

$$\gamma_{vt}^v = e^{i\phi_0} \gamma_{tg} \frac{p_1 [e^{(p_2+p_3)h_v} - 1]}{(p_2 + p_3)(e^{p_1 h_v} - 1)} \quad (4.38)$$

$$\gamma_{tg} = \exp\left[-\frac{1}{2}\left(\frac{4\pi}{\lambda}\right)^2 \sigma_g^2\right] \quad (4.39)$$

$$p_1 = \frac{2\sigma_e}{\cos \theta} \quad (4.40)$$

$$p_2 = p_1 + ik_z \quad (4.41)$$

$$p_3 = -\frac{(\sigma_v^2 - \sigma_g^2)}{2h_r} \left(\frac{4\pi}{\lambda}\right)^2 \quad (4.42)$$

Here, σ_g and σ_v is the motion standard deviations of the scatterer of ground and at an arbitrary height h_r . Under the zero-spatial baseline case ($k_z = 0$), the RMoG model can be written as

$$\gamma_{\text{RMoG}_{\text{zero}}} = \frac{\gamma_{vt0}^v + \mu \gamma_{tg}}{\mu + 1} \quad (4.43)$$

$$\gamma_{vt0}^v = \gamma_{tg} \frac{p_1 [e^{(p_1+p_3)h_v} - 1]}{(p_1 + p_3)(e^{p_1 h_v} - 1)} \quad (4.44)$$

The basic forms of the RMoG and the model used in this study is similar because both models assume the coincident the structure of the forest, i.e. two layers model. However, the model in this study splits the temporal decorrelation functions of ground and volume layers into the temporally-uncorrelated and temporally-correlated coherence functions. In addition, the main physical sources to induce the temporal decorrelation is motion only in RMoG model. Hence, comparison of the amount of decorrelation is more reasonable rather than the extracted physical parameters. Also, the temporal decorrelation function γ_{vt0}^v of RMoG model is coincident to the $\exp\left[-\frac{\Delta T}{\tau_v}\right] |\gamma_{t_rand}^v|$ of the model in this study. Hence, the total amount of the temporal decorrelation need to be compared.

Fig. 4. 29 shows the correlation between the RMoG model and the model formulated in this study. These results demonstrate that the temporal coherence of volume and ground, γ_{vt0}^v and γ_{tg}^g , extracted from RMoG model has similar amount of the temporal coherence estimated from the model in this study. The high

correlations are observed not only in the short temporal baseline (49 days), but also in long temporal baseline (759 days). The temporally-correlated coherence in long temporal baseline is smaller than that in short temporal baseline. Thus, the contribution is larger in long temporal baseline in terms of temporal decorrelation. The fact that the correlation between the two models is similar implies that the extraction performance is also similar regardless of the temporal baseline. Also, the inversion approach adopted in RMoG model finds the minimum between model value and observables. Meanwhile, the inversion in this study first estimate ground-to-volume ratio and the temporally-correlated coherence by finding the closest exponential envelope to the observables. The high correlation value also demonstrates the inversion method reliable.

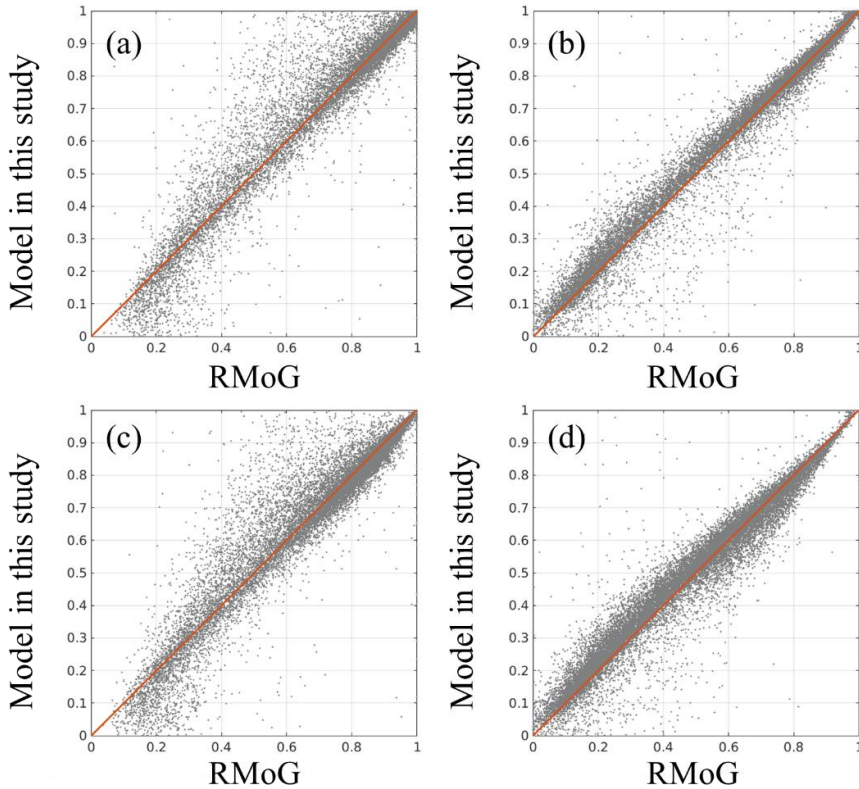


Fig. 4. 30. Temporal coherence comparisons between RMoG model and the coherence model used in this study. Temporal coherence of (a) ground and (b) volume layers for a pair 2015/05/11-2015/06/29 (49 days). Temporal coherence of (c) ground and (d) volume layers for a pair 2013/5/31-2015/06/29 (759 days)

4.5.2. Comparison with damage mapping algorithm using single-polarization data

The advantages in the use of the full-polarization are that the extraction of the model parameters is possible without the assumptions used in the approach using single-polarization, and consequently, the analysis of each layer (i.e. ground and volume layers) is independently possible. In Chapter 3 and 4, the both damage mapping algorithms using single- and full- polarizations have been introduced and validated with in-situ data. However, the comparison between both algorithms has not been fully performed. Here, in order to quantitatively assess the both algorithm in terms of extraction of the model parameters and performance of the damage mapping, the results is compared.

For this purpose, the algorithm proposed in Chapter 3 was independently applied to the dataset with the each polarization (HH, HV, and VV). The calculated characteristic time constants of ground and volume layers, τ_g and τ_v , are shown in Fig. 4. 30, 31, and 32. The high values are observed on the right side of the images, where the bare soil and low and sparse vegetation dominantly exist. In contrast, the lower value of τ_g and τ_v is mainly observed on the left side where high and relatively dense trees exist. This spatial features of τ_g and τ_v values are coherently found in the analysis using full-polarization (Fig. 4. 18). However, the obtained values from single-polarization dataset tend to be underestimated through the comparison in Fig. 4. 33. These tendencies are found in the characteristic time constants of both ground and volume layers. Indeed, the underestimated value of τ_g is easily expected from the interpretation of coherence characteristics. The HH, VV, and HV simultaneously have the contributions of the ground and volume layers. It was possible to maximize the coherence and isolate the ground effect from the volume effect by the coherence optimization procedure. Thus, the optimized coherences can have the more ground contributions than coherence generated from

HH, VV and HV polarizations. In the same perspective, the higher value of τ_v is expected in the single-polarization dataset. However, the obtained result is opposite to the expectation, because the range of the ground-to-volume ratio is set based on the criteria of temporally-uncorrelated coherence (Eq. (4.33) and (4.44)).

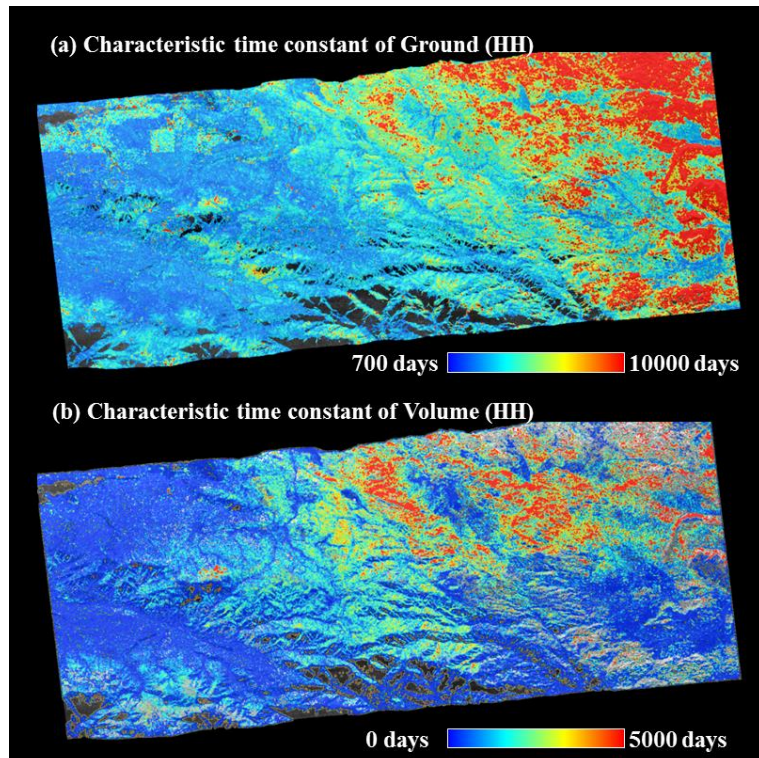


Fig. 4. 31. Characteristic time constant of (a) ground layer and (b) volume layer calculated from HH polarization data.

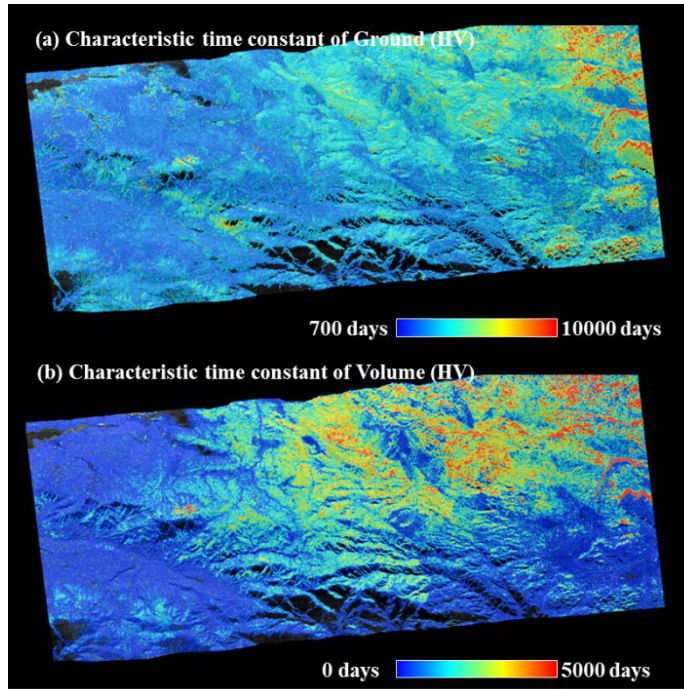


Fig. 4. 32. Characteristic time constant of (a) ground layer and (b) volume layer calculated from HV polarization data

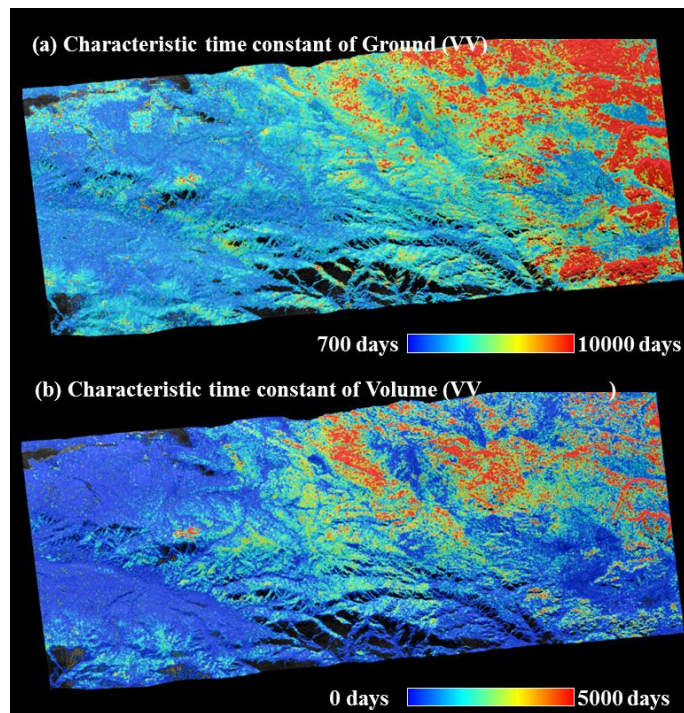


Fig. 4. 33. Characteristic time constant of (a) ground layer and (b) volume layer calculated from HH polarization data.

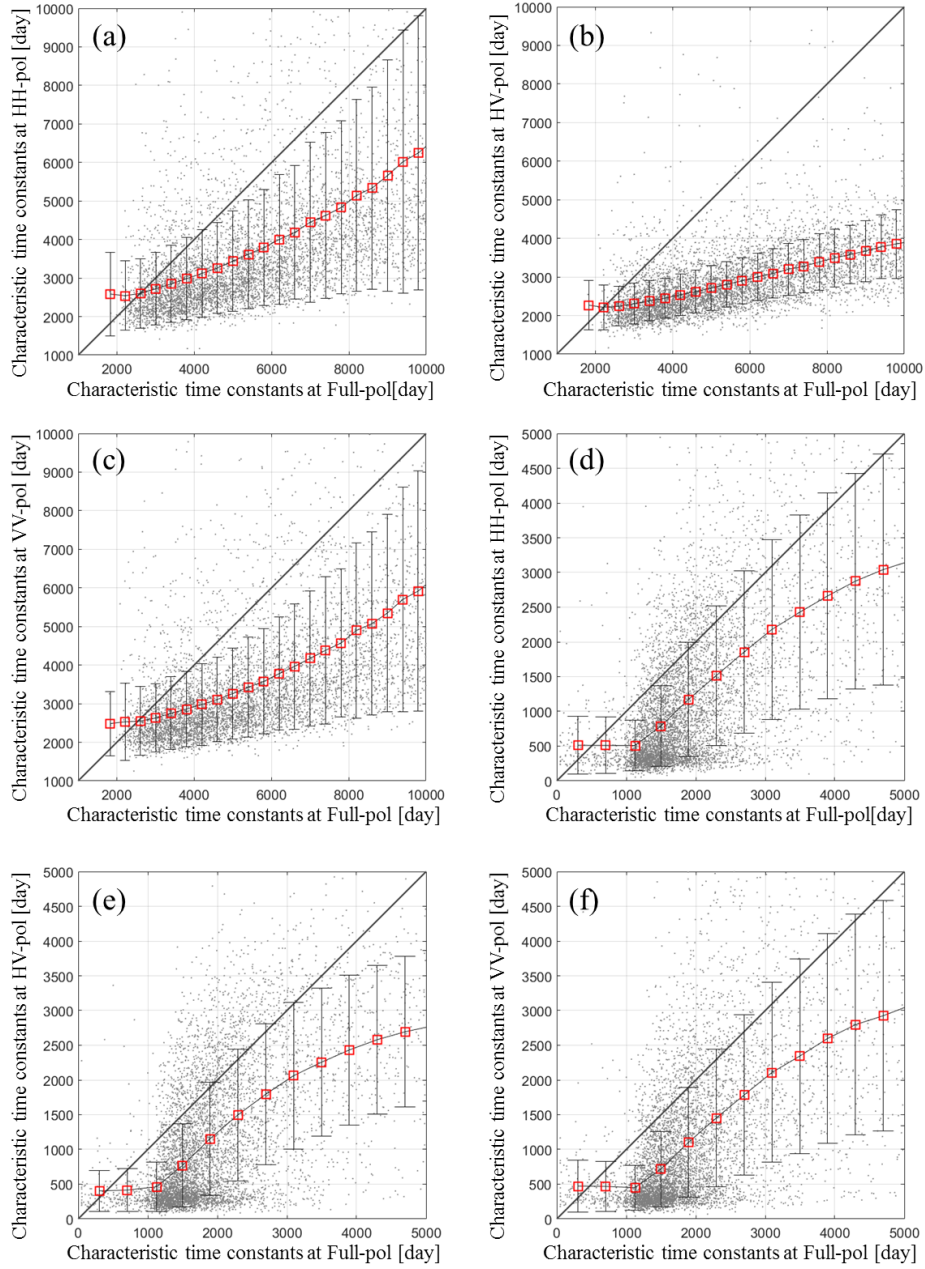


Fig. 4. 34. Comparisons of characteristic time constant of ground layer extracted from full-polarization data with (a) HH, (b) HV and (c) VV polarizations. Comparisons of characteristic time constant of volume layer extracted from full-polarization data with (d) HH, (e) HV and (f) VV polarizations.

In terms of the performance of damage mapping, the ROC curve is plotted coherently with the analysis of Full-polarization dataset. Through the ROC curve analysis, the most effective method was the damage map of the ground layer using full polarization. Interestingly, the performance of damage mapping using single-polarization is slightly lower than the approach using full-polarization, especially in HV and VV polarization, despite the underestimated parameters. The damage map of volume layer using full-polarization only prevails the effectiveness in the range from 0.03 to 0.2 of false alarm rate. This founding somehow reveals that the proposed method using single-polarization can be effective even though the model parameters are less accurate. However, it does not imply that the introduction of the polarization does not help to obtain the damage mapping. One of the main benefits in use of the polarization is that separate analysis of volume and ground layer is possible. This may be most effective when the only one layer is affected by the natural disaster such as the surface fire. In the case of the single-polarization, the damaged area can be generated but which layer is affected is not clear.

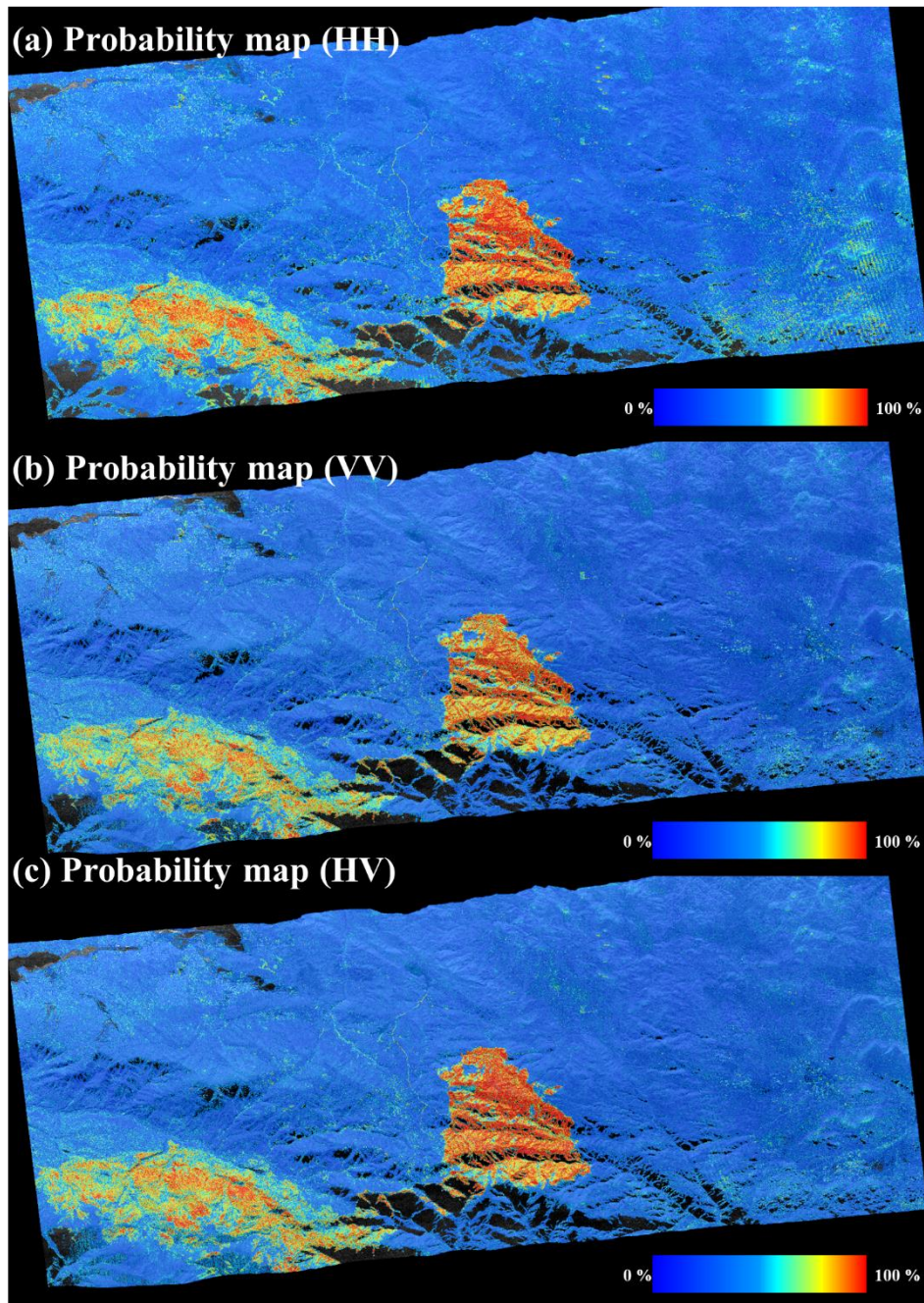


Fig. 4. 35. Damage probability maps derived from the damage mapping algorithm using multi-temporal single polarization data (Chapter 3).

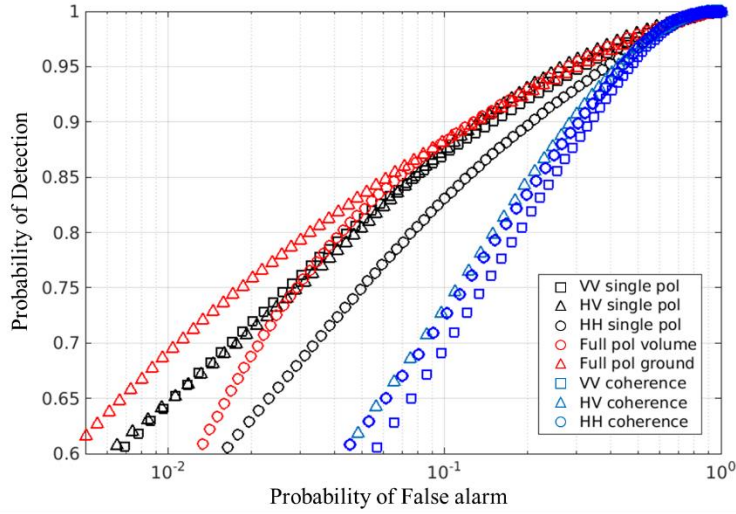


Fig. 4. 36. ROC curves for coherence and damage mapping algorithm using single-polarizations and full-polarization

Table 4. 3. The probability of detection on various damage mapping methods.

	Probability of False Alarm		
	0.01	0.05	0.1
HH coherence	0.433	0.629	0.727
HV coherence	0.376	0.618	0.727
VV coherence	0.398	0.583	0.691
HH single-pol analysis	0.533	0.748	0.830
HV single-pol analysis	0.641	0.803	0.876
VV single-pol analysis	0.641	0.813	0.868
Full-pol ground	0.691	0.833	0.883
Full-pol volume	0.541	0.819	0.882

4. 6. Discussion and conclusion

This study demonstrated the usefulness of polarimetric and interferometric SAR (PolInSAR) data for mapping damage caused by a wildfire. Challenges of coherence-based damage mapping are that the interpretation of coherence behavior is not easy and that the decorrelation caused by the damage occurs on top of natural changes. To overcome these limitations, this study first formulated a coherence model to interpret multi-temporal PolInSAR data with zero spatial baselines and long

temporal baselines using UAVSAR data. The coherence model incorporates temporally correlated change related to the decreasing of coherence as the time span increases and temporally uncorrelated changes induced by randomly occurring natural phenomena such as rain, snow, and the wind. The unique property of the model used in this study is that it has a term describing the exponentially decaying coherence with the temporal baseline. Also, the model was designed to interpret the decorrelation induced by dielectric property changes in ground layer and the positional changes in volume layer.

The limitations associated with the use and interpretation of PolInSAR data arise from the balance between the number of observations and unknown parameters. In this case, the full-polarizations and multi-temporal data were essential in solving the coherence model. The three-step parameter estimation approach was also introduced. Before estimation of the model parameters, the complex coherence is optimized. Then, pair-independent parameters (i.e. the ground-to-volume ratios and the characteristic time constants of the ground and volume layers) were estimated. The difference between the expected coherence from the envelope estimated from the temporally correlated coherence and the actual coherence estimated was interpreted as the temporally uncorrelated coherence. Thus, the temporally uncorrelated coherence could be estimated by finding minimize the actual coherence and the expected coherence.

To solve the problem regarding the mixed contributions from the natural changes and the event, the probability map was estimated by comparing the temporally uncorrelated coherence of the event set with the probability density function built from the reference set. The final probability maps of the ground and volume layers for the event were generated by an averaging stack of the probability maps of the event set.

Through the application to the 2015 Lake Fire, California, using UAVSAR data,

it is proved that the proposed approach can assist quantitatively interpretation of coherence and effective damage mapping. The result that the damage caused by the Lake Fire was included in the temporally uncorrelated coherence implies that the decorrelation caused by randomly occurring phenomena can be isolated. The analysis using the ROC curve verified that the method successfully reduced the false alarms.

This approach is meaningful because it is the first trial that the coherence model applied to the damage mapping using multitemporal PolInSAR data. Furthermore, the advantage that changes in the ground and volume layers can be detected separately is a unique characteristic. This method can be applied in many cases for damage mapping purposes, as long as a stack of quad-polarization SAR data were acquired with near-zero spatial baseline.

The algorithm used in this study was evaluated for the case that volumetric decorrelation is negligible due to near-zero spatial perpendicular baseline. Typically, data acquired from space-borne SAR systems not only have a temporal baseline but also a non-trivial spatial baseline. To overcome this limitation, the criteria used for setting the spatial baseline range should be carefully determined to minimize the volumetric decorrelation. The application utilizing the coherence model incorporated with the volumetric and temporal decorrelations, as described in Chapter 2, is also worthy of further study. This research could be useful for data acquired from the L-band ALOS-2 mission, the planned NISAR mission, and the proposed TanDEM-L mission.

Chapter 5.

Conclusions and Future Perspectives

In this study, the damage mapping algorithm using the temporal decorrelation have been presented for multi-temporal SAR data. During past decades, the SAR system has been dramatically developed and advanced, and its applications have extended their applicable range in technological and scientific aspects. The most useful advantage on the damage mapping purpose is that the radar can image the target even in poor weather conditions and night. This is critical when an emergent response is required to evaluate the damage and carry out the appropriate response to the natural disaster.

From the beginning of remote sensing techniques, the detection and assessment of damages caused by the natural disasters have been the main issue. A number of techniques to detect the change in more than two images have been proposed using remote sensing data for past decades. Also, they successfully demonstrate their robustness and effectiveness in many kinds of literature. They usually approach the problem by finding differences between the scenes related to the event of interest and interpreting the physical factor to induce these differences. Thus, the results produced by the change detection methods can be the collective of many events involving a natural disaster, and anthropogenic activities which can affect the remote sensing images. In this context, this work can be discriminated from the previous techniques, hence this study aims to detect only the changes caused by the event of interest.

When the work started, two challenging problems have been found. First is that the differences in the images are not only a result of natural disaster but also the effect of several phenomena which is not of the interest. The main tool of the damage mapping, coherence, is very sensitive to the natural phenomena, thus, the significant

loss of coherence has been observed even though the coherence is irrelevant to the natural disaster. In the case of the event pair, the decorrelation is observed over the area which is located far from the source of natural disaster. This undesired features can be considered as the primary source to degrade the performance. In order to overcome the limitation, one of the conceivable ways is the use of multi-temporal data to build the historical behavior of coherence induced by only natural phenomena.

The second problem is the decorrelation sources are various. In particular, the coherence of the vegetated area is theoretically determined by the complex structure, physical characteristic, and the response to the diverse phenomena in terms of the radar signal. Also, the observable coherences are complicated to apply the conventional method of change detection. This problem is also linked to the first issue because the model to explain the coherence of the multi-temporal data needs to be designed.

In order to successfully cope with the problems and detect the damaged area, the study has started from the theoretical background of coherence and design of coherence model for multi-temporal data in Chapter 2. The decorrelation sources are commonly categorized into four main factors, which are the thermal, geometrical, volume, and temporal baseline. The coherence model is designed so that it includes several decorrelation sources such as temporally correlated changes, temporally uncorrelated changes and the motions in the two layers; i.e. ground and volume layer. The temporally correlated change depicts the exponentially decreasing coherences with the increase of the temporal baseline, which is commonly observed in multi-temporal coherence. The temporally-uncorrelated change explains the differences between the observable coherence and hypothetic envelopes calculated the temporally correlated coherence. In reality, this term means the randomly occurring phenomena such as rain, snow, and natural disaster. The physical source of temporally-correlated and uncorrelated coherence. The parameterization of the

temporal change can be different depending on the assumption of the physical source. Hence, the standard deviation of scatterer motion and dielectric properties change can be the source. However, the discrimination of these two sources can be a challenging task and it might be unnecessary for the purpose of damage mapping.

The coherence model consists of two layers which have their own temporally-correlated and uncorrelated change terms. The ground-to-volume ratio plays an important role to determine the contributions of temporal decorrelations in ground and volume layer. The ground-to-volume ratio is a function of the backscattering of ground and volume layer, and the terms related to attenuation of the radar signal. Since the backscatter signal is also varied depending on the arbitrary polarization, the coherence can be different on the choice of polarization. If the interferometric data with multi-polarization is available, the coherence behavior can be differently observed even though the assumption that temporal decorrelation of ground and volume layer is irrelevant to the polarization is valid.

The differences with the previous model are also discussed in Chapter 2. The RVoG model does not employ the temporal decorrelation term because it is designed to explain the PolInSAR data with negligible temporal baseline. Meanwhile, RMoG model is formulated to extract the physical parameters of the forest such as extinction, canopy height, ground-to-volume ratio and temporal decorrelation. This model assumes the height-dependent temporal decorrelation, which is induced by the motions of scatterers. However, this model may be insufficient to apply the data with long-temporal baseline because not only the motion but also the dielectric properties change can dominantly affect the coherence. The model presented in this work considers properties that the coherence decrease as time spans are longer. Also, the distributions of coherence values acquired at multi-temporal acquisitions are reasonably interpreted as a sum of the temporally uncorrelated and temporally correlated changes on the ground-to-volume ratio.

The damage mapping algorithm using the suggested model was introduced for single-polarization multi-temporal data in Chapter 3 as a case study for the detection of volcanic ash. Shinmoedake volcano, which is one of the active volcanoes among Kirishima volcano cluster, erupted in January 2011 and emitted a massive amount of volcanic ash. For the detection of volcanic ash, L-band ALOS PALSAR interferometric data was used. This data was acquired over the Kirishima volcano spanning from 2007 to 2011. In order to emphasize the temporal decorrelation effect, it is necessary to minimize the other decorrelation sources. Since the volcano is covered by the dense forest, accordingly the contribution of the volume decorrelation can be severe. The volume decorrelation is commonly expressed as a function of the physical parameter of the forest, and the geometry of SAR sensors. In order to minimize the effect of the volume decorrelation, the controllable parameter is the spatial baseline. In approach using multi-temporal images, a number of the interferometric pair can be listed which have a different spatial baseline. According to RVoG model, the interferometric pairs within 1000m ensure the 0.94 of volumetric coherence under the realistic assumption for the physical parameter of the forest. During the extraction procedure for the model parameter, the challenging problem is an imbalance between the numbers of unknowns and observables. Here, the model parameters were extracted under the several assumptions. Also, the ground-to-volume ratio and the temporally-correlated coherence are first estimated using the curve fitting method and, then the temporally-uncorrelated coherences were retrieved. Once the model parameters were estimated, the probability of the damage, i.e. volcanic ash, was calculated based on the historical coherence behavior constructed by kernel density estimation method. By comparing the changes of model parameters between the reference pairs and event pairs, the probability of changes caused by volcanic ash is defined. The in-situ data, which measures the depth and area density of volcanic ash, is compared with the calculated probability

maps for determining the threshold and evaluating the performance. The correlation is found over the area where the depth of the volcanic ash is more than 5 cm and the area density is more than 10kg/m^2 . The uniqueness is that this approach show good performance, and the result has physical meanings. Introducing the new parameter can interpret the coherent behavior and enhance the measurement regardless of the time spans.

In Chapter 4, the damage mapping method for the multi-temporal and fully-polarimetric interferometric SAR data was addressed. The approach proposed in Chapter 3 has the several limitations, which the assumptions for extracting the model parameters are required. In this chapter, the assumptions used in the method can be reduced and the changes of two layer can be estimated separately by introducing polarimetric and interferometric SAR data. The approach is applied to detect the burnt area caused by the Lake Fire, in June 2015 using UAVSAR data.

In order to quantitatively evaluate the damage caused by Lake Fire, the amplitude ratio, and coherence analysis were carried out. Even though, coherence analysis shows the loss of coherence due to the fire event, the temporal decorrelation caused by the natural changes is mixed with the signal of the event. Thus, the clear discrimination of the effect of fire from the natural phenomena cannot be achieved. Also, the amplitude ratio result shows poor sensitivity, and it cannot be used for damage mapping.

The damage mapping algorithm proposed in Chapter 4 also uses the coherence model proposed in Chapter 2. Here, the temporal decorrelation of ground layer is assumed as a complex number, because it involves the soil-moisture changes, which is a polarization-dependent parameter. Hence, the fact that the use of multi-polarization causes the different level of the temporal decorrelation of ground on the arbitrary polarizations needs to be taken into account. Meanwhile, the temporal decorrelation of volume layer is assumed to be dominantly governed by the motions

of scatterers. The model parameter inversion is a key step in the application using full-polarization data. The procedure consists of the three steps, which are coherence optimization, the estimation of temporally-correlated coherence and temporally-uncorrelated coherence estimation. The extraction results show the high characteristic time constants in ground-dominant pixels, meanwhile, the relatively low value is observed in the vegetated area. It is also worth to note that the isolating procedure from observed coherence into the temporally-correlated and uncorrelated coherence enhanced the damaging effect. The proposed inversion approach is practically beneficial to independently provide the damage information of volume and ground layers.

The damage probabilities of volume and ground layers are determined based on the histograms of the natural phenomena and natural disaster. Concerning the performance of the proposed algorithm, ROC curve analysis was carried out. The quantitative analysis demonstrates the proposed method is more effective than only use of the coherence. In particular, the most robust way was when the averaged probability of ground layer was used.

However, the method is not always applicable due to the assumptions used in inversion procedure. The considerable change in the dielectric characteristic of target media can induce a significant alteration in complex coherence. In this circumstance, the coherence is observed near zero value. Then, observed coherence has no valuable meaning to be interpreted. Similarly, the significant change in the vertical structure of target media invalidate the assumptions and misinterpret the model parameters. Thus, whether the pixels experience the significant change or not needs to be checked. If the significant changes in complex coherence and the phase alteration is induced by the natural phenomena, the temporal decorrelation is a complex number. In this perspective, the phenomena can induce the different level of the phase alteration in complex coherences of arbitrary polarization. It means that the phase

angles in optimized coherences can be different. Thus, in this work, the phase differences between optimized coherence are calculated. In the unburnt area, the distributions of phase differences are stationary regardless of temporal baseline. This observation implies that strength of the temporal decorrelation is very similar in most of the cases. Therefore, the method can be applicable and results have an invaluable meaning. If this condition is not fully satisfied, the different approach such as incoherence change detection should alternatively be designed.

In Chapter 4 the reliability of the extracted model parameters was also discussed. RMoG model and its inversion process have been demonstrated in the literature. This work quantitatively compares the extracted model parameters of two algorithms. The temporal decorrelation terms in RMoG model correspond to the total amount of the temporally-correlated and uncorrelated coherence. The comparison shows the considerable correlation, and consequently the processing chain, and its products have convincingness.

The comparison between the approach using single-polarization and full polarization data is also carried out. The robustness of the damage mapping algorithm for single-polarization is demonstrated using in-situ data. Unfortunately, the extracted model parameters are not fully exploited because its verification is a troublesome task, however, the available multi-polarization allows the comparison of model parameters. The result leads that the model parameters for single-polarization approach tend to be underestimated. The returned signal is effectively determined by the many scatterers in target media. In full-polarization, the effects of distinguishable contributions of ground and volume layers can be discriminated by the coherence optimization. However, the data with single-polarization cannot adopt this key procedure, thus some inconsistency is found. Although the underestimated parameters appear, surprisingly the performance of single-polarization is discovered to be good enough to be comparable with the full-polarization technique. As

mentioned in Chapter 2, the algorithm focuses on how to assess the accurate the damage map rather than the accurate model parameter. The comparison result apparently proves that the processing chain, especially the isolating the exponentially decreasing coherence and statistical approach to determine the probability, is robust and applicable to these studies.

So far, the damage mapping algorithms based on the coherence model for single- and multi-polarization have been proposed. These have a special meaning because they are first trials for multi-temporal coherence employing the coherence model. Also, they have a benefit to provide the remarkably accurate damaged maps. The algorithms used in this work start from the stacks of a number of the SAR images. Currently, a number of SAR images are available from the beginning of space-borne and airborne mission, and the plans of a new mission for the high-resolution, high-quality, multi-polarization and short revisit time are increasing. Consequently, the requirement can be expected to be easily fulfilled. For next generation missions such as TanDEM-L, and NISAR, this algorithm has an enough potential to be applied.

국문 요약문

자연 재해에 대한 빠른 대응과 복구를 위해서는 피해 지역에 대한 평가가 선행되어야 하며, 그런 의미로 피해 지역을 탐지하는 것은 매우 중요하다. SAR 시스템은 기상적 조건과 주야에 무관하게 영상을 획득할 수 있으므로, 변화 혹은 피해 지역을 탐지할 수 있는 효율적인 방법이라고 알려져 있다. 또한 SAR 시스템을 통하여 계산할 수 있는 간밀도 (coherence)는 지표의 산란체의 움직임 혹은 유전적 성질에 변화에 매우 민감하게 반응하기 때문에 피해를 탐지하기에 적합하다고 평가되어 왔다. 그러나 간밀도를 이용한 자연재해의 피해 탐지에는 어려움이 존재할 수 있다. 즉, 탐지하고자 하는 자연재해로 인한 피해와 비, 눈, 바람과 같은 기상현상, 혹은 식생의 자연적인 변화가 미치는 영향이 간밀도에서는 유사하게 발생할 수 있기 때문이다. 이것은 레이더 신호의 간밀도가 미세한 변화에도 민감하게 반응하는 특징으로부터 기인한다. 그러므로 자연 현상으로부터 발생하는 간밀도 감소 현상은 피해 탐지 알고리즘에서 오탐지율을 증가시키는 원인이 되며, 자연 재해의 영향과 분리해야 할 필요성이 있다. 또한 다양한 지표 특성을 가지는 픽셀들은 자연 현상에 대한 각기 다른 간밀도 특성을 가지고 있기 때문에 정확한 피해 탐지를 위해서는 각 픽셀들에서의 독립적인 평가가 필요하다.

간밀도를 결정하는 요인들이 다양하고 복합적으로 작용하기 때문에 해석에 어려움이 있다는 점 역시 간밀도 기반 피해 탐지 알고리즘의 한계점이다. 특히 식생이 존재하는 지역에서의 간밀도의 변화는 더욱 복잡하게 나타날 수 있다. 그 이유는 유전적 성질을 지니고 있는 산란체들이 식생에서는 수직적으로 분포하며, 파장이 긴 레이더 신호가 이를 투과함에 따라 식생의 상층부부터 하층부 또한 지표면까지 도달되어 산란되어 간밀도를 감소시키는 체적 간밀도 감소 현상(volume decorrelation) 때문이다. 획득 시간이 동일하지 않은 두 장의 SAR 영상을 사용하는 repeat-pass 간섭기법에서는 각 식생의 각 부분에서 발생하는 변화 정보(temporal decorrelation)도 동시에 기록되기 때문에 해석은 더욱 어려워진다.

그러므로 본 연구에서는 다중 시기 긴밀도를 이용하여 자연 현상을 해석 할 수 있는 모델을 제작하고 이를 변화 탐지 알고리즘으로 확장하여, 적용 가능성을 평가하고 정밀한 피해 지역을 추출하는 것을 목적으로 한다. 이를 위하여 첫 번째로는 간섭 기법에서의 시간 차이(temporal baseline)이 길 때, 다중 시기 긴밀도(multi-temporal coherence)를 해석할 수 있는 모델을 제작하는 것을 목적으로 하였다. 두 번째로는 단일 편파의 다중 시기 SAR 영상에서 관측되는 긴밀도를 해석하고, 모델 파라미터를 추출하며, 결과적으로 피해를 탐지하기 위한 방법을 기술하고자 하였다. 세 번째로는 다중편파의 다중 시기 SAR 영상에 대한 해석 방법에 대한 연구를 진행하는 것을 목적으로 하였다.

2장에서는 긴밀도의 측정과 긴밀도를 결정하는 대표적 요인에 대하여 분석하였고 시계열 긴밀도 감소 모델을 수식화하였다. 긴밀도 요인 중 첫 번째는 열잡음 긴밀도 감소(thermal decorrelation)로서, 열 잡음(thermal noise)로부터 기인되며, 각 산란체의 신호대 잡음비(signal-to-noise ratio)와 밀접한 관련이 있다. 두 번째는 기하학적 비상관성(geometric decorrelation)으로, 두 센서가 다른 위치에서 신호를 송수신할 때 지상에 투영되는 파수의 스펙트럼이 이동함에 따라 발생한다. 세 번째 요인은 일반적으로 체적 비상관성(volume decorrelation)이라 언급되는 것으로 지상의 매질 안에 산란체가 랜덤하게 분포하고 전자파가 이를 투과할 때 발생하는 위상차이에 의하여 발생된다. 체적 비상관성은 식생에서 주로 관찰되며, 이를 설명하기 위하여 RVoG 모델이 제안되기도 하였다. RVoG 모델은 식생의 잎을 포함하는 체적 레이어와 식생 하부의 지표 레이어를 포함하는 모델로서, 두 레이어에서 결정되는 간섭기법의 위상 및 긴밀도를 설명한다. 마지막 요인은 두 영상 사이에 산란체가 변화할 때 발생하는 시간 비상관성(temporal decorrelation)이다. 픽셀 안의 산란체가 비균질하게 이동하거나, 유전체의 성질이 변화할 경우 발생한다. 일반적인 repeat-pass 간섭기법의 경우 시간 비상관성이 매우 우세하게 나타나는 경우가 많으며, 식생의 경우 체적 비상관성과 시간 비상관성이 동시에 우세하게 나타난다. 식생에서 관찰되는 체적 비상관성과 시간 비상관성을 동시에 설명하는 RMoG 모델이 제안된 바 있다.

본 연구에서는 상대적으로 긴 시간 차이를 가지고 있는 repeat-pass

간접기법에서 관측되는 긴밀도 모델을 고안하였다. 시간 비상관성을 다루는 RMoG 모델은 두 영상의 시간 차이가 크지 않을 경우, 산란체의 이동이 시간 비상관성을 발생시키는 주된 요인이라는 가정하에 제작되었다. 그러나 일반적인 인공위성 SAR는 수 일 이상의 시간 차이를 가지고 있으며, 다중 시기의 SAR 영상을 다룰 경우, 각각의 시간 차이는 상이하게 나타난다. 이 경우 시간 비상관성을 발생시키는 요인을 산란체의 이동만으로 설명하는 기에는 어려움이 있다. 그러므로 본 연구에서 고안된 모델은 지표에서의 변화를 산란체의 이동과 유전체의 성질 변화가 결합된 상태로 가정하였으며, 식생의 체적 부분은 산란체의 움직임이 체적에서의 시간 긴밀도를 감소시키는 주된 요인으로 생각하였다. 또한 다중 시기의 SAR 영상으로부터 계산된 긴밀도는 시간 차이가 증가함에 따라 긴밀도가 감소하는 현상을 관측할 수 있다. 이러한 특징은 시간 차이가 길 경우 매우 크게 나타날 수 있지만, 이전의 모델은 시간 차이가 짧은 경우를 가정하였기 때문에 그 영향이 중요하지 않았다. 그러므로 본 모델에서는 기존 모델과는 다르게 두 영상의 시간 차이가 증가함에 따라 긴밀도가 감소하는 현상을 설명하고자 지수 형태의 함수를 지표와 체적 레이어에 각각 도입하였고 이를 시간 종속적 긴밀도(temporally-correlated coherence). 즉, 체적과 지표의 두 레이어 상에서 각각의 시간에 따라서 감소하게 되며, 이는 특정한 시간 차이에서 긴밀도가 형성되었을 때 특별한 현상이 없을 경우 예측될 수 있는 값으로 생각할 수 있다. 반면, 예측되는 값과 실제 관측값과는 차이가 존재하므로 이는 시간 독립적 긴밀도(temporally uncorrelated-coherence)로 해석하였다. 체적과 지표의 시간 긴밀도 감소 현상은 전체 긴밀도에 영향을 주기 때문에 이를 지표와 체적의 비를 도입하여, 각각의 효과가 전체 긴밀도에 주는 영향에 대하여 정량화하였다.

3장에서는 제안된 모델을 기반으로 단일 편파의 다중 시기 SAR 영상에 대하여 긴밀도 변화 탐지 알고리즘의 해석이 고안되었다. 본 방법은 일본의 키리시마 화산의 2011년 화산 폭발로 발생하였던 화산재를 탐지 하는 것을 목적으로 하였으며, 본 목적을 위하여 단일 편파의 ALOS PALSAR 영상이 사용되었다. SAR 영상을 이용하여 시간 차이가 다양하게 긴밀도가 제작되었다. 사용한 multi-looking은 32 look으로 긴밀도의 바이어스가 비교적 작음을 의미한다. 또한 픽셀의 대부분에서의 열적 비상관성(thermal decorrelation)은 무시할 수 있을

정도로 나타났으며, 기하학적 비상관성(geometric decorrelation)은 common-wave spectral filtering을 사용하여 감소되었다. 또한 대상 화산은 식생이 분포하고 있기 때문에 체적 비상관성(volume decorrelation)을 최소화하여야 할 필요성이 있다. 체적 비상관성은 식생의 높이, 식생의 수직적인 구조, 두 레이더 센서의 기선거리(spatial baseline)등에 의하여 결정된다. 식생의 물리적인 파라미터는 연구에서 수정할 수 있는 변수가 아닌 반면, 다중 시기에서 만들어 진 영상은 다수의 기선거리를 가지고 있기 때문에 기선거리에 대한 조건이 설정함으로써 체적 비상관성을 최소화 할 수 있다. RVoG 모델을 기반으로 계산된 결과 ALOS PALSAR의 경우 약 1000m의 기선거리를 가지고 있을 때 체적 긴밀도는 약 0.94 이상이 됨을 알 수 있으며, 이는 체적 긴밀도를 고려하지 않아도 됨을 의미한다. 앞서 2장에서 제안된 긴밀도 모델의 파라미터의 추출을 위하여 자료는 화산 폭발 전의 간섭쌍과 화산폭발 전후의 간섭쌍의 두 그룹으로 나누어졌다. 우선 화산 폭발 이전의 긴밀도에 대한 해석 및 이해를 위하여 긴밀도 모델이 적용되었다. 모델 파라미터에서 중요한 것은 모델에 포함되어 있는 파라미터의 수와 관측 값의 수로, 관측값이 충분할 경우에만 정확한 모델 파라미터 추출이 가능하다. 그러나 단일 편파의 다중 시기 영상을 다루는 경우 미지수의 개수가 더 많기 때문에 정확한 모델 파라미터 추출은 어려울 수 있다. 그러나 본 연구에서는 모델의 특성을 이용한 가정을 바탕으로 모델 파라미터를 추출하고자 하였다. 모델 파라미터 추출의 첫 번째는 지표대 체적비 및 시간 종속적 긴밀도의 추정으로 이는 두 지수 형태의 곡선 적합(curve fitting)으로 수행되었다. 본 결과로부터 추출된 각 픽셀의 특징적 시간 상수(characteristic time constant)는 그 픽셀이 시간의 변화에 따라 긴밀도의 안정성을 보이는 상수로, 높을수록 긴 시간 차이에도 긴밀도가 높음을 의미한다. 일반적으로 인공적인 구조물이나, 식생이 없는 나지(bare soil)에서 높은 값을 보임을 알 수 있으며, 반면 식생이 있는 픽셀은 상대적으로 낮은 값을 보였다. 추정된 결과를 바탕으로 시간 독립적 긴밀도를 추정하였으나, 이 때 미지수가 관측 값의 개수보다 많으므로 파라미터 추정에 불확실성이 존재한다. 그러므로 본 연구에서는 지표와 체적에서의 시간 종속적 긴밀도의 비를 이용하여 각 픽셀 및 각 시간차이를 갖는 긴밀도에서 체적과 지표의 시간 비상관성 중 우세한 현상을 탐지하여 우세하지 않은 현상을 무시할 수 있다고 가정하였다. 즉, 만약 지표의 시간 종속적 긴밀도가 체적의 시간 종속적 긴밀도보다

그 효과가 크다면, 시간 독립적 긴밀도가 주로 지표로부터 기인된다고 가정하는 것이다. 일반적으로 식생의 긴밀도는 지표의 긴밀도와 체적의 긴밀도의 영향이 복합적으로 작용하여 결정된다. 이 때 체적의 긴밀도의 바람에 의해서도 쉽게 변하기 때문에 시간이 지남에 따라 그 영향이 거의 무시할 수 있게 된다. 그러므로 시간 차이가 짧은 경우 식생이 긴밀도에 주도적으로 영향을 줄 수 있지만, 시간 차이가 긴 경우 지표가 우세하게 긴밀도에 영향을 준다. 이와 같은 가정을 통하여 시간 독립적 긴밀도를 추출하였다. 각 픽셀에서 관찰되는 긴밀도의 현상을 통계적으로 분석하기 위하여 자연 재해가 포함되지 않은 자료의 시간 종속적 파라미터의 히스토그램을 제작하였고, 이를 기반의 자연 재해가 기존에 발생하였던 자연 현상이 가능성을 계산하였다. 반대로 이 수치는 자연 현상이 아닐 확률을 의미하기도 한다. 결론적으로 ALOS 자료를 사용하여 화산재가 쌓여있을 확률도를 계산하였다. 결과의 검증은 실제 현장 조사를 통하여 획득된 화산재의 두께와 영역 밀도 (area density)와의 비교를 통하여 진행되었다. 검증 결과는 두께로 약 5 cm 이상, 영역 밀도로 약 10 kg/m² 이상의 화산재가 쌓인 지역에서 상관성을 보임을 확인하였으며, 이를 바탕으로 성공적으로 재해에 대한 변화를 탐지하였음을 알 수 있었다.

4장에서는 긴밀도 모델을 이용하여 다중 시기의 다중 편파 SAR 영상을 활용하여 자연 재해 탐지 알고리즘에 적용되었다. 본 연구를 위하여 2009년부터 2015년까지의 15장의 UAVSAR 자료가 활용되었으며, 미국 캘리포니아 주에서 발생한 2015년의 산불 중 하나인 Lake fire에 대하여 연구가 진행되었다. 긴밀도 영상에서 산불에 의한 긴밀도 감소 현상을 확인할 수 있었지만, 식생 지역의 자연 현상에 의한 긴밀도 감소 현상과 복합적으로 발생하였기 때문에 해석에 어려움이 있었다. 영상의 진폭 영상을 이용한 자연 재해 탐지에도 산불 탐지할 만큼 민감도가 충분하지 않았다. 3장과 마찬가지로 본 연구 지역에서 긴밀도나 진폭만을 사용해서는 정확한 피해 지도를 만들기 어려웠으며, 그러므로 긴밀도 모델을 적용한 피해 탐지 알고리즘을 적용할 필요성이 있었다. 3장에서 제안된 모델 해석 방법과는 차이점이 있는데, 그것인 본 연구에서 사용되는 UAVSAR 자료가 다중 편파를 가지고 있으며, 공간 기선 거리가 거의 0에 가깝다는 특징이 있기 때문이다. 단일 편파 자료에서는 매개 변수의 값이 관측값보다 많았지만, 다중 편파의 경우 관측값이 더 많다. 그러므로 모델 파라미터 추정에

필요했던 가정을 줄일 수 있다는 장점이 있다. 또한 공간 기선거리가 거의 0에 가깝다는 것도 체적 비상관성을 무시할 수 있다는 것을 의미한다. 그러므로 관측된 긴밀도는 거의 시간 비상관성과 관련 있다고 생각할 수 있다. 모델 파라미터를 추출하기 위한 방법은 크게 3가지로 구성되었다. 첫 번째로는 지표와 체적에 대한 긴밀도 영향을 분리하기 위하여 우선적으로 긴밀도 최적화 알고리즘을 적용하였다. 본 연구에서는 다중 시기 영상마다 다른 최적화 벡터를 상정하는 MSM 알고리즘을 적용하였다. 이 과정을 통하여 관측할 수 있는 긴밀도가 최대치가 되게 만드는 편파와 그와 수직하는 편파를 찾을 수 있으며, 모델 해석과 연관시켰을 때 최대치가 되는 긴밀도는 지표의 변화에, 최소화되는 긴밀도는 체적의 변화와 관련되어 있다고 해석할 수 있다. 두 번째 단계에서는 시간 종속적 긴밀도에 해당하는 변수인 특징적 시간 상수를 추출하였으며, 지표대 체적비 역시 계산하였다. 단일 편파 추정 방법과 다르게 다중 편파 영상에서는 모든 편파의 긴밀도를 이용하여 체적과 지표에서의 시간 종속적 긴밀도를 추정한다. 세번째 단계에서는 체적과 지표에서의 시간 독립적 긴밀도를 동시에 추정하며 3장과는 다른 것은 이 과정에서 가정이 필요하지 않다는 것이다. 본 과정을 통하여 추정된 파라미터 중 시간 독립적 긴밀도는 시간 종속적 긴밀도로부터 설명되지 않는 부분을 추가적으로 설명하는 파라미터로써 갑작스럽게 일어나는 변화를 의미한다. 그러므로 이를 이용하여 각 픽셀에서 과거 동안 발생하였던 자연 현상이 긴밀도에 미치는 영향을 파악할 수 있으며, 산불은 비교적 강한 긴밀도 감소를 발생시키기 때문에 통계적인 접근을 통하여 확률적인 피해 가능성을 분석할 수 있었다. 산불의 경계 부분의 자료와의 상대적인 비교를 통한 검증 결과를 통하여 긴밀도만을 이용하여 피해 지역을 추정하는 방법보다 오탐지률을 줄일 수 있는 것을 알 수 있었다.

4장에서 사용된 모델 파라미터 추정 결과의 검증을 위하여 이전의 검증이 진행되어 왔던 RMoG 모델과 상대 비교를 진행하였다. RMoG의 체적과 지표 부분의 시간 비상관성 함수는 본 연구에서 사용된 모델의 시간 종속적 긴밀도와 시간 독립적 긴밀도의 곱으로 표현될 수 있다. 비교한 결과는 높은 상관성을 보이는 것으로 확인되었다. 또한 단일 편파와 다중 편파를 사용한 모델 파라미터 추정 결과와 재해 탐지 결과도 비교하였다. 모델 파라미터 추정의 경우, 단일 편파에서 추정된 결과가 다소 작음이 확인되었으며, 이것은 단일 편파(HH)가 지표와

체적 사이의 산란 중심에서 기록된 것으로 그 원인을 추정해볼 수 있다. 그럼에도 불구하고 피해탐지 방법에서의 정확도는 다중 편파를 사용하는 방법에 우세하게 나타났지만, 거의 유사한 정도의 정확도를 가지고 있음을 확인할 수 있었다.

본 연구에서 제안된 피해 탐지 알고리즘은 자연 현상에서 비롯되는 긴밀도 감소 현상을 분석하여 자연 재해로부터 발생하는 현상을 구별하여 피해로 규정하였다. 이를 통해, 기존의 알고리즘 보다 정확도를 향상시킬 수 있었다. 또한 다중 편파 간섭계 SAR 자료를 사용함으로써, 다중 편파에 기록되어 있는 다른 산란 중심에서의 변화를 이용하여 체적 및 지표에서의 변화를 독립적으로 평가하여 피해를 탐지하였다. 이와 같은 알고리즘은 다수의 자연 재해에 적용될 수 있으며, 각 픽셀의 긴밀도 특성을 반영하기 때문에 다양한 지표 타입에 적용될 수 있을 것으로 기대된다. 또한 물리적인 해석을 병합하여 피해의 심각도를 정량화 할 수 있는 가능성 역시 존재 하며, 향후 발사될 인공위성의 미션에서도 적용될 수 있기 때문에 본 연구의 의의가 크다고 판단할 수 있다.

Bibliography

- Amelung, F., Galloway, D. L., Bell, J. W., Zebker, H. A., & Lacznia, R. J. (1999). Sensing the ups and downs of Las Vegas: InSAR reveals structural control of land subsidence and aquifer-system deformation. *Geology*, 27(6), 483-486.
- Askne, J., & Hagberg, J. (1993). *Potential of interferometric SAR for classification of land surfaces*. Paper presented at the Geoscience and Remote Sensing Symposium, 1993. IGARSS'93. Better Understanding of Earth Environment., International.
- Askne, J. I., Dammert, P. B., Ulander, L. M., & Smith, G. (1997). C-band repeat-pass interferometric SAR observations of the forest. *IEEE Transactions on Geoscience and Remote Sensing*, 35(1), 25-35.
- Balzter, H. (2001). Forest mapping and monitoring with interferometric synthetic aperture radar (InSAR). *Progress in Physical Geography*, 25(2), 159-177.
- Bamler, R., & Just, D. (1995). Phase statistics and decorrelation in SAR interferograms. *System*, 1, E2.
- Barber, J. (2015). A Generalized Likelihood Ratio Test for Coherent Change Detection in Polarimetric SAR. *IEEE Geoscience and Remote Sensing Letters*, 12(9), 1873-1877.
- Barber, J., & Kogon, S. (2012). *Probabilistic three-pass sar coherent change detection*. Paper presented at the Signals, Systems and Computers (ASILOMAR), 2012 Conference Record of the Forty Sixth Asilomar Conference on.
- Berardino, P., Fornaro, G., Lanari, R., & Sansosti, E. (2002). A new algorithm for surface deformation monitoring based on small baseline differential SAR interferograms. *IEEE Trans. Geosci. Remote Sens.*, 40(11), 2375-2383.
- Bouaraba, A., Younsi, A., Belhadj Aissa, A., Acheroy, M., Milisavljevic, N., & Closson, D. (2012). Robust techniques for coherent change detection using COSMO-SkyMed SAR images. *Prog. Electromagn. Res.*, 22, 219-232.
- Bouaraba, A., Younsi, A., Belhadj Aissa, A., Acheroy, M., Milisavljevic, N., &

- Closson, D. (2012). Robust techniques for coherent change detection using Cosmo-SkyMed SAR images. *Progress In Electromagnetics Research M*, 22, 219-232.
- Bourgeau-Chavez, L. L., Kasischke, E. S., Riordan, K., Brunzell, S., Nolan, M., Hyer, E., . . . Ames, S. (2007). Remote monitoring of spatial and temporal surface soil moisture in fire disturbed boreal forest ecosystems with ERS SAR imagery. *International Journal of Remote Sensing*, 28(10), 2133-2162.
- Bovolo, F., & Bruzzone, L. (2005). A detail-preserving scale-driven approach to change detection in multitemporal SAR images. *IEEE Trans. Geosci. Remote Sensing*, 43(12), 2963-2972.
- Bowman, A. W., & Azzalini, A. (1997). *Applied smoothing techniques for data analysis*. New York: Oxford University Press Inc.
- Bruzzone, L., Marconcini, M., Wegmuller, U., & Wiesmann, A. (2004). An advanced system for the automatic classification of multitemporal SAR images. *IEEE Transactions on Geoscience and Remote Sensing*, 42(6), 1321-1334.
- Cloude, S., & Papathanassiou, K. (2003). Three-stage inversion process for polarimetric SAR interferometry. *IEE Proceedings-Radar, Sonar and Navigation*, 150(3), 125-134.
- Cloude, S. R. (2010). *Polarisation : applications in remote sensing*. United States: Oxford University press Inc.
- Cloude, S. R., & Papathanassiou, K. P. (1998). Polarimetric SAR interferometry. *IEEE Transactions on Geoscience and Remote Sensing*, 36(5), 1551-1565. doi:Doi 10.1109/36.718859
- Cloude, S. R., & Pottier, E. (1997). An entropy based classification scheme for land applications of polarimetric SAR. *IEEE Transactions on Geoscience and Remote Sensing*, 35(1), 68-78.
- Collins, J. B., & Woodcock, C. E. (1996). An assessment of several linear change detection techniques for mapping forest mortality using multitemporal Landsat TM data. *Remote Sensing of Environment*, 56(1), 66-77.
- Corr, D. G., & Rodrigues, A. (1998). *Coherent change detection of vehicle movements*. Paper presented at the Geoscience and Remote Sensing Symposium Proceedings, 1998. IGARSS'98. 1998 IEEE International.
- De Zan, F., Parizzi, A., Prats-Iraola, P., & López-Dekker, P. (2014). A SAR

- interferometric model for soil moisture. *IEEE Transactions on Geoscience and Remote Sensing*, 52(1), 418-425.
- Dekker, R. (1998). Speckle filtering in satellite SAR change detection imagery. *Int. J. Remote Sensing*, 19(6), 1133-1146.
- Ferretti, A., Prati, C., & Rocca, F. (2001). Permanent scatterers in SAR interferometry. *IEEE Transactions on Geoscience and Remote Sensing*, 39.(1), 8-20.
- Fielding, E. J., Talebian, M., Rosen, P. A., Nazari, H., Jackson, J. A., Ghorashi, M., & Walker, R. (2005). Surface ruptures and building damage of the 2003 Bam, Iran, earthquake mapped by satellite synthetic aperture radar interferometric correlation. *Journal of Geophysical Research: Solid Earth*, 110(B3).
- Flynn, T., Tabb, M., & Carande, R. (2002). *Coherence region shape extraction for vegetation parameter estimation in polarimetric SAR interferometry*. Paper presented at the Geoscience and Remote Sensing Symposium, 2002. IGARSS'02. 2002 IEEE International.
- Galloway, D. L., Hudnut, K. W., Ingebritsen, S. E., Phillips, S. P., Peltzer, G., Rogez, F., & Rosen, P. A. (1998). Detection of aquifer system compaction and land subsidence using interferometric synthetic aperture radar, Antelope Valley, Mojave Desert, California. *Water Resources Research*, 34(10), 2573-2585.
- Gatelli, F., Guamieri, A. M., Parizzi, F., Pasquali, P., Prati, C., & Rocca, F. (1994). The wavenumber shift in SAR interferometry. *IEEE Trans. Geosci. Remote Sens.*, 32(4), 855-865.
- Geudtner, D., Winter, R., & Vachon, P. W. (1996). Flood monitoring using ERS-1 SAR interferometry coherence maps. in *Proc. Int. Geosci. Remote Sens. Symp.*, 2, 966-968.
- Gong, M., Zhou, Z., & Ma, J. (2012). Change detection in Synthetic Aperture Radar Images based on Image Fusion and Fuzzy Clustering. *IEEE Trans. Image Processing*, 21(4), 2141-2151.
- Goodenough, D. G., Chen, H., Richardson, A., Cloude, S., Hong, W., & Li, Y. (2012). Mapping fire scars using Radarsat-2 polarimetric SAR data. *Canadian Journal of Remote Sensing*, 37(5), 500-509.
- Graham, L. C. (1974). Synthetic interferometer radar for topographic mapping. *Proceedings of the IEEE*, 62(6), 763-768.

- Grey, W. M. F., Luckman, A. J., & Holland, D. (2003). Mapping urban change in the U.K. using satellite radar interferometry. *Remote Sens. Environ.*, 87(1), 16-22.
- Hajnsek, I., Kugler, F., Lee, S.-K., & Papathanassiou, K. P. (2009). Tropical-forest-parameter estimation by means of Pol-InSAR: The INDREX-II campaign. *IEEE Transactions on Geoscience and Remote Sensing*, 47(2), 481-493.
- Hajnsek, I., & Prats, P. (2008). *Soil moisture estimation in time with D-InSAR*. Paper presented at the Geoscience and Remote Sensing Symposium, 2008. IGARSS 2008. IEEE International.
- Hensley, S., Wheeler, K., Sadowy, G., Jones, C., Shaffer, S., Zebker, H., . . . Chao, R. (2008). *The UAVSAR instrument: Description and first results*. Paper presented at the Radar Conference, 2008. RADAR'08. IEEE.
- Hoffmann, J. (2007). Mapping damage during the Bam (Iran) earthquake using interferometric coherence. *International Journal of Remote Sensing*, 28(6), 1199-1216.
- Homer, C., Dewitz, J., Fry, J., Coan, M., Hossain, N., Larson, C., & Wickham, J. (2007). Completion of the 2001 national land cover database for the conterminous United States. *Photogrammetric Engineering and Remote Sensing*, 73(4), 337.
- Hooper, A. (2008). A multi-temporal InSAR method incorporating both persistent scatterer and small baseline approaches. *Geophysical Research Letters*, 35(16).
- Jordan, R. (1997). *Shuttle Radar Topography Mission System Functional Requirements Document*. Retrieved from
- Jung, J., Kim, D.-j., Lavallo, M., & Yun, S.-H. (2016). Coherent Change Detection Using InSAR Temporal Decorrelation Model: A Case Study for Volcanic Ash Detection. *IEEE Transactions on Geoscience and Remote Sensing*, 54(10), 5765-5775.
- Jung, J., Kim, D.-j., & Park, S.-E. (2014). Correction of atmospheric phase screen in time series InSAR using WRF model for monitoring volcanic activities. *IEEE Transactions on Geoscience and Remote Sensing*, 52(5), 2678-2689.
- Krieger, G., Moreira, A., Fiedler, H., Hajnsek, I., Werner, M., Younis, M., & Zink, M. (2007). TanDEM-X: A satellite formation for high-resolution SAR

- interferometry. *IEEE Transactions on Geoscience and Remote Sensing*, 45(11), 3317-3341.
- Kugler, F., Schulze, D., Hajnsek, I., Pretzsch, H., & Papathanassiou, K. P. (2014). TanDEM-X Pol-InSAR performance for forest height estimation. *IEEE Transactions on Geoscience and Remote Sensing*, 52(10), 6404-6422.
- Lavalle, M., & Hensley, S. (2015). Extraction of structural and dynamic properties of forests from polarimetric-interferometric SAR data affected by temporal decorrelation. *IEEE Transactions on Geoscience and Remote Sensing*, 53(9), 4752-4767.
- Lavalle, M., Simard, M., & Hensley, S. (2012). A temporal decorrelation model for polarimetric radar interferometers. *IEEE Transactions on Geoscience and Remote Sensing*, 50(7), 2880-2888.
- Lee, J.-S., Grunes, M. R., & Kwok, R. (1994). Classification of multi-look polarimetric SAR imagery based on complex Wishart distribution. *International Journal of Remote Sensing*, 15(11), 2299-2311.
- Lee, S. K., Kugler, F., Papathanassiou, K. P., & Hajnsek, I. (2013). Quantification of temporal decorrelation effects at L-band for polarimetric SAR interferometry applications. *IEEE Journal of Selected Topics in Applied Earth Observations and Remote Sensing*, 6(3), 1351-1367.
- Lombardini, F., Gini, F., Farina, A., & Griffiths, H. (1998). Effect of temporal decorrelation on 3-D SAR imaging using multiple pass beamforming.
- Lombardini, F., & Griffiths, H. (Jul. 1998). *Effect of temporal decorrelation on 3D SAR imaging using multiple pass beamforming*. Paper presented at the Proc. IEEEUREL Meeting Radar Sonar Signal Process, Peebles, U.K.
- Massonnet, D., Briole, P., & Arnaud, A. (1995). Deflation of Mount Etna monitored by spaceborne radar interferometry. *Nature*, 375(6532), 567-570.
- Massonnet, D., Rossi, M., Carmona, C., Adragna, F., Peltzer, G., Feigl, K., & Rabaute, T. (1993). The displacement field of the Landers earthquake mapped by radar interferometry. *Nature*, 364(6433), 138-142.
- Miyabuchi, Y., Hanada, D., Niimi, H., & Kobayashi, T. (2013). Stratigraphy, grain-size and component characteristics of the 2011 Shinmoedake eruption deposits, Kirishima Volcano, Japan. *J. Volcanol. Geoth. Res.*, 258, 31-46.
- Moreira, A., Krieger, G., Hajnsek, I., Hounam, D., Werner, M., , R., S., &

- Settlemeyer, E. (2004). TanDEM-X: a TerraSAR-X add-on satellite for single-pass SAR interferometry. In *Geoscience and Remote Sensing Symposium, 2004. IGARSS'04. Proceedings. 2004 IEEE International*, 2, 1000-1003.
- Morrison, K., Bennett, J. C., Nolan, M., & Menon, R. (2011). Laboratory measurement of the DInSAR response to spatiotemporal variations in soil moisture. *IEEE Transactions on Geoscience and Remote Sensing*, 49(10), 3815-3823.
- Moser, G., & Serpico, B. (2006a). Generalized minimum-error thresholding for unsupervised change detection from SAR amplitude imagery. *IEEE Trans. Geosci. Remote Sensing*, 44(10), 2972-2982.
- Moser, G., & Serpico, B. (2006b). Generalized minimum-error thresholding for unsupervised change detection from SAR amplitude imagery. *IEEE Trans. Geosci. Remote Sensing*, 44(10), 2972-2982.
- Nesti, G., Tarchi, D., Bedidi, A., Despan, D., Rudant, J., Bachelier, E., & Borderies, P. (1998). Phase shift and decorrelation of radar signal related to soil moisture changes. *EUROPEAN SPACE AGENCY-PUBLICATIONS-ESA SP*, 441, 423-430.
- Neumann, M., Ferro-Famil, L., & Reigber, A. (2008). Multibaseline polarimetric SAR interferometry coherence optimization. *IEEE Geoscience and Remote Sensing Letters*, 5(1), 93-97.
- Neumann, M., Ferro-Famil, L., & Reigber, A. (2010). Estimation of forest structure, ground, and canopy layer characteristics from multibaseline polarimetric interferometric SAR data. *IEEE Trans. Geosci. Remote Sens.*, 48(3), 1086-1104.
- Neumann, M., Ferro-Famil, L., & Reigber, A. (2010). Estimation of forest structure, ground, and canopy layer characteristics from multibaseline polarimetric interferometric SAR data. *IEEE Transactions on Geoscience and Remote Sensing*, 48(3), 1086-1104.
- Newey, M., Benitz, G., & Kogon, S. (2012). *A generalized likelihood ratio test for SAR CCD*. Paper presented at the Signals, Systems and Computers (ASILOMAR), 2012 Conference Record of the Forty Sixth Asilomar Conference on.

- Nico, G., Pappalepore, M., Pasquariello, G., Refice, A., & Samarelli, S. (2000). Comparison of SAR amplitude vs. coherence flood detection methods-a GIS application. *International Journal of Remote Sensing*, 21(8), 1619-1631.
- Nico, G., Pappalepore, M., Pasquariello, G., Refice, A., & Samarelli, S. (2000). Comparison of SAR amplitude vs. coherence flood detection methods - a GIS application. *Int. J. Remote Sens.*, 21(8), 1619-1631.
- Nolan, M., & Fatland, D. R. (2003). Penetration depth as a DInSAR observable and proxy for soil moisture. *IEEE Transactions on Geoscience and Remote Sensing*, 41(3), 532-537.
- Nolan, M., Fatland, D. R., & Hinzman, L. (2003). DInSAR measurement of soil moisture. *IEEE Transactions on Geoscience and Remote Sensing*, 41(12), 2802-2813.
- Novak, L. M. (2005). *Coherent change detection for multi-polarization SAR*. Paper presented at the Signals, Systems and Computers, 2005. Conference Record of the Thirty-Ninth Asilomar Conference on.
- Oishi, N., Tsuchida, M., Wakayama, T., Hasegawa, H., & Okada, Y. (2009). *A coherence improvement technique for coherent change detection in SAR interferometry*. Paper presented at the Radar Conference, 2009. EuRAD 2009. European.
- Olesk, A., Voormansik, K., Tamm, T., Noorma, M., & Praks, J. (2015). *Seasonal effects on the estimation of height of boreal and deciduous forests from interferometric TanDEM-X coherence data*. Paper presented at the SPIE Remote Sensing.
- Papathanassiou, K. P., & Cloude, S. R. (2001). Single-baseline polarimetric SAR interferometry. *IEEE Transactions on Geoscience and Remote Sensing*, 39(11), 2352-2363.
- Papathanassiou, K. P., & Cloude, S. R. (2003). The effect of temporal decorrelation on the inversion of forest parameters from PoI-InSAR data. *In International Geoscience and Remote Sensing Symposium*, 3, III-1429.
- Park, S.-E., Yamaguchi, Y., & Kim, D.-j. (2013). Polarimetric SAR remote sensing of the 2011 Tohoku earthquake using ALOS/PALSAR. *Remote Sensing of Environment*, 132, 212-220.
- Praks, J., Antropov, O., & Hallikainen, M. T. (2012). LIDAR-aided SAR

- interferometry studies in boreal forest: Scattering phase center and extinction coefficient at X-and L-band. *IEEE Transactions on Geoscience and Remote Sensing*, 50(10), 3831-3843.
- Preiss, M., Douglas, G. A., & Stacy, N. J. S. (2006). Detecting Scene Changes Using Synthetic Aperture Radar Interferometry. *IEEE Transactions on Geoscience and Remote Sensing*, 44(8), 2041-2054.
- Preiss, M., & Stacy, N. J. (2006). *Coherent change detection: Theoretical description and experimental results*. Retrieved from
- Qong, M. (2005). Coherence optimization using the polarization state conformation in PolInSAR. *IEEE Geoscience and Remote Sensing Letters*, 2(3), 301-305.
- Rignot, E. J. M., & Zyl, J. J. v. (1993). Change detection techniques for ERS-1 SAR data. *IEEE Tans. Geosci. Remote Sensing*, 44(8), 896-906.
- Rocca, F. (2007). Modeling interferogram stacks. *IEEE Transactions on Geoscience and Remote Sensing*, 45(10), 3289-3299.
- Rosen, P. A., Hensley, S., Joughin, I. R., Li, F. K., Madsen, S. N., Rodriguez, E., & Goldstein, R. M. (2000). Synthetic aperture radar interferometry. *Proceedings of the IEEE*, 88(3), 333-382.
- Sato, M., Chen, S.-W., & Satake, M. (2012). Polarimetric SAR analysis of tsunami damage following the March 11, 2011 East Japan earthquake. *Proceedings of the IEEE*, 100(10), 2861-2875.
- Shimada, M., Isoguchi, O., Tadono, T., & Isono, K. (2009). PALSAR radiometric and geometric calibration. *IEEE Trans. Geosci. Remote Sensing*, 47(12), 3915-3932.
- Siegert, F., & Hoffmann, A. A. (2000). The 1998 forest fires in East Kalimantan (Indonesia): A quantitative evaluation using high resolution, multitemporal ERS-2 SAR images and NOAA-AVHRR hotspot data. *Remote Sensing of Environment*, 72(1), 64-77.
- Siegert, F., & Ruecker, G. (2000). Use of multitemporal ERS-2 SAR images for identification of burned scars in south-east Asian tropical rainforest. *International Journal of Remote Sensing*, 21(4), 831-837.
- Singh, A. (1989). Review article digital change detection techniques using remotely-sensed data. *International Journal of Remote Sensing*, 10(6), 989-1003.
- Sun, B., Chen, J., Li, C.-S., & Zhou, Y.-Q. (2010). FA-SCANSAR: Full aperture

- scanning pulse by pulse for the nearspace slow-moving platform borne SAR. *Progress In Electromagnetics Research B.*, 25, 23-37.
- Takahashi, M., Nasahara, K. N., Tadono, T., Watanabe, T., Dotsu, M., Sugimura, T., & Tomiyama, N. (2013). *JAXA high resolution land-use and land-cover map of Japan*. Paper presented at the in Proc. IEEE IGARSS'2013, Melbourne, VIC.
- Technology, N. I. o. A. I. S. a. (2011). Isomass contours that describes ash accumulation from Kirishimayama-Shinmoedake eruption between 26 and 27 January, 2011. Retrieved from http://www.aist.go.jp/aist_j/press_release/pr2011/pr20110201_2/pr20110201_2.html
- Touzi, R., Lopes, A., Bruniquel, J., & Vachon, P. W. (1999). Coherence estimation for SAR imagery. *IEEE Trans. Geosci. Remote Sens.*, 37(1), 135-149.
- Treuhaft, R. N., & Siqueira, P. R. (2000). Vertical structure of vegetated land surfaces from interferometric and polarimetric radar. *Radio Science*, 35(1), 141-177.
- Van Zyl, J., & Burnette, C. (1992). Bayesian classification of polarimetric SAR images using adaptive a priori probabilities. *International Journal of Remote Sensing*, 13(5), 835-840.
- Van Zyl, J. J. (2001). The Shuttle Radar Topography Mission (SRTM): a breakthrough in remote sensing of topography. *Acta Astronautica*, 48(5), 559-565.
- Wahl, D. E., Yocky, D. A., Jakowatz, C. V., & Simonson, K. M. (2016). A new maximum-likelihood change estimator for two-pass sar coherent change detection. *IEEE Transactions on Geoscience and Remote Sensing*, 54(4), 2460-2469.
- Wei, M., & Sandwell, D. T. (2010). Decorrelation of L-band and C-band interferometry over vegetated areas in California. *IEEE Transactions on Geoscience and Remote Sensing*, 48(7), 2942-2952.
- White, R. G., & Oliver, J. (1990). *Change detection in SAR imagery*, Arlington.
- Yonezawa, C., & Takeuchi, S. (2001). Decorrelation of SAR data by urban damages caused by the 1995 Hyogoken-nanbu earthquake. *International Journal of Remote Sensing*, 22(8), 1585-1600.
- Yu, B., & Phillips, R. D. (2014). *Using contextual information to improve SAR CCD*:

Bayesian contextual coherent change detection (BC CCD). Paper presented at the IGARSS.

- Yun, S.-H., Hudnut, K., Owen, S., Webb, F., Simons, M., Sacco, P., . . . Fielding, E. (2015). Rapid damage mapping for the 2015 Mw 7.8 Gorkha earthquake using synthetic aperture radar data from COSMO–SkyMed and ALOS-2 satellites. *Seismological Research Letters*, 86(6), 1549-1556.
- Zebker, H., & Villasenor, J. (1992). Decorrelation in interferometric radar echoes. *IEEE Trans. Geosci. Remote Sensing*, 30(5), 950-959.
- Zwieback, S., Hensley, S., & Hajnsek, I. (2015). Assessment of soil moisture effects on L-band radar interferometry. *Remote Sensing of Environment*, 164, 77-89.